ABSTRACT

Title of Dissertation: EXPLORING FLUXONIUM-BASED QUANTUM COMPUTING

Wei-Ju Lin
Doctor of Philosophy, 2025

Dissertation Directed by: Professor Kasra Sardashti
Department of Physics

Fluxonium qubit is a promising elementary building block for quantum information processing due to its long coherence time combined with a strong anharmonicity. In this thesis, we first introduce a novel fluxonium qubit operating at zero magnetic field with high coherence. We implement and characterize single-qubit gates with an average gate fidelity of 99.93%, extracted from randomized benchmarking. This qubit serves as a ready-to-use superconducting qubit that operates in the frequency range of conventional transmons and exhibits stronger anharmonicity.

Next, we implement a 60 ns direct CNOT gate on two inductively coupled fluxoniums, which behave almost exactly like a pair of transversely coupled spin-1/2 systems. Notably, the typically undesirable static ZZ term, arising from non-computational transitions, is nearly absent even in the presence of strong qubit-qubit hybridization. The CNOT gate fidelity, estimated via randomized benchmarking, reaches 99.94%. Furthermore, this fidelity remains above 99.9% over a span of 24 days without any recalibration between measurements. Compared with the 99.96% fidelity of a 60 ns identity gate, our results constrain non-decoherence-related errors during logical operations to as low as 2×10^{-4}. This work adds a simple and robust two-qubit gate to the still relatively small family of “beyond three nines” gates on superconducting qubits.

EXPLORING FLUXONIUM-BASED QUANTUM COMPUTING

by

Wei-Ju Lin

Dissertation submitted to the Faculty of the Graduate School of the
University of Maryland, College Park in partial fulfillment
of the requirements for the degree of
Doctor of Philosophy
2025

Advisory Committee:
  Professor Kasra Sardashti, Co-Chair
  Professor Jay D. Sau, Chair
  Professor Benjamin S. Palmer
  Professor Aaron Sternbach
  Professor Ichiro Takeuchi, Dean's Representative

Dedication

To my parents.

Acknowledgments

My pursuit of a PhD over the past four years in a foreign country was made possible by the support of many wonderful people. I am truly grateful to them, for it is because of their support that my PhD journey has become a memory I will cherish forever.

I would first like to thank my parents, Chi-Yi and Wen-Hsiang, for their unconditional love and for always putting me before themselves. I am deeply grateful for their understanding and the tremendous effort they have made to support me through all the challenges I faced in pursuit of my career goals. I would like to thank my grandmother, Lee-Hsueh, for being a source of motivation, inspiration, and strength for me and our entire family. I also express my gratitude to my grandparents, Ching-Yu, Shou-Hsien, and Kun-Yen for filling my childhood with love.

I would like to thank my advisor, Prof. Vladimir Manucharyan. Vlad always provided critical guidance and insightful advice whenever I encountered challenges in our projects. I also learned a great deal from him about how to present results effectively and convey complex concepts clearly. Thank you, Vlad, for organizing the lab and projects in a way that allowed me to explore topics of personal interest, and for ensuring I had support from people with diverse expertise to help me complete my research smoothly throughout my Ph.D. I would also like to thank my thesis advisor, Prof. Kasra Sardashti, for taking care of the lab and guiding me through the final stage of my Ph.D., especially in completing all the graduation requirements during my last year after Vlad moved to EPFL. Your support made a significant difference, and I would have faced much greater difficulty without it. I would like to extend my gratitude to my committee members, Prof. Jay D. Sau, Prof. Benjamin S. Palmer, Prof. Aaron Sternbach, and Prof. Ichiro Takeuchi, for their time, feedback, and guidance.

I would like to thank my colleagues in our group. Dr. Haonan Xiong, a senior graduate student when I joined the group, taught me much of what I know in the lab. He was thorough and guided me through a wide range of skills from fabrication and microwave engineering to qubit measurements, including gate optimization and characterization. I am sincerely grateful to Haonan for his patience and for walking me through every detail. My pursuit of a Ph.D. would not have been possible without his guidance. I appreciate Dr. Raymond Mencia for always being willing to share with me the knowledge about fluxonium. Ray also kindly taught me and shared his experience in various lab works, especially the operation and maintenance of e-gun deposition system and fabrication tips. Thank you, Ray, for continuing to collaborate with us even after your time at Maryland. I would like to thank other seniors for kindly welcoming me despite that we only shared a short time in the lab. I thank Prof. Roman Kuzmin for being willing to discuss with me whenever I ask. I am grateful to Dr. Nitish Mehta for kindly sharing the lecture notes for classes. I appreciate Dr. Aaron Somoroff for showing me how to fab on Sapphire substrates. I am thankful to Dr. Hanho Lee for kindly sharing his experience in lab and job hunting. Shukai Liu and Dr. Arunav Bordoloi joined the group around the same time as I did, and I thank them for jointly taking care of the lab after all the senior members had graduated or left in our second year. Hyunheung Cho was a junior working closely with me and sharing the loading in the gate projects. I particularly thank Hyunheung for helping me taking care of the lab and various responsibilities when I was busy on writing thesis and job hunting. I would also like to thank former members in Vlad's group who built up all the tools in the lab I relied on even though our time there did not overlap. I am especially grateful to Prof. Yen-Hsiang Lin, a former postdoc in the lab, for introducing me to the world of fluxonium and for his warm and thoughtful advice regarding my future career. I wish to thank Dr. Long Nguyen, a former graduate student in the lab, for his kindness in sharing his experience and offering helpful guidance during my search for postdoctoral positions. I am grateful to Prof. Ivan Pechenezhskiy, a former postdoc in the lab, for teaching me the knowledge of quasi particles and for sharing his experience in academia.

The support of our collaborators is appreciated. Dr. Yinqi Chen simulated our two-qubit dynamics and always helped me explore and identify the error sources in our system whenever I needed simulation support. I also learned a lot on how to collaborate effectively with theorists through our discussion. Prof. Maxim Vavilov offered many valuable suggestions and provided a lot of important feedback on the theory side of the gate projects. Prof. Chen Wang shared their experimental skills and experience in characterizing CNOT gates, which are very helpful. I sincerely thank you all for the insightful discussions we had.

Finally, I thank my beloved wife and soulmate, Ellie. Her unwavering support, cheering, funny moves, and love made the difficult times during my PhD life bearable. Ellie, I love you, and I look forward to a lifetime of happiness together.

Table of Contents

List of Tables

List of Figures

List of Symbols and Abbreviations

Latin letters

$\hat{a}, \hat{a}^\dagger$	Annihilation and creation operators
C	Capacitance
E_C	Charging energy
E_J	Josephson energy
E_L	Inductive energy
F	Gate fidelity
f	Frequency
g	Qubit-resonator coupling strength
H	Hamiltonian
J	Qubit-qubit coupling strength
J_C	Capacitive coupling strength
J_L	Inductive coupling strength
L	Inductance
L_J	Josephson inductance
L_i	Lindblad operator of decoherence process i
$\hat{n}$	Charge operator normalized by number of Cooper pairs
n_g	Offset charge
n_{th}	Thermal photon number
Q	Charge
$S_\lambda(\omega)$	Noise spectral density of noise source λ
$\vec{S}$	Bloch vector
T	Temperature
T_1	Energy relaxation time
T_2^E	Echo decay time
T_2^R, T_2^*	Ramsey decay time
t_f	Evolution time
$\hat{U}$	Unitary evolution operator
x_{qp}	normalized quasiparticle density
X	Pauli X matrix
Y	Pauli Y matrix
Z	Pauli Z matrix

Greek letters

α	Anharmonicity
$\beta(t)$	Time-dependent drive
$\bar{\beta}(t)$	Slowly-varying drive envelope
χ	Dispersive shift
δ	Detuning
δ_r	Transition–resonator detuning
$\mathcal{E}$	Gate error
ϵ_{ps}	Quantum phase slip energy
$\epsilon_{1(2)}$	Quantum phase slip energy of single (bi) fluxon tunneling
$\epsilon_{A(B)}$	External drive field of qubit A (B)
η	Complex ratio ϵ_B/ϵ_A
κ	Resonator linewidth (loss rate)
λ	Noise source
Ω	Rabi frequency
ω	Angular frequency
ϕ	Phase of drive
Φ	Magnetic flux
$\hat{\varphi}$	Phase operator
φ_{ext}	External flux bias normalized by reduced magnetic flux quantum
ρ	Density matrix
$\hat{\sigma}_+$	Raising operator
$\hat{\sigma}_-$	Lowering operator
$\hat{\sigma}_x^j$	Pauli-X operator for qubit j
$\hat{\sigma}_z^j$	Pauli-Z operator for qubit j
τ_c	Characteristic correlation time
θ	Phase accumulation
ξ	Interaction rates

Physical constants

e	Electron charge
h	Planck constant
$\hbar$	Reduced Planck constant
Φ_0	Magnetic flux quantum
ϕ_0	Reduced magnetic flux quantum

Abbreviations

AWG	Arbitrary Waveform Generator
CNOT	Controlled-NOT
cQED	Circuit Quantum Electrodynamics
CQPS	Coherent quantum phase slips
CR	Cross-Resonance
CX_{π}	Controlled-π Rotation Gate
CZ	Controlled-Z
DRAG	Derivative Removal by Adiabatic Gate
IFQ	Integer fluxonium qubit
IQ	In-phase, Quadrature
IRB	Interleaved Randomized Benchmarking
JJ	Josephson Junction
LC	Inductor Capacitor resonance mode
MIST	Measurement-Induced State Transitions
QEC	Quantum Error Correction
QND	Quantum Nondemolition
RB	Randomized Benchmarking
TLS	Two-level system
ZX	ZX interaction
ZZ	ZZ interaction

Citations to Published Work

Parts of Chapters 3 and 4 have appeared in the journal papers [1, 2, 3].

Chapter 1: Introduction

Among existing quantum platforms, superconducting circuits based on Josephson tunnel junctions [4] have emerged as a leading candidate for quantum computing. Within the circuit quantum electrodynamics platform [5], the larger scale quantum computing experiments rely almost exclusively on transmon qubits [6]. Despite the high coherence of transmon qubits, a notable drawback is their relatively weak anharmonicity (a few %), which can lead to leakage errors outside the computational subspace during gate operations. Leakage is a correlated error and thus a challenge for quantum error correction (QEC) [7], which provides a path to achieve practical quantum computing. A possible path to suppress leakage is to replace transmons with fluxonium qubits [8], which generally combine similarly long coherence time with a much stronger anharmonicity (over 100%) [1, 9, 10, 11, 12, 13, 14, 15, 16]. While scaling up, high-fidelity entangling gate operations is a key requirement for quantum computing [17]. A notable recent work experimentally demonstrating physical error below threshold of QEC surface code and exponential suppression of logical error [18] has identified two-qubit gate error as the dominant error source. For transmon, high-fidelity two-qubit gates are implemented using a time-varying qubit frequency [19, 20, 21, 22], or an all-microwave control [23, 24, 25, 26], or tunable couplers [27, 28, 29], or combinations of the above approaches [30]. However, all such gate schemes suffer from a relatively weak anharmonicity of transmon circuits. Promising initial demonstrations of entangling gates on a pair of fluxoniums are indeed based on their strongly anharmonic spectra [31, 32, 33, 34, 35, 36, 37, 38]. In this thesis, we explore novel schemes for both single- and two-qubit building blocks based on fluxonium qubits. In the single-qubit project, we investigate and operate a fluxonium qubit biased at zero magnetic flux, in contrast to the conventional operating point at half a flux quantum. In the two-qubit project, we couple two fluxonium qubits via inductive coupling, as opposed to the more commonly used capacitive coupling. We demonstrate high-fidelity gate operations in both platforms and thus the potential to be applied to multi-qubit quantum processors. The thesis is organized as follows. In Chapter 2, we review the fundamental theory of superconducting qubits, focusing on the control, readout, and coupling schemes of fluxonium along with the qubit performance in noisy environments. In Chapter 3, we demonstrate the equivalence of the integer- and the half-integer flux sweet spots with respect to the energy relaxation rate using an elementary model of flux quantization in a superconducting loop. We further describe the device and experimental characterization of the unconventional integer fluxonium qubit. In Chapter 4, we introduce an inductively coupled two-fluxonium system and its experimental verification of the nearly ideal transversely-coupled spin-1/2 Hamiltonian in the computational sub-space. We further describe the realization and benchmarking of the cross-resonance two-qubit gates, along with the error budget of both single- and two-qubit gate operations. In Chapter 5, we summarize the experimental work of this thesis and discuss the outlook to improve the performance of future devices based on fluxonium qubits.

Chapter 2: Fluxonium Theory

In this chapter, we introduce the core concepts and models of superconducting qubits. By incorporating nonlinearity through Josephson junctions (JJ) [4], superconducting circuits can host various types of qubits. We focus in particular on fluxonium qubits and their relevant context in this thesis, including fluxonium readout and multi fluxonium systems. The rapid progress in superconducting quantum computing has been driven by sustained improvements in qubit coherence times, which fundamentally limit the error rates of quantum processors. From initial coherence times on the order of nanoseconds in the Cooper pair box [39] to the millisecond coherence times in fluxonium [14], nearly six orders of magnitude improvement in T_2 have been achieved over the past two decades. We discuss dissipation arising from interactions with the environment, which helps illustrate the noise resilience of fluxonium qubits for achieving high coherence. Last but not least, we introduce the concept of various quantum gate operations, focusing on the schemes we apply in the experiments of this thesis. This chapter establishes the necessary background for understanding the details presented in Chapter 3 and 4.

2.1 Superconducting Circuits

2.1.1 Capacitor, Inductor, and Josephson Junction

In circuit quantum electrodynamics (cQED), there are three major building blocks: capacitor, inductor, and Josephson junction as shown in Fig. 2.1. A capacitor is characterized by its capacitance C and the charge Q accumulated on the capacitor, with the energy $Q^2/2C$. An inductor is characterized by its inductance L and the magnetic flux Φ threading through the inductor, with the energy $\Phi^2/2L$. We can also define two dimensionless variables, the number of Cooper pairs $n = Q/2e$ and the reduced flux $\varphi = \Phi/\phi_0$ with the electron charge e and the reduced flux quantum $\phi_0 = \Phi_0/2\pi = \hbar/2e$ (Φ_0 is flux quantum), rewriting the stored energies as $4E_C n^2$ and $E_L\varphi^2/2$ with charging energy $E_C = e^2/2C$ and inductive energy $E_L = {\phi_0}^2/L$.

A JJ consists of a thin insulating layer sandwitched between two layers of superconductors. Its properties can be described by the Josephson equations:

$$I = I_c \sin\varphi, \tag{2.1}$$

$$V = \phi_0 \frac{d\varphi}{dt}. \tag{2.2}$$

Here, I and V denote the current through junction and the voltage across it, respectively. I_c is the critical current indicating the largest current that can flow through the junction. φ is the superconducting phase difference across the junction. By taking the time-derivative of the first equation and combining it with the second equation, we can get

$$V = \frac{\phi_0}{I_c \cos\varphi} \frac{dI}{dt} = L_J \frac{dI}{dt}. \tag{2.3}$$

This gives us the inductance of a JJ

$$L_J = \frac{\phi_0}{I_c \cos\varphi}. \tag{2.4}$$

Accordingly, the JJ behaves like a non-linear inductor. We use the same symbol φ as the reduced flux since Eq. 2.2 indicates $V = d\Phi/dt$, which is the same voltage-flux relation of a linear inductor. This illustrates the equivalence of the two contexts and generalizes the language for both linear and non-linear inductors. It is noteworthy that the origin of this kinetic inductance lies in the inertia of electrons, distinguishing it from geometric inductance, which arises from the physical wire geometry such as a coil. The energy stored in the junction is given by:

$$E = \int IV dt = I_C \phi_0 \int \sin\varphi \, d\varphi = -E_J \cos\varphi, \tag{2.5}$$

where we have defined the Josephson energy $E_J = I_C \phi_0$. In this work, we use aluminum and aluminum oxides for superconductors and the insulating layers, respectively, to realize a JJ.

2.1.2 Resonator, Transmon, and Fluxonium

In this section, we introduce three common subsystems used in superconducting qubit circuits: the resonator, the transmon, and the fluxonium. Each is constructed from different combinations of the fundamental elements discussed in the previous section.

A resonator can be described by an inductor shunted by a capacitor as shown in Fig. 2.2

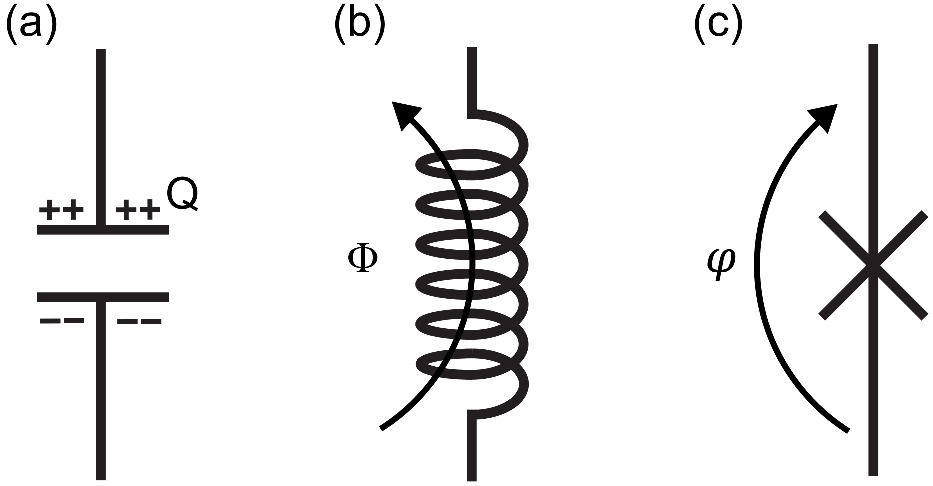

Figure 2.1: (a),(b),(c) The circuit of a capacitor, a inductor, a Josephson junction, respectively, characterized by charge Q, magnetic flux Φ, and phase difference φ.

(a). Its Hamiltonian is

$$\hat{\mathcal{H}} = 4E_C\hat{n}^2 + \frac{1}{2}E_L\hat{\varphi}^2, \tag{2.6}$$

where we have promoted the charge and flux variables to the quantum operators, $\hat{n}$ and $\hat{\varphi}$. Since $\dot{\Phi} = V$ and $\dot{Q} = I$, $\hat{n}$ and $\hat{\varphi}$ are canonically conjugate quantum operators satisfying the commutation relation $[\hat{\varphi}, \hat{n}] = i$, analogous to the momentum and position operators of a harmonic oscillator such as a rolling ball inside a quadratic potential well or a mass on a spring. Namely, $4E_C\hat{n}^2$ and $\frac{1}{2}E_L\hat{\varphi}^2$ are analogous to kinetic and potential energies, respectively. For the LC resonator, we can thus introduce the creation and annihilation operators, $\hat{a}^\dagger$ and $\hat{a}$, to rewrite the Hamiltonian $\hat{\mathcal{H}} = \hbar\omega\left(\hat{a}^\dagger\hat{a} + \frac{1}{2}\right)$ with resonant frequency $\omega = \sqrt{8E_LE_C}/\hbar = 1/\sqrt{LC}$. Accordingly, the eigenstates are equally-spaced with the energy difference of $\hbar\omega$. $\hat{n}$ and $\hat{\varphi}$ in terms of $\hat{a}^\dagger$ and $\hat{a}$ are

$$\hat{n} = \frac{i}{\sqrt{2}}\left(\frac{E_L}{8E_C}\right)^{\frac{1}{4}}\left(\hat{a}^\dagger - \hat{a}\right), \tag{2.7}$$

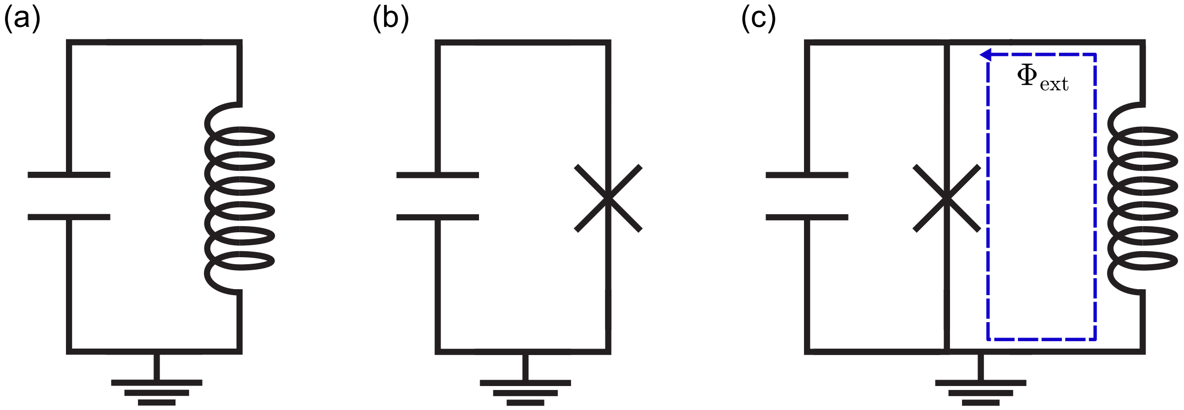

Figure 2.2: (a),(b),(c) The circuit of a resonator, a transmon, a fluxonium, respectively.

$$\hat{\varphi} = \frac{1}{\sqrt{2}} \left(\frac{8E_C}{E_L} \right)^{\frac{1}{4}} \left(\hat{a}^\dagger + \hat{a} \right). \tag{2.8}$$

Resonators are commonly applied in superconducting circuits, serving functions such as inter-qubit coupling, qubit state readout, and even acting as qubits themselves, as in the case of bosonic qubits [40].

If the linear inductor in a LC resonator is replaced by a JJ as shown in Fig. 2.2(b), the potential energy term becomes a cosine function and introduce nonlinearity into the circuit to form eigenenergies with unequal spacing as shown in Fig. 2.3(a). The lowest two states can then be used to define the qubit transition. This is possible because the anharmonicity $\alpha = \frac{(E_2-E_1)-(E_1-E_0)}{h}$ defined by the energies of the lowest three eigenstates becomes nonzero, allowing population confined within the logical subspace while driving the qubit transition. This circuit Hamiltonian is given by

$$4E_C(\hat{n} - n_g)^2 - E_J \cos\hat{\varphi}, \tag{2.9}$$

where n_g is the offset charge on the Cooper pair island, i.e., the upper isolated island of Fig.

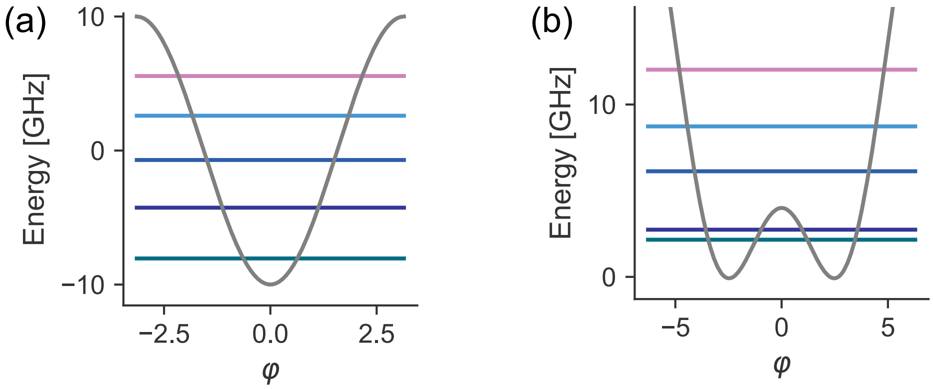

Figure 2.3: (a) The energy levels of a transmon with 0.2 GHz E_C and 10 GHz E_J, giving nonzero anharmonicity. (b) The energy levels of a fluxonium biased at half flux quantum with 1 GHz E_C, 1 GHz E_L, and 4 GHz E_J, giving stronger anharmonicity compared with a transmon. The figure plots are generated by scQubit [41].

2.2(b). The eigenenergy spectrum exhibits dispersion with respect to n_g, meaning the transition energy gaps between eigenstates are n_g dependent. Since n_g can fluctuate and cause decoherence, this charge noise has posed a long-standing challenge in the field. Increasing the ratio E_J/E_C can enter the system into the transmon regime and suppress the effect of n_g on the qubit transition energy, which is widely adopted against charge noise [6]. However, the suppression of charge noise comes at the cost of a lower anharmonicity, where the typical value of α/h is around 200 MHz, limiting the speed of gate operations.

By combining all three circuit elements, as shown in Fig. 2.2(c), a fluxonium circuit is formed, which has the potential to achieve stronger anharmonicity. The potential energy of a fluxonium is the sum of a cosine and a quadratic term, leading to the Hamiltonian

$$4E_C\hat{n}^2 + \frac{1}{2}E_L(\hat{\varphi} - \varphi_{\text{ext}})^2 - E_J\cos(\hat{\varphi}). \tag{2.10}$$

Here, $\varphi_{\text{ext}} = \Phi_{\text{ext}}/\phi_0$ comes from the flux quantization of a superconducting loop and corresponds to the external magnetic flux Φ_{ext} threading through the loop formed by the linear inductor and JJ. The allocation of φ_{ext} to the linear inductor term rather than the JJ term generalizes the case of time-dependent external flux [42]. Figure 2.3(b) shows the strongly anharmonic energy spectrum of a typical fluxonium biased at half flux quantum ($\varphi_{\text{ext}} = \pi$). Typically, the linear inductor in a fluxonium circuit is realized by incorporating a large number of identical JJs, often more than 100, forming a long JJ array in a loop as shown in Fig. 2.4. These chain JJs have much larger E_J than the single JJ in Fig. 2.2(c), indicating the phase difference across each chain JJs needs to be small for the lowest few eigenstates to avoid a huge potential energy. To better demonstrate the idea, we write down the energy of the junction array with N JJs based on the flux quantization of a superconducting loop

$$-NE_J^{\text{chain}} \cos\left(\frac{\hat{\varphi}}{N}\right) = -NE_J^{\text{chain}} \left(1 - \frac{1}{2}\left(\frac{\hat{\varphi}}{N}\right)^2\right) + O\left(\frac{\hat{\varphi}^4}{N^3}\right), \tag{2.11}$$

where higher order terms are negligible due to the large value of N. This leads to the energy of a linear inductor

$$\frac{1}{2}E_L\hat{\varphi}^2 = \frac{1}{2}\frac{E_J^{\text{chain}}}{N}\hat{\varphi}^2. \tag{2.12}$$

It is noteworthy that the self capacitance C_J^{chain} of each chain JJ and the stray capacitance to ground C_g can introduce unwanted energy terms. In order to make the first term of 2.11 valid, two assumptions must be satisfied [43]. First, $\exp\left(-\sqrt{8E_J^{\text{chain}}/E_C^{\text{chain}}}\right) \ll 1$ with $E_C^{\text{chain}} = e^2/2C_J^{\text{chain}}$ is required to suppress the phase slips across each chain JJ as discussed in the section of pure dephasing mechanism. Second, $C_J^{\text{chain}}/C_g \gg N$ makes the chain resonance mode frequency much higher than the plasma frequency of each chain JJ $\sqrt{8E_J^{\text{chain}}E_C^{\text{chain}}}/h$ so that we can ignore the ef-

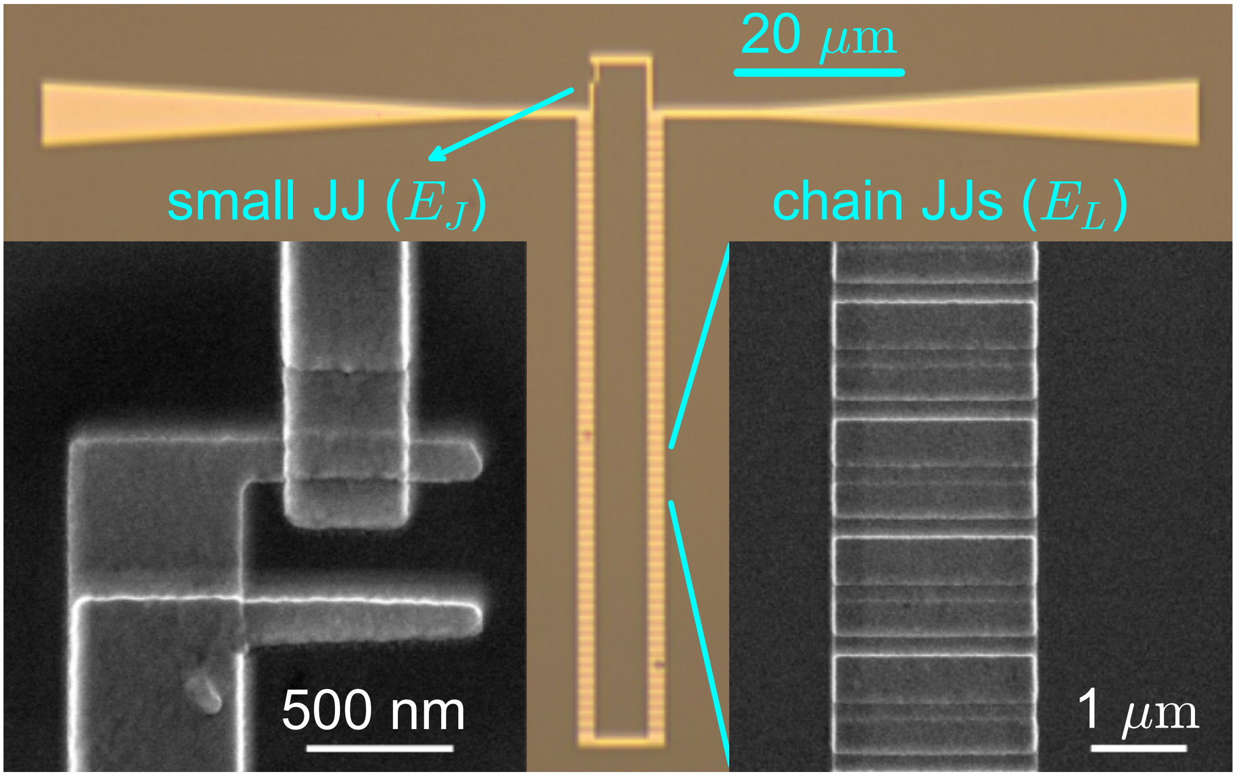

Figure 2.4: The microscope photo of a single fluxonium. The upper small JJ determines the value of E_J, while the lower chain of large JJs corresponds to E_L. The design of triangular pads helps us control the value of E_C, while the junction capacitance also contributes to E_C. The insets show the SEM images of small JJ and chain JJs, fabricated with Dolan bridge technique to achieve a Al-AlOx-Al structure.

fect of this transmission line resonator like chain mode. Next, we examine the fluxonium properties and decoherence mechanisms to see whether a fluxonium can combine strong anharmonicity with high coherence, making it a promising building block.

2.2 Transition matrix elements

In addition to the transition frequency, it is also important to examine the transition matrix elements including higher energy levels and transitions, as they determine how a qubit couples to other systems such as the readout resonator, neighboring qubits, and the environment. For a

Hamiltonian having the form $\hat{\mathcal{H}} = 4E_C\hat{n}^2 + \hat{V}(\hat{\varphi})$, we can derive the relation between the charge matrix elements $\langle j|\hat{n}|i\rangle$ and the phase matrix elements $\langle j|\hat{\varphi}|i\rangle$ for the transition from state i to state j by checking the commutation relation

$$[\hat{\mathcal{H}}, \hat{\varphi}] = [4E_C\hat{n}^2, \hat{\varphi}] = -8iE_C\hat{n} \tag{2.13}$$

and its matrix element

$$\langle j|[\hat{\mathcal{H}}, \hat{\varphi}]|i\rangle = \langle j|(\hat{\mathcal{H}}\hat{\varphi} - \hat{\varphi}\hat{\mathcal{H}})|i\rangle = (E_j - E_i)\langle j|\hat{\varphi}|i\rangle. \tag{2.14}$$

This gives

$$\langle j|\hat{n}|i\rangle = \frac{i\hbar\omega_{ij}}{8E_C}\langle j|\hat{\varphi}|i\rangle, \tag{2.15}$$

which is important for understanding different coupling schemes.

Fluxonium exhibits a highly anharmonic spectrum and non-trivial selection rules compared to the transmon, allowing transitions between non-adjacent energy levels. While the typical operating point is at half a flux quantum, tuning away from this point alters the potential landscape and consequently the wavefunction parity. This enables a distinct eigen energy spectrum and transition matrix elements that vary with qubit parameters across different flux bias points [44]. Figure 2.5 shows the spectrum, matrix elements, and wavefunctions of a fluxonium with E_J, E_C, and E_L similar to the device measured in this thesis.

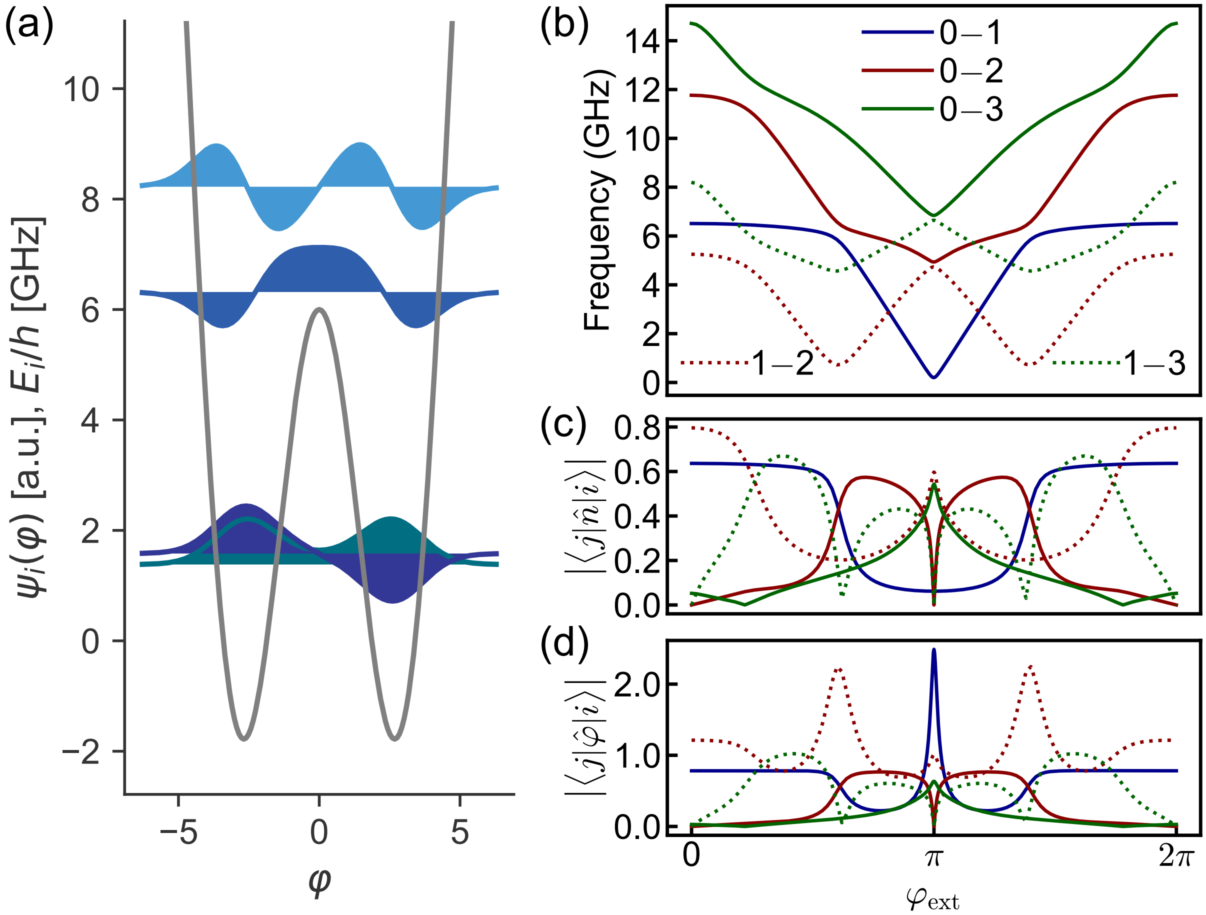

Figure 2.5: The fluxonium wavefunctions, energy spectrum, and matrix elements of the lowest four eigenstates with E_J = 6 GHz, E_L = 1 GHz, and E_C = 1 GHz. (a) The wavefunctions and eigenenergies biased at half flux quantum ($\varphi_{\text{ext}} = \pi$) along with the corresponding potential landscape, generated by scQubit [41]. (b),(c),(d) The energy spectrum, charge matrix elements, phase matrix elements across different external flux bias, respectively. At $\varphi_{\text{ext}} = \pi$, 0-2 and 1-3 matrix elements are zero due to the even parity as shown in (a).

2.3 Dispersive Readout

A resonator is commonly used to readout a superconducting qubit, typically via dispersive coupling to enable quantum nondemolition (QND) measurement [45]. The Hamiltonain of this readout scheme can be described by $\hat{\mathcal{H}} = \hat{\mathcal{H}}_q + \hat{\mathcal{H}}_r + \hat{V}_{qr}$, where $\hat{\mathcal{H}}_q$ and $\hat{\mathcal{H}}_r = \hbar\omega_r\left(\hat{a}^\dagger\hat{a} + \frac{1}{2}\right)$ are the qubit and resonator Hamiltonian, respectively. If they are capacitively coupled, the qubit-resonator coupling term is

$$\hat{V}_{qr} = ig_n(\hat{a}^\dagger - \hat{a})\hat{n}_q \tag{2.16}$$

with coupling strength g_n and the charge operator of qubit $\hat{n}_q$. $\hat{V}_{qr}$ can be treated as a perturbative term in the dispersive regime, where $|g_n\langle j|\hat{n}_q|i\rangle| \ll |\hbar(\omega_{ij} - \omega_r)|$ for the transitions $|i\rangle - |j\rangle$ of the superconducting qubit, typically a multilevel artificial atom. Accordingly, we can estimate the resonator frequency shift when the qubit is at $|i\rangle$ by second order perturbation theory [43]:

$$\chi_i = {g_n}^2 \sum_{j \neq i} |\langle j|\hat{n}_q|i\rangle|^2 \frac{2\omega_{ij}}{\omega_{ij}^2 - \omega_r^2}. \tag{2.17}$$

In experiments, this shift provides a frequency shift conditional on the qubit states

$$\chi_{10} = \chi_1 - \chi_0 = {g_n}^2 \left(\sum_{j \neq 1} |\langle j|\hat{n}_q|1\rangle|^2 \frac{2\omega_{1j}}{{\omega_{1j}}^2 - \omega_r^2} - \sum_{j \neq 0} |\langle j|\hat{n}_q|0\rangle|^2 \frac{2\omega_{0j}}{{\omega_{0j}}^2 - \omega_r^2} \right), \tag{2.18}$$

which is called dispersive shift and enables us to distinguish qubit states by measuring the response of resonator. Fig. 2.6 demonstrates the characteristics of the transmission coefficient S_{21} for a two port resonator, which is used to readout our qubits.

Even though the qubit frequency of a fluxonium is low and usually far-detuned from the

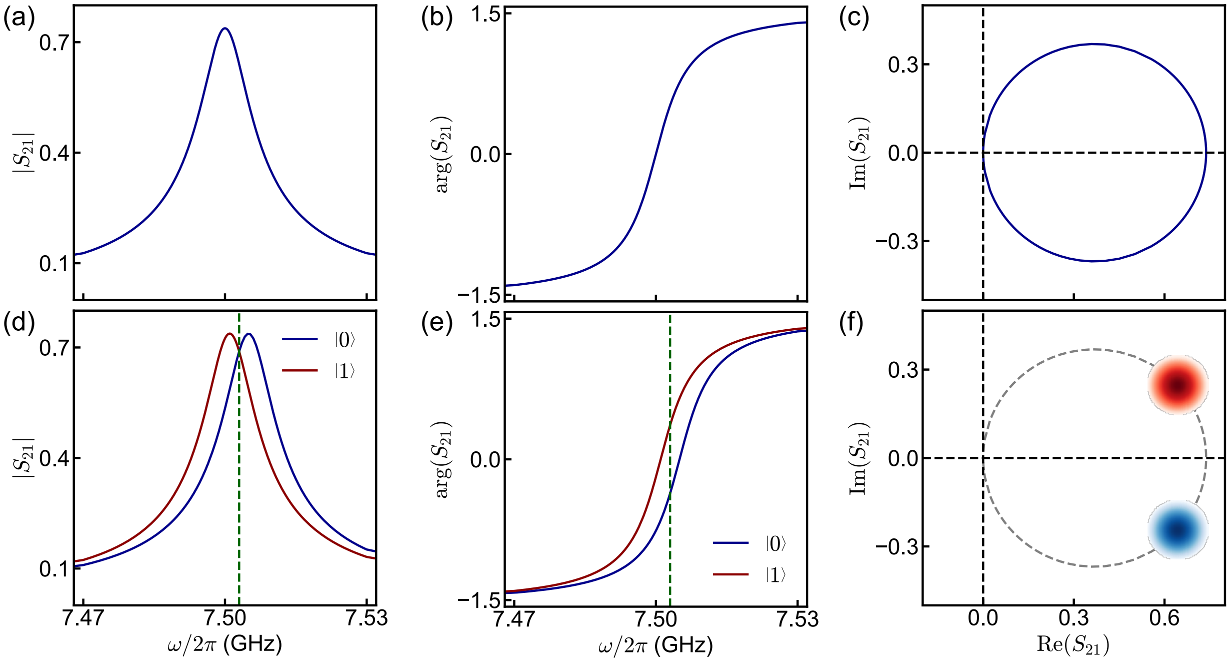

Figure 2.6: Transmission coefficient S_{21} of a two port resonator with frequency centered at 7.5 GHz. (a),(b),(c) The amplitude $|S_{21}|$, phase $\arg(S_{21})$, complex plane (IQ plane) response of a bare resonator S_{21} at different drive frequencies, respectively. (d),(e),(f) The amplitude $|S_{21}|$, phase $\arg(S_{21})$, complex plane (IQ plane) response of a resonator S_{21} coupled to a qubit at different drive frequencies, respectively. The blue and red colors correspond to qubit state at $|0\rangle$ and $|1\rangle$, respectively. The resonator frequency shifts by different amounts conditional on the qubit states, leading to a dispersive shift χ_{01} = 4 MHz for example as shown in (d). The blobs in (f) corresponds to the readout frequency indicated by the dark green line in (d), visualizing the different responses conditional on the qubit states with a uncertainty due to noise.

readout resonator frequency, the dispersive shift can still be large due to the contribution from the higher levels as shown in Eq. 2.18. Taking our devices for example, the 0-3 transition of fluxonium at half flux quantum has a large charge matrix elements as shown in 2.5 (c), enabling a large dispersive shift if we place the readout resonator frequency near the 0-3 frequency. 1-3 transtion has frequency similar to 0-3 but a much smaller matrix elements, making 0-3 the dominant contribution. The coupling strength g_n and the detuning $\omega_{03} - \omega_r$ need to be properly designed to avoid non-QND effects such as measurement induced state transitions (MIST), which remains an active area of research in the field for faster qubit readout.

2.4 Relaxation and Decoherence Mechanisms

Noise from the environment leads to decoherence and the loss of quantum information in qubits, including energy relaxation and dephasing. The dynamics of a qubit under such effects can be described by the Lindblad master equation [45]

$$\frac{d\rho}{dt} = -\frac{i}{\hbar}[\hat{\mathcal{H}}, \rho] + \sum_i \mathcal{D}[\hat{L}_i](\rho) \tag{2.19}$$

with the dissipator $\mathcal{D}[\hat{L}_i](\rho)$ capturing the decoherence processes:

$$\mathcal{D}[\hat{L}_i](\rho) = \hat{L}_i \rho \hat{L}_i^\dagger - \frac{1}{2}\hat{L}_i^\dagger \hat{L}_i \rho - \frac{1}{2}\rho \hat{L}_i^\dagger \hat{L}_i. \tag{2.20}$$

These processes reduce the purity Tr(ρ^2) of the density matrix ρ that describes the qubit state. $\hat{L}_i$ are the Lindblad operators including $\hat{L}_1 = \sqrt{\Gamma_\downarrow}\,\hat{\sigma}_-$ for qubit emission, $\hat{L}_2 = \sqrt{\Gamma_\uparrow}\,\hat{\sigma}_+$ for qubit absorption, and $\hat{L}_3 = \sqrt{\frac{\Gamma_\phi}{2}}\,\hat{\sigma}_z$ for pure dephasing. These mechanisms are discussed in further detail in the following sections, where we examine whether fluxonium can combine strong anharmonicity with high coherence, the most significant advantage of fluxonium.

2.4.1 Energy relaxation mechanisms

For energy relaxation, the associated Linblad operators are $\hat{L}_1$ and $\hat{L}_2$. Combined with a simple qubit Hamiltonian $\hat{\mathcal{H}} = \frac{\hbar\omega_{01}}{2}\hat{\sigma}_z$ in Eq. 2.19, we get the rate equations (a special case of optical Bloch equations):

$$\frac{d(\rho_{11}-\rho_{00})}{dt} = \frac{d\langle\hat{\sigma}_z\rangle}{dt} = -\Gamma_1\left(\langle\hat{\sigma}_z\rangle - \langle\hat{\sigma}_z\rangle_{\text{th}}\right), \tag{2.21}$$

$$\frac{d\rho_{10}}{dt} = -i\omega_{01}\rho_{10} - \frac{\Gamma_1}{2}\rho_{10}. \tag{2.22}$$

Here, $\Gamma_1 = \Gamma_\uparrow + \Gamma_\downarrow$ is the energy relaxation rate. $\langle\hat{\sigma}_z\rangle_{\text{th}} = (\Gamma_\uparrow - \Gamma_\downarrow)/(\Gamma_\uparrow + \Gamma_\downarrow)$ is the thermal equilibrium value of the Z component of the qubit Bloch vector, coming from $\frac{\Gamma_\uparrow}{\Gamma_\downarrow} = \frac{\rho_{11}^{\text{th}}}{\rho_{00}^{\text{th}}} = e^{-\frac{\hbar\omega_{01}}{k_B T}}$ shown in optical Bloch equations. The relaxation rate Γ_1 indicates how fast $\langle\hat{\sigma}_z\rangle$ decays to $\langle\hat{\sigma}_z\rangle_{\text{th}}$, which also introduce a decoherence rate $\Gamma_1/2$ denoting how fast the coherence ρ_{10} decays.

The relaxation process can be modeled by a noise source with amplitude $\delta v(t)$ coupled to a qubit via $\hat{\sigma}_x$ with coupling constant A, which causes transitions through perturbation

$$\hat{V} = A\delta v(t)\hat{\sigma}_x \tag{2.23}$$

[46]. If the initial state is in the ground state, the coefficient of excited state at time t_f is

$$c_e(t_f) = -\frac{iA}{\hbar}\int_0^{t_f} dt\, e^{i\omega_{01}t}\delta v(t), \tag{2.24}$$

derived from time-dependent perturbation theory. The corresponding population is

$$p_e(t_f) = |c_e(t_f)|^2 = \frac{A^2}{\hbar^2}\int_0^{t_f}\int_0^{t_f} dt\, dt'\, e^{-i\omega_{01}(t-t')}\delta v(t)\delta v(t'). \tag{2.25}$$

After taking an ensemble average over time t_f and performing change of variables $\tau = t - t'$, we get the correlation function $\langle \delta v(t)\delta v(t-\tau)\rangle$ within the integral, which decays to zero after a characteristic correlation time $\tau = \tau_c$. We further apply Markovian approximation $\tau_c \ll t_f$, indicating that the noise is uncorrelated with no memory effect. The disturbances from the noise are thus random and independent of each other. This leads to the approximation setting the bounds in the last integral to infinity and achieve

$$\langle p_e(t_f)\rangle = \frac{A^2}{\hbar^2}\int_0^{t_f} dt \int_{-\infty}^{\infty} d\tau\, e^{-i\omega_{01}\tau}\, \langle \delta v(\tau)\delta v(0)\rangle = \frac{A^2}{\hbar^2} S_v(-\omega_{01}) t_f, \tag{2.26}$$

where we've applied time translational invariance and defined the noise spectral density

$$S_v(\omega) = \int_{-\infty}^{\infty} d\tau\, e^{i\omega\tau}\langle \delta v(\tau)\delta v(0)\rangle, \tag{2.27}$$

being the Fourier transform of the correlation function. Accordingly, we get the transition rate of qubit absorption

$$\frac{d\langle p_e(t_f)\rangle}{dt_f} = \Gamma_\uparrow = \frac{A^2}{\hbar^2} S_v(-\omega_{01}). \tag{2.28}$$

Similarly, if the initial state is in the excited state, we achieve the transition rate of qubit emission

$$\Gamma_\downarrow = \frac{A^2}{\hbar^2} S_v(\omega_{01}) \tag{2.29}$$

by the same algebra.

The derivation above gives the general form of the Fermi's Golden rule:

$$\Gamma_{ij}^{\lambda} = \frac{1}{\hbar^2} \left| \langle j|\hat{O}|i\rangle \right|^2 S_{\lambda}(\omega_{ij}), \tag{2.30}$$

the relaxation rate from state i to j due to noise source λ that coupled through operator $\hat{O}$. This concept provides a framework for understanding the various noise sources that contribute to the degradation of the relaxation time $T_1 = 1/\Gamma_1$ in superconducting qubits. Below, we outline several typical sources commonly encountered in superconducting circuits and summarize the corresponding parameters observed in our fluxonium devices [11].

2.4.1.1 Dielectric loss

Dielectric loss arises from defects present in lossy dielectric materials near the circuits [47]. These defects are observed to behave like two-level systems (TLS), which can couple to superconducting qubits and exchange energy with them, leading to relaxation. This mechanism can be modeled by filling qubit capacitor with lossy dielectric materials with complex dielectric constant $\epsilon = \epsilon_1 + i\epsilon_2$, giving $C_{\text{eff}} = C\,(1 + i\tan\delta_C)$ with the effective loss tangent

$$\tan\delta_C = \frac{\epsilon_2}{\epsilon_1}. \tag{2.31}$$

The corresponding relaxation rate between state i and j is

$$\Gamma_{ij}^{\text{diel}} = \frac{8E_C}{\hbar} \left|\langle j|\hat{n}|i\rangle\right|^2 \tan\delta_C \left[\coth\left(\frac{\hbar\omega_{ij}}{2k_BT}\right) + 1\right] \tag{2.32}$$

[48], where the last term with temperature T dependence accounts for the stimulated emission due to the thermal photons of the oscillator bath model, which also includes the effect of the discussed excitation rate considering qubit absorption in the previous section. For a real sample that has different materials and multiple interfaces, we can define $\tan\delta_C = \sum_i p_i \tan\delta_i$ where p_i is the participation ratio of material i with loss tangent $\tan\delta_i$. Compared to transmon, fluxonium has a very low qubit frequency and thus a small $|\langle j|\hat{n}|i\rangle|$ following Eq. 2.15, suppressing the dielectric loss channel that is dominant in superconducting qubits. This is the main advantage and reason for fluxonium to achieve high coherence. Alternatively, one can also suppress $|\langle j|\hat{\varphi}|i\rangle|$ instead of frequency to achieve a small $|\langle j|\hat{n}|i\rangle|$ following Eq. 2.15, which is shown experimentally in Chapter 3. The estimated loss tangent in our lab is $\tan\delta_C = 10^{-6} - 10^{-5}$, which is the main source limiting our T_1.

2.4.1.2 Quasiparticle

Breaking Cooper pairs generates unpaired electrons, which are called quasiparticles that can induce relaxation when they tunnel through the JJs. The corresponding relaxation rate is

$$\Gamma_{ij}^{\mathrm{qp}} = \frac{8E_J}{\pi\hbar}\sqrt{\frac{2\Delta}{\hbar\omega_{ij}}}\left|\langle j|\sin\left(\frac{\hat{\varphi}-\varphi_{\mathrm{ext}}}{2}\right)|i\rangle\right|^2 x_{\mathrm{qp}}, \tag{2.33}$$

where Δ is the superconducting gap, and x_{qp} refers to the quasiparticle density normalized by Cooper pair density. The tunneling events across chain JJs are the main loss channel rather than the small JJ because of the wavefunction parity biased at half flux quantum as shown in Fig. 2.5 (a). The x_{qp} observed in experiments is usually much higher than the thermal equilibrium case and can lead to double exponential T_1 decay [49], while the estimated x_{qp} is below 10^{-7} and not the main relaxation mechanism in our lab according to the T_1 measured in a double-loop device across different flux bias [11]. Another possible loss channel due to quasiparticles is the inductive loss characterized by the inductive loss tangent $\tan\delta_L$, which is analogous to $\tan\delta_C$ discussed in the previous paragraph. The same Γ_1 gives the relation $\frac{\tan\delta_L}{\tan\delta_C} = \frac{(\hbar\omega_{ij})^2}{8E_C E_L}$ and indicates the inductive loss is less severe than quasiparticle tunneling in the chain JJs assuming $\tan\delta_L = x_{qp}$. High energy photons with frequency comparable to superconducting gap (over 100 GHz) is one of the sources inducing these non-equilibrium quasiparticles, indicating the importance of high frequency filters in the measurement lines.

2.4.1.3 1/f flux noise

1/f flux noise is one of the dominant noise sources causing the relaxation of flux qubits, so it is important to investigate its effect on fluxonium which has a similar structure. Following Eq. 2.10, we can see that flux noise $\delta\varphi_{\text{ext}}$ couple to the qubit through the Hamiltonian term $E_L\delta\varphi_{\text{ext}}\hat{\varphi} = \frac{\hbar}{2eL}\delta\Phi_{\text{ext}}\hat{\varphi}$, with which the Fermi's golden rule gives

$$\Gamma_{ij}^{\Phi} = \frac{1}{4e^2L^2}\left|\langle j|\hat{\varphi}|i\rangle\right|^2 S_\Phi(\omega_{ij}), \quad S_\Phi(\omega) = \frac{2\pi(S_\Phi^{1/f})^2}{|\omega|^\mu}. \tag{2.34}$$

The characterized noise amplitude in our lab is $S_{\Phi_{\text{ext}}}^{1/f} = 10^{-6} - 10^{-5}\,\Phi_0$, and the corresponding T_1 limit with the power $\mu = 1$ is above 10 ms, indicating this is not the dominant mechanism for fluxonium relaxation in contrast to flux qubits. This is because of the relatively large inductance L ($\sim$ 100 nH) of fluxonium.

2.4.1.4 Purcell effect

When the qubit is coupled to a lossy resonator, energy exchange between the two can lead to qubit energy dissipation into the environment, a phenomenon known as the Purcell effect [50]. The Purcell decay rate can be approximated as

$$\Gamma_{ij}^{\mathrm{Purcell}} \approx {g_O}^2 \left|\langle j|\hat{O}|i\rangle\right|^2 \frac{\kappa}{{\delta_r}^2} \tag{2.35}$$

in the dispersive regime, where the detuning with respect to the resonator frequency δ_r is much larger than the qubit-resonator coupling strength g. $\hat{O}$ can be $\hat{n}$ or $\hat{\varphi}$, depending on how the qubit couples to the resonator with coupling strength g_n or g_φ. κ is the loss rate of the resonator. Thanks to the large detuning δ_r enabled by the readout scheme of fluxonium, the Purcell limited T_1 due to the readout resonator can easily exceed 10 ms for our typical readout parameters.

2.4.2 Pure dephasing mechanisms

Pure dephasing only introduces dephasing rate without causing energy relaxation, which is often modeled by random phase accumulation between qubit states $|0\rangle$ and $|1\rangle$. This process indicates that we lose track of the qubit phase, which reduces coherences ρ_{10}, ρ_{01} and the length of the Bloch vector after averaging the random fluctuation. Pure dephasing can arise from various mechanisms, such as fluctuations in the transition frequency and relaxation processes of neighboring transitions. To better understand pure dephasing, we once again consider a simple qubit Hamiltonian in Eq. 2.19 but with a noise causing the fluctuation of qubit frequency $\delta\omega$, leading to

$$\hat{\mathcal{H}} = \frac{\hbar}{2} \left(\bar{\omega}_{01} + \delta\omega(t)\right) \hat{\sigma}_z. \tag{2.36}$$

Following Eq. 2.22, we get

$$\rho_{10}(t_f) = \rho_{10}(0) e^{(-i\bar{\omega}_{01} - \frac{\Gamma_1}{2})t_f - i\int_0^{t_f} \delta\omega(t)dt}. \tag{2.37}$$

We next Taylor expand $\delta\omega(t)$ and assume that the fluctuation is small:

$$\delta\omega(t) = \sum_{\{\lambda\}} \left(\frac{\partial\omega_{01}}{\partial\lambda} \delta\lambda(t) + O(\delta\lambda(t)^2) \right) \tag{2.38}$$

Here, $\{\lambda\}$ is the set of noise sources that cause $\delta\omega(t)$. For example, one common λ is the external flux Φ_{ext}, corresponding to the flux noise $\delta\Phi_{\text{ext}}$. The integral term in Eq. 2.37 now reads $-i\sum_{\{\lambda\}} \frac{\partial\omega_{01}}{\partial\lambda} \int_0^{t_f} \delta\lambda(t)dt$. After taking an ensemble average of Eq. 2.37 over time t_f, the contribution from each source λ is isolated and characterized by the two-time correlation function as

$$\langle e^{-i\frac{\partial\omega_{01}}{\partial\lambda}\int_0^{t_f}\delta\lambda(t)dt} \rangle = e^{-\frac{1}{2!}\left(\frac{\partial\omega_{01}}{\partial\lambda}\right)^2 \int_0^{t_f} dt \int_0^{t_f} dt' \langle\delta\lambda(t)\delta\lambda(t')\rangle}, \tag{2.39}$$

representing the extra decay of coherence due to noise source λ. Here, we've applied the identity $\langle e^P \rangle = e^{\langle P\rangle + (\langle P^2\rangle - \langle P\rangle^2)/2! + O(\langle P^3\rangle)/3! + \dots}$ assuming the noise $\delta\lambda(t)$ is Gaussian distributed, such that $\langle\delta\lambda(t)\rangle$ and higher order multi-time correlation functions are zero. Finally, applying time translational invariance and the fact that $\langle\delta\lambda(t-t')\delta\lambda(0)\rangle = \int_{-\infty}^{\infty} \frac{d\omega}{2\pi} e^{-i\omega(t-t')} S_\lambda(\omega)$ from the inverse Fourier transform of Eq. 2.27, we get

$$\int_0^{t_f} dt \int_0^{t_f} dt' \, \langle \delta\lambda(t)\delta\lambda(t')\rangle = {t_f}^2 \int_{-\infty}^{\infty} \frac{d\omega}{2\pi} S_\lambda(\omega) W(\omega, t_f). \tag{2.40}$$

The dimensionless weighting function

$$W(\omega, t_f) = \frac{1}{{t_f}^2} \left| \int_0^{t_f} dt \, e^{-i\omega t} \right|^2 = \frac{\sin^2(\omega t_f/2)}{(\omega t_f/2)^2} \tag{2.41}$$

serves as a filter function to shape the noise spectrum seen by the qubit. Let us first consider the simple example of white noise: $S_\lambda(\omega) = S_\lambda^{\text{white}}$, which is a constant amplitude independent of ω within $[0, 2\pi/\tau_c]$. Using $\int_{-\infty}^{\infty} dx \, \frac{\sin^2 x}{x^2} = \pi$, Eq. 2.39 becomes $e^{-\Gamma_\phi t_f}$, demonstrating the pure dephasing rate

$$\Gamma_\phi = \left(\frac{\partial \omega_{01}}{\partial \lambda}\right)^2 \frac{S_\lambda^{\text{white}}}{2}. \tag{2.42}$$

The flat spectrum of white noise corresponds to a correlation function $\langle \delta\lambda(\tau)\delta\lambda(0)\rangle = S_\lambda^{\text{white}}\delta(\tau)$, indicating that the shorter the correlation time τ_c, the broader the noise spectrum $S_\lambda(\omega)$. The exponential decay profile of pure dephasing is consistent with the results of plugging the Lindblad operator $\hat{L}_3$ into the Lindblad master equation, leading to the total decoherence rate $1/T_2 = \Gamma_2 = \frac{\Gamma_1}{2} + \Gamma_\phi$ derived from Eq. 2.37. However, Eq. 2.39 and 2.40 denote that the noise spectrum shape the decay profile, which can be non-exponential sometimes when $S_\lambda(\omega)$ is ω dependent. In the following sections below, we highlight a few pure dephasing mechanisms commonly encountered in superconducting circuits.

2.4.2.1 Dynamical decoupling

Before introducing other types of noise sources that have longer τ_c and thus ω dependent $S_\lambda(\omega)$, we first elaborate the measurement techniques that can characterize and mitigate them. The pulse sequences characterizing T_1 and T_2 are shown in Fig. 2.7. The derivation above considers free induction, which can be measured by a Ramsey sequence corresponding to the weighting function in Eq. 2.41. This measurement also extracts qubit frequency with high accuracy determined by T_2, as illustrated in Chapter 4. A spin echo sequence [51] add a short π-pulse in the middle of a Ramsey sequence, reversing the small frequency drift in the interval $[0, t_f/2]$ and canceling it out with the second half $[t_f/2, t_f]$. This leads to the weighting function

$$\begin{aligned} W(\omega, t_f) &= \frac{1}{{t_f}^2}\left|\int_0^{t_f/2} dt\, e^{-i\omega t} - \int_{t_f/2}^{t_f} dt\, e^{-i\omega t}\right|^2 = \frac{1}{\omega^2 {t_f}^2}\left|2e^{i\omega t_f/2} - e^{i\omega t_f} - 1\right|^2 \\ &= \tan^2\left(\frac{\omega t_f}{4}\right)\frac{\sin^2(\omega t_f/2)}{(\omega t_f/2)^2}, \end{aligned} \tag{2.43}$$

where the extra factor $\tan^2\left(\frac{\omega t_f}{4}\right)$ filters out the low frequency noise of $S_\lambda(\omega)$. The coherence time T_2^E measured by this echo sequence is usually the more important $T_2 = 1/\Gamma_2$. This is because the total free evolution time t_f in pulse sequences determine the frequency window of filter function $W(\omega, t_f)$. In contrast, Ramsey sequences are always sensitive to the low frequency noise coming from the long measurement time regardless of the choice of t_f. The prolonged time scale of the total measurement duration is few orders longer than t_f and often beyond the regime of interest, which also makes the Ramsey coherence time T_2^R typically shorter than T_2^E if the noise spectrum is not white and shows 1/f behavior as discussed in the next section. This can be understood as the result of averaging multiple oscillations with different frequencies, which

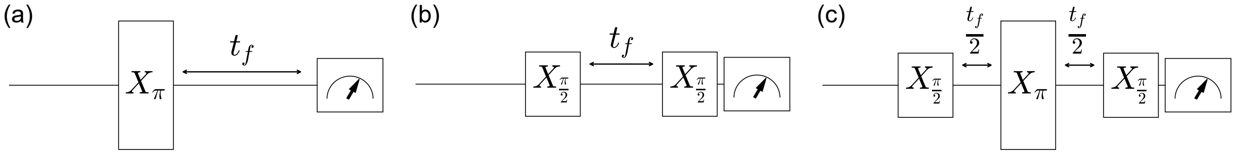

Figure 2.7: Pulse sequences of relaxation time T_1 and decoherence time T_2 measurements, where X_π and $X_{\frac{\pi}{2}}$ correspond to π and $\frac{\pi}{2}$ rotation with respect to the X axis of the Bloch sphere, respectively. (a) T_1 sequence measuring relaxation rate. (b),(c) Ramsey sequence, echo sequence for decoherence rate measurements, respectively.

leads to a faster decay profile.

The Carr-Purcell-Meiboom-Gill (CPMG) sequence [52, 53] further generalizes the echo sequence by incorporating N π-pulses, separating the evolution time t_f into same durations t_f/N or $t_f/(N+1)$ to make sure the number of durations are even and can cancel out higher frequency noise. Taking a odd $N = 2n - 1$ for example, Eq. 2.43 is generalized to

$$W(\omega, t_f) = \frac{1}{\omega^2 {t_f}^2} \left| 2e^{i\omega t_f/2n} - e^{i\omega t_f} - 1 \right|^2 = \tan^2\left(\frac{\omega t_f}{4n}\right) \frac{\sin^2(\omega t_f/2)}{(\omega t_f/2)^2}, \tag{2.44}$$

where the extra factor $\tan^2\left(\frac{\omega t_f}{4n}\right)$ further moves the window of filter function $W(\omega, t_f)$ to higher frequency range as N increases. We note that Ramsey, spin echo, and CPMG measurements yield the same decoherence rate for white noise, which has a flat noise spectrum and is therefore insensitive to the specific form of the filter function $W(\omega, t_f)$.

2.4.2.2 1/f noise

A 1/f behavior and similar spectral dependence is observed in the $S_\lambda(\omega)$ of various noise sources in superconducting circuits, including flux noise, charge noise, and critical current noise.

We model the noise with

$$S_\lambda(\omega) = \frac{2\pi(S_\lambda^{1/f})^2}{|\omega|^\mu}. \tag{2.45}$$

Considering the simple case with power $\mu = 1$, the decay profile Eq. 2.39 becomes a Gaussian form $e^{-(\Gamma_\phi t_f)^2}$. If we measure the decay rate with a Ramsey sequence, the approximated

$$\Gamma_\phi^{\text{Ramsey}} \approx \left(\frac{\partial\omega_{01}}{\partial\lambda}\right) S_\lambda^{1/f}\sqrt{\ln(t_m/t_f)}, \tag{2.46}$$

where t_m is the total measurement time and indicates a shorter T_2^{Ramsey} after a long measurement for averaging. This is different from the case of white noise, because our measurement frequency band is actually limited by t_m. Fluctuation with frequency $< 1/t_m$ are not effective, and this low frequency bound affects the $\Gamma_\phi^{\text{Ramsey}}$ due to 1/f noise more because the noise power is stronger at low frequency, meaning that increasing t_m can shorten the measured T_2^{Ramsey} a lot compared to white noise. The spin echo decay envelope gives the pure dephasing rate

$$\Gamma_\phi^{\text{Echo}} = \left(\frac{\partial\omega_{01}}{\partial\lambda}\right) S_\lambda^{1/f}\sqrt{\ln(2)} \tag{2.47}$$

Taking the 1/f flux noise in our lab for example, the characterized noise amplitude $S_{\Phi_{\text{ext}}}^{1/f} = 10^{-6} - 10^{-5}\,\Phi_0$.

From the previous derivation, we can see that the pure dephasing rates depend on $\frac{\partial\omega_{01}}{\partial\lambda}$, so it is common in experiments to bias the qubit at the noise-insensitive sweet spot where $\frac{\partial\omega_{01}}{\partial\lambda} = 0$ such as $\frac{\partial\omega_{01}}{\partial\Phi_{\text{ext}}} = 0$ for example. In this case, we need to take the second-order terms in Eq. 2.38

into account:

$$\delta\omega(t) = \sum_{\{\lambda\}} \left(\frac{\partial^2 \omega_{01}}{\partial \lambda^2} \, \delta\lambda(t)^2 + O(\delta\lambda(t)^3) \right) \tag{2.48}$$

The decay profile is complicated in this case but can be approximated as the product of a power law dominant at short time scale and a exponential law dominant at long time scale with $\Gamma_\phi^{(2)} \approx \frac{\partial^2 \omega_{01}}{\partial \lambda^2} (S_\lambda^{1/f})^2$ [54]. Taking the 1/f flux noise in our lab for example, this corresponds to 10 - 100 ms T_2 for our typical fluxonium parameters with the second order flux sensitivity estimated using the fluxon model in Chapter 3:

$$\frac{\partial^2 \omega_{01}}{\partial \Phi^2} \approx \frac{4\pi^2}{{\phi_0}^2} \frac{{E_L}^2}{\hbar\omega_{01}}. \tag{2.49}$$

2.4.2.3 Shot noise

In cQED, a resonator is often applied to readout a qubit, relying on the fact that the excitation of qubit shifts the resonator frequency and vice versa. This indicates that the photon number fluctuation in the resonator also fluctuates the qubit frequency and causes dephasing. When the qubit is biased at the flux sweet spot, this dephasing mechanism becomes important. The corresponding thermal photon shot noise has a Lorentzian spectrum and induces pure dephasing rate

$$\Gamma_\phi = \frac{n_{\mathrm{th}} \, \kappa \, \chi_{01}^2}{\kappa^2 + \chi_{01}^2} \tag{2.50}$$

in the small thermal photon number n_{th} limit [55]. Here, κ is the linewidth of the resonator, and χ_{01} is the resonator frequency shift conditioned on the qubit being at 0 or 1 state. $n_{\mathrm{th}} = \frac{1}{e^{\hbar\omega_r / k_B T_{\mathrm{eff}}} - 1}$ is the thermal photon number inside the resonator with frequency ω_r, while this relation can be used to estimate the effective resonator temperature T_{eff} in our lab, which is around 50 - 60 mK.

2.4.2.4 Coherent quantum phase slips

A phase slip corresponds to the 2π phase jump across a JJ, equivalent to fluxon tunneling. The phase slip rate of each chain JJ is much smaller than the small JJ in a fluxonium circuit, as the phase slip energy is given by

$$\epsilon_{\text{ps}} = \sqrt{\frac{16E_J E_C}{\pi}} \left(\frac{8E_J}{E_C}\right)^{1/4} e^{-\sqrt{\frac{8E_J}{E_C}}} \tag{2.51}$$

[43]. Coherent quantum phase slips (CQPS) refers to the spatially interfering quantum phase slips depending on the distribution of the electric charge along the JJ chain. Considering N JJs in the chain, the corresponding energy is described by

$$E_{\text{CQPS}} = \sum_{j=1}^{N} \epsilon_{\text{ps},j} e^{i2\pi n_{gs,j}}, \quad n_{gs,j} = \sum_{k=0}^{j-1} n_{g,k} \tag{2.52}$$

where $n_{g,k}$ is the offset charge on the kth junction. This term adds a perturbative correction of phase-slip Hamiltonian to the fluxonium Hamiltonian and induce a qubit frequency shift depending on the instantaneous value of E_{CQPS} [56]. Accordingly, the charge noise results in pure dephasing through this mechanism and the corresponding Ramsey decay rate of a Gaussian decay profile

$$\Gamma_{\phi}^{\text{CQPS}} = \pi\sqrt{N}\epsilon_{\text{ps}}|\mathcal{F}_{01}| \tag{2.53}$$

[57], where the structure factor $\mathcal{F}_{\alpha\beta} \approx \int_{-\infty}^{\infty} d\varphi\, \psi_\beta^*(\varphi)\psi_\beta(\varphi - 2\pi) - \int_{-\infty}^{\infty} d\varphi\, \psi_\alpha^*(\varphi)\psi_\alpha(\varphi - 2\pi)$ utilizes the wavefunction overlap after a 2π shift. In our samples, we design large $E_J^{\text{chain}}/E_C^{\text{chain}}$ to suppress this dephasing mechanism.

2.5 Coupled Fluxonium Qubits

Engineering robust on-demand interactions between long-lived quantum bits (qubits) is important for enabling high-fidelity logical gates in future quantum computers and achievable by the outstanding tunability of superconducting circuits. In the case of superconducting qubits [58, 59, 60], a common approach is to connect two frequency-detuned qubit circuits via a capacitor and activate the qubit-qubit interaction by microwave drives. A characteristic drawback of such a permanent connection is that it usually leads to a static ZZ-term, making one qubit frequency conditional on the state of another qubit. This arises from the generally uneven ”pressure” on the four computational levels from the higher-energy non-computational levels. This interaction would induce coherent errors during single-qubit operations and lead to quantum cross-talk across the qubit register, which is one of the main challenges to build a superconducting quantum processor. This effect can be pronounced not only for weakly-anharmonic transmons [20, 22, 23, 24, 25, 26] but also for strongly-anharmonic fluxoniums [31, 32, 36, 38]. The magnitude of the static ZZ-term can be suppressed by a variety of tricks, from introducing more complex coupler elements [26, 27, 29, 33, 34, 61, 62, 63, 64], including fast-flux-tunable couplers [65], to applying differential AC-stark shifts by off-resonantly driving the non-computational transitions [32]. However, both mitigation strategies increase the complexity of devices and control protocols. In this section, we discuss the scheme of direct coupling between qubits with fixed coupling strength and explore the possibility of strong qubit-qubit hybridization without introducing unwanted quantum crosstalks.

2.5.1 Transversly coupled spin-1/2 qubits

We first start with the simple case, characterizing a transversly coupled spin-1/2 pair with Hamiltonian

$$\hat{\mathcal{H}}/\hbar = -\frac{1}{2}\left(\omega_A\hat{\sigma}_z^A + \omega_B\hat{\sigma}_z^B\right) + J\hat{\sigma}_x^A\hat{\sigma}_x^B, \tag{2.54}$$

having the dressed eigenstates

$$\begin{aligned}
|00\rangle &= \cos\theta_1 \left|0_A\right\rangle \left|0_B\right\rangle - \sin\theta_1 \left|1_A\right\rangle \left|1_B\right\rangle, \\
|01\rangle &= \cos\theta_2 \left|0_A\right\rangle \left|1_B\right\rangle - \sin\theta_2 \left|1_A\right\rangle \left|0_B\right\rangle, \\
|10\rangle &= \cos\theta_2 \left|1_A\right\rangle \left|0_B\right\rangle + \sin\theta_2 \left|0_A\right\rangle \left|1_B\right\rangle, \\
|11\rangle &= \cos\theta_1 \left|1_A\right\rangle \left|1_B\right\rangle + \sin\theta_1 \left|0_A\right\rangle \left|0_B\right\rangle,
\end{aligned} \tag{2.55}$$

assuming adiabatic indexing of the coupled system. $|i_\alpha\rangle$ denotes the bare spin basis with $i = 0, 1$ and $\alpha = A, B$. The hybridization strength is determined by θ_1 and θ_2, satisfying

$$\begin{aligned}
\tan 2\theta_1 &= \frac{2J}{\omega_A + \omega_B}, \\
\tan 2\theta_2 &= \frac{2J}{\omega_A - \omega_B}.
\end{aligned} \tag{2.56}$$

The symmetry of Eq. 2.55 indicates symmetric transition matrix elements

$$\langle 01|\hat{\sigma}_x^B|00\rangle = \langle 11|\hat{\sigma}_x^B|10\rangle, \langle 10|\hat{\sigma}_x^A|00\rangle = \langle 11|\hat{\sigma}_x^A|01\rangle \tag{2.57}$$

and

$$\langle 01|\hat{\sigma}_x^A|00\rangle = -\langle 11|\hat{\sigma}_x^A|10\rangle, \langle 10|\hat{\sigma}_x^B|00\rangle = -\langle 11|\hat{\sigma}_x^B|01\rangle, \tag{2.58}$$

where the elements in Eq. 2.57 and Eq. 2.58 are called direct matrix elements and cross matrix elements, respectively. The symmetric eigenenergies leads to zero static ZZ

$$\Big(\langle 01|\hat{\mathcal{H}}|01\rangle - \langle 00|\hat{\mathcal{H}}|00\rangle\Big) - \Big(\langle 11|\hat{\mathcal{H}}|11\rangle - \langle 10|\hat{\mathcal{H}}|10\rangle\Big) = 0. \tag{2.59}$$

Eq. 2.55 simplifies to

$$\begin{aligned}
|00\rangle &\approx |0_A\rangle\,|0_B\rangle - \frac{J}{\omega_A+\omega_B}\,|1_A\rangle\,|1_B\rangle\,,\\
|01\rangle &\approx |0_A\rangle\,|1_B\rangle - \frac{J}{\omega_A-\omega_B}\,|1_A\rangle\,|0_B\rangle\,,\\
|10\rangle &\approx |1_A\rangle\,|0_B\rangle + \frac{J}{\omega_A-\omega_B}\,|0_A\rangle\,|1_B\rangle\,,\\
|11\rangle &\approx |1_A\rangle\,|1_B\rangle + \frac{J}{\omega_A+\omega_B}\,|0_A\rangle\,|0_B\rangle\,,
\end{aligned} \tag{2.60}$$

if $J \ll |\omega_A - \omega_B|, |\omega_A + \omega_B|$, and the hybridization strength is proportional to J in this limit.

2.5.2 Coupled multilevel artificial atoms

Superconducting qubits are typically multilevel artificial atoms, which complicates their coupling schemes. In the weak coupling limit, perturbation theory provides insight into the parameters that determine hybridization strength, as well as the resulting eigenenergy shifts and transition matrix elements. We can define the Hamiltonian $\hat{\mathcal{H}} = \hat{\mathcal{H}}_A + \hat{\mathcal{H}}_B + \hat{V}_{AB}$ and

$$V_{kl,k'l'} = \langle kl|\hat{V}_{AB}|k'l'\rangle = J_O\langle k_A|\hat{O}_A|k'_A\rangle\langle l_B|\hat{O}_B|l'_B\rangle \tag{2.61}$$

for the qubit-qubit coupling term $\hat{V}_{AB}$, where the operator $\hat{O}$ is $\hat{n}$ ($\hat{\varphi}$) if the qubits are capacitively (inductively) coupled with coupling strength J_O. The dressed computational states in terms of the bare qubit basis are

$$
\begin{aligned}
|00\rangle &\approx |0_A\rangle\,|0_B\rangle - \frac{V_{11,00}}{\omega_{01}^A + \omega_{01}^B}\,|1_A\rangle\,|1_B\rangle - \frac{V_{31,00}}{\omega_{03}^A + \omega_{01}^B}\,|3_A\rangle\,|1_B\rangle - \frac{V_{13,00}}{\omega_{01}^A + \omega_{03}^B}\,|1_A\rangle\,|3_B\rangle + \cdots\,, \\
|01\rangle &\approx |0_A\rangle\,|1_B\rangle - \frac{V_{10,01}}{\omega_{01}^A - \omega_{01}^B}\,|1_A\rangle\,|0_B\rangle - \frac{V_{12,01}}{\omega_{01}^A + \omega_{12}^B}\,|1_A\rangle\,|2_B\rangle - \frac{V_{30,01}}{\omega_{03}^A - \omega_{01}^B}\,|3_A\rangle\,|0_B\rangle + \cdots\,, \\
|10\rangle &\approx |1_A\rangle\,|0_B\rangle + \frac{V_{01,10}}{\omega_{01}^A - \omega_{01}^B}\,|0_A\rangle\,|1_B\rangle - \frac{V_{21,10}}{\omega_{12}^A + \omega_{01}^B}\,|2_A\rangle\,|1_B\rangle + \frac{V_{03,10}}{\omega_{01}^A - \omega_{03}^B}\,|0_A\rangle\,|3_B\rangle + \cdots\,, \\
|11\rangle &\approx |1_A\rangle\,|1_B\rangle + \frac{V_{00,11}}{\omega_{01}^A + \omega_{01}^B}\,|0_A\rangle\,|0_B\rangle - \frac{V_{20,11}}{\omega_{12}^A - \omega_{01}^B}\,|2_A\rangle\,|0_B\rangle + \frac{V_{02,11}}{\omega_{01}^A - \omega_{12}^B}\,|0_A\rangle\,|2_B\rangle + \cdots\,,
\end{aligned}
\tag{2.62}
$$

where we only keep the relevant terms with non zero $V_{kl,k'l'}$, considering states up to $|3\rangle$ and the corresponding transitions. These terms dominate because matrix elements to higher levels are smaller. This is why we focus on them when designing our qubit parameters. According to Eq. 2.62, a reasonable approach to achieving strong hybridization via higher energy levels is to bring the 0–1 transition frequency of one qubit close to the 1–2 transition frequency of the other. However, this method makes it difficult to avoid static ZZ interactions, as the energies of the states in Eq. 2.62 shift by different amounts at the same time when trying to increase the hybridization of one of the four states.

2.5.2.1 Capacitively coupled fluxonium qubits

The relatively large ZZ-term in capacitively coupled fluxoniums is related to a general property of transition matrix elements of the charge operator $\hat{n}$. That is, they are proportional to the transition frequency [66]. This is based on Eq. 2.15 along with the fact that the phase transition matrix elements at half flux quantum depend on the wavefunction distribution at phase space and do not generally change with frequency [34, 67]. For example, fluxonium qubit transition relies on the fluxon transition between the lowest two potential well, leading to $\langle 1|\hat{\varphi}|0\rangle \approx \pi$ independent of qubit parameters and thus frequency as shown in Fig. 2.5(a). Consequently, even if the non-computational transitions are far detuned from the computational ones, their effect cannot be readily neglected because of their relatively large transition frequency and matrix elements if qubits are capacitively coupled. This can be explained by the comparable coefficients $\frac{V_{20,11}}{\omega_{12}^A-\omega_{01}^B}$, $\frac{V_{02,11}}{\omega_{01}^A-\omega_{12}^B}$, and $\frac{V_{01,10}}{\omega_{01}^A-\omega_{01}^B}$ in Eq. 2.62, based on the values provided in Fig. 2.5(b) and (c).

2.5.2.2 Inductively coupled fluxonium qubits

Compared to capacitive coupling, the coupling of fluxoniums via a mutual inductance is governed by the phase operator $\hat{\varphi}$, and the transition matrix elements do not generally grow with frequency [34, 67]. Furthermore, the matrix element of computational transition $\langle 1|\hat{\varphi}|0\rangle$ is larger than other transitions involving higher levels as shown in Fig. 2.5(d) for example. Along with the strong anharmonicity, this leads to $\frac{V_{20,11}}{\omega_{12}^A-\omega_{01}^B}, \frac{V_{02,11}}{\omega_{01}^A-\omega_{12}^B} \ll \frac{V_{01,10}}{\omega_{01}^A-\omega_{01}^B}$ in Eq. 2.62, so it is possible to achieve strong qubit-qubit hybridization without involving higher levels and thus with low static ZZ as shown experimentally in Chapter 4. Combining inductive and capacitive coupling can even lead to completely canceling the static ZZ term [68].

2.6 Quantum gates

In this section, we introduce the principles behind implementing gate operations on superconducting qubits and briefly review the techniques used for various types of gates. We focus more on the method we adopt in the experiments, the microwave activated gates, instead of the flux gates tuning the external flux bias.

2.6.1 Single-qubit gates

2.6.1.1 X and Y gates: Rabi oscillation

Let's first introduce the simplest and the most common method to control qubits, which considers a semi-classical model of a qubit under a classical drive in the lab frame:

$$\hat{\mathcal{H}}^{\mathrm{lab}} = -\frac{\omega_q}{2}\hat{\sigma}_z + \frac{\Omega}{2}\cos(\omega_d t + \phi_d)\hat{\sigma}_x. \tag{2.63}$$

The drive strength Ω is proportional to the field amplitude at the qubit and the matrix element $\langle 1|\hat{O}|0\rangle$, where $\hat{O}$ represents either $\hat{n}$ or $\hat{\varphi}$ depending on whether the drive line is capacitively or inductively coupled to the qubit. ϕ_d denotes the phase of the drive. To remove the time dependence in the Hamiltonian, we move from the lab frame into the rotating frame by the rate of ω_d through the transformation

$$\hat{\mathcal{H}}^{\mathrm{rot}} = \hat{U}^{\dagger}\hat{\mathcal{H}}^{\mathrm{lab}}\hat{U} - i\hbar U^{\dagger}\frac{\partial \hat{U}}{\partial t} \tag{2.64}$$

with $\hat{U} = \exp(-i\frac{-\omega_d\hat{\sigma}_z}{2}t)$, which is also called the field interaction picture. We further apply rotating wave approximation (RWA) to drop the counter-rotating term oscillating with $e^{\pm i(\omega_d+\omega_q)t}$, which represents a fast precessing rotation axis by the rate of $\omega_d+\omega_q$ and averages out if the qubit dynamics is much slower, i.e., $|\delta|, \Omega \ll \omega_d + \omega_q$ with $\delta = \omega_d - \omega_q$. This term can also be viewed as a drive with a large detuning $\omega_d + \omega_q$, which barely changes the qubit population but only shifts the qubit frequency as we will discuss in the next section. There are also methods in the lab frame to completely cancel out this counter-rotating term [69]. Now we reach the time independent Hamiltonian in the rotating frame

$$\hat{\mathcal{H}}^{\mathrm{rot}} = \frac{\delta}{2}\hat{\sigma}_z + \frac{\Omega}{2}\cos\phi_d\hat{\sigma}_x - \frac{\Omega}{2}\sin\phi_d\hat{\sigma}_y, \tag{2.65}$$

giving the equation of motion

$$\frac{d\vec{S}}{dt} = \vec{\widetilde{\Omega}} \times \vec{S} \tag{2.66}$$

with the Bloch vector $\vec{S} = (\langle\hat{\sigma}_x\rangle, \langle\hat{\sigma}_y\rangle, \langle\hat{\sigma}_z\rangle)$ and $\vec{\widetilde{\Omega}} = (\Omega\cos\phi_d, \Omega\sin\phi_d, \delta)$. This dynamic represents a rotation of the Bloch vector $\vec{S}$ with respect to the axis $\frac{\vec{\widetilde{\Omega}}}{\left|\vec{\widetilde{\Omega}}\right|}$ by the rate of $\left|\vec{\widetilde{\Omega}}\right| = \widetilde{\Omega}$. This rotation makes qubit population oscillate, which is called the Rabi oscillation with Ω defined as the Rabi frequency and $\widetilde{\Omega} = \sqrt{\delta^2 + \Omega^2}$ defined as the generalized Rabi frequency. When the drive is on resonance with qubit, i.e. $\delta = 0$, we can achieve X and Y gate by setting $\phi_d = 0$ and $\pi/2$, respectively. Note that the phase offset of ϕ_d due to cables, microwave components, and incommensurate period of pulse sequences is not important, as we can always redefine the frame to set this phase offset zero for the X rotation axis.

2.6.1.2 Z gates: virtual and geometric phase accumulation

To achieve a Z rotation of the Bloch vector, a straightforward way is shifting the qubit frequency for a certain amount of time without drive to accumulate dynamic phase as shown in Eq. 2.65 with $\Omega = 0$. This can be done by applying a flux pulse changing the biased external flux, but this way moves the qubit away from the flux sweet spot and introduces more incoherent errors. In practice, we apply the virtual Z gate [70] which simply rotates and updates the reference frame in software at no additional cost in reality. This method performs the best in our experiments, as it has no physical pulse and thus zero time cost. Each virtual Z rotation by an angle θ_z in the pulse sequence shifts the phase ϕ_d needed for subsequent X and Y pulses by θ_z, equivalent to rotating the observer's frame rather than the qubit state.

There are also other ways to perform Z gates using only microwave drives. While these approaches may not outperform virtual Z gates, they offer valuable insight into qubit dynamics and can be extended to facilitate two-qubit gates mentioned in Section 2.6.2. Furthermore, the following discussions including those in the next section are helpful to understand our gate calibration and error budget in Chapter 4. In the qubit frame, where we set the drive frequency for X and Y gates $\omega_d^{X,Y} = \omega_q$ to define this frame as reference, we can apply an off resonant drive with frequency ω_d^Z to perform a Z gate. The qubit dynamics in the off-resonance frame determined by ω_d^Z follows Eq. 2.66, and a full 2π rotation needs time $t_{2\pi} = 2\pi/\widetilde{\Omega}$. The evolution operator of this one cycle is $\exp\left(\text{sign}(\delta) i \frac{2\pi}{2} \hat{\sigma}_z\right)$, which is equivalent to a identity matrix with an overall phase of -1 and does not depend on Ω, ϕ_d, $|\delta|$. We can now transform the evolution operator from the off-resonance frame back to the reference frame, which is the on-resonance qubit frame, as $\exp(-i\frac{\delta(t+t_{2\pi})}{2}\hat{\sigma}_z)\exp\left(\text{sign}(\delta) i \frac{2\pi}{2} \hat{\sigma}_z\right)\exp(i\frac{\delta t}{2}\hat{\sigma}_z) = \exp(-i\frac{\delta t_{2\pi} - \text{sign}(\delta)2\pi}{2}\hat{\sigma}_z)$. The accumulated geometric phase $\theta_z = \delta t_{2\pi} - \text{sign}(\delta)2\pi = 2\pi(\frac{|\delta|}{\widetilde{\Omega}} - 1)\text{sign}(\delta)$ has magnitude being the solid angle of the off-resonant trajectory, which depends only on the geometric interpretation not on how fast it rotates. For example, the phase accumulated is still the same if both Ω and δ are increased by the same ratio to speed up the cycle, since the same Ω/δ ratio leads to identical trajectories. An arbitrarily small θ_z can be achieved by relatively large detuning $|\delta| \gg \Omega$.

2.6.1.3 Stark shift and adiabaticity

The microwave activated Z gate above has an average phase accumulation rate of

$$\overline{\omega_Z} = \frac{\theta_z}{t_{2\pi}} = (|\delta| - \widetilde{\Omega})\text{sign}(\delta) = \left(|\delta| - \sqrt{\delta^2 + \Omega^2}\right)\text{sign}(\delta). \tag{2.67}$$

Comparing the eigenenergy difference of

$$\hat{\mathcal{H}} = \frac{\delta}{2}\hat{\sigma}_z + \frac{\Omega}{2}\hat{\sigma}_x \tag{2.68}$$

with the case of no drive $\hat{\mathcal{H}} = \frac{\delta}{2}\hat{\sigma}_z$, we can see the deviation is exactly Eq. 2.67, which is called ac Stark shift. Here, we set $\phi_d = 0$ in Eq. 2.65 to get Eq. 2.68 for clearer illustration without losing generality. In the limit of $|\delta| \gg \Omega$, we can perform Z gates with arbitrary angle by repeating multiple off-resonant 2π rotations. In fact, the component of X rotation is small and barely changes qubit population. Thus, we do not need to wait for a full 2π cycle to perform the Z gate, which can be simply done by waiting an arbitrary gate time t_g to accumulate arbitrary phase $\left(|\delta| - \sqrt{\delta^2 + \Omega^2}\right)\text{sign}(\delta)t_g$. This changes the picture from geometric phase accumulation to dynamic phase accumulation by the rate of qubit frequency shift.

To further extend this method to the case $|\delta| \sim \Omega$, we need to apply a adiabatic pulse shape. An adiabatic process indicates the change of Hamiltonian is slow enough so that the eigenbasis follows the evolution of the instantaneous dressed eigenstates, and the population distribution of a quantum state over these dressed eigenstates is always the same at different time. This means the coefficient of each eigenstate keeps the same magnitude but introduces only a phase factor.

Taking a adiabatic flux pulse for dynamic phase accumulation for example, the Hamiltonian can be described by

$$\hat{\mathcal{H}} = \frac{\delta(t)}{2}\hat{\sigma}_z + \frac{\Omega}{2}\hat{\sigma}_x \tag{2.69}$$

because qubit frequency depends on flux. We note that there's no microwave drive in this flux gate scheme, and the Ω in Eq. 2.69 does not mean the Rabi frequency defined in the scheme of microwave activated gates but indicates the minimal qubit frequency at the flux sweet spot. We keep the same symbol simply for clearer analogy between the two scenarios. The unwanted population transfer that does not adiabatically follow the dressed states is

$$P_{\text{lost}} = \exp\left(-\frac{\pi\Omega^2}{2|\partial_t\delta(t)|}\right), \tag{2.70}$$

the so-called Landau–Zener tunnel probability [71]. Eq. 2.70 manifests the adiabatic condition $|\partial_t\delta(t)| \ll \Omega^2$. Similarly, the adiabatic condition for the scheme of microwave activated gates is

$$|\partial_t\Omega(t)| \ll \delta^2, \tag{2.71}$$

where the time dependence of $\Omega(t)$ describes the slow varying pulse envelope. We can now see that as long as Eq. 2.71 is fulfilled, the final qubit state after the pulse is simply the initial state accompanied by an additional dynamic phase. This phase is accumulated by the rate of the instantaneous ac Stark shift $|\delta| - \sqrt{\delta^2 + \Omega(t)^2}$ without inducing qubit population transfer even when $\Omega \sim |\delta|$. This can also be explained in the frequency domain: Longer and smoother pulse shape has a Fourier frequency spectrum centered at ω_d with a smaller linewidth, leading to a smaller component at the qubit frequency ω_q, which is δ away from the center. Weaker pulse amplitude further lower this component and thus minimize the qubit population transfer. The next question is which parameter regime gives better Z gates, $|\delta| \sim \Omega$ or $|\delta| \gg \Omega$? Unfortunately, when $|\delta| \sim \Omega$, the adiabatic condition requires long gate time t_g and results in large accumulated phase θ_z, which is not practical for the goal of fast Z gates with arbitrary target phase. Taking a pulse with cosine envelope and peak amplitude Ω_{max} for example, the adiabatic condition $|\partial_t\Omega(t)| \sim \Omega_{\text{max}}/t_g \ll \delta^2$ leads to $t_g \gg 1/\delta$ along with the accumulated phase $\left(|\delta| - \sqrt{\delta^2 + {\Omega_{\text{max}}}^2}\right) t_g \sim \delta t_g \gg 1$ if $|\delta| \sim \Omega_{\text{max}}$.

Nonetheless, it is still important to understand the adiabaticity of pulses with $|\delta| \gg \Omega$ to minimize population transfer and its related errors while chasing fast and short gates. For example, in the regime where $|\delta| \gg \Omega$, larger δ is still better because it allows smaller unwanted population change assuming the same ramping time t_g and same phase accumulation rate after reaching Ω_{max}. This rate is $\omega_0 = \sqrt{\delta^2 + {\Omega_{\text{max}}}^2} - |\delta| \approx \frac{{\Omega_{\text{max}}}^2}{2|\delta|}$. The gate error due to unwanted population transfer analogous to Eq. 2.70 is smaller if $\frac{\delta^2}{|\partial_t\Omega(t)|} \sim \frac{\delta^2}{\Omega_{\text{max}}/t_g} = \frac{\delta^2 t_g}{\sqrt{2\omega_0|\delta|}}$ is larger, which is satisfied when $|\delta|$ is larger. Further pulse shaping techniques such as Derivative Removal by Adiabatic Gate (DRAG) [72, 73] that modifies the Fourier spectrum of pulse and reduces the frequency component at qubit transition can further suppress residual population transfer. This enables faster gates while maintaining adiabaticity.

In addition to the Stark shift based Z gate discussed above, another common situation is the off resonant drive on 1-2 transition while performing X gates on 0-1 transition and requires the same analysis to suppress unwanted leakage to the 2 state. Fluxonium has strong anharmonicity and is relatively resilient to this leakage error. However, for fluxonium qubits with much lower frequency, the huge ratio of $\langle 2|\hat{n}|1\rangle / \langle 1|\hat{n}|0\rangle$ can be a problem while trying to achieve fast single-qubit X gates through charge drive. The Rabi frequency Ω_{1-2} for 1-2 transition starts to get close to detuning, i.e., the anharmonicity, inducing off resonant excitation. To mitigate this effect, flux drive with small $\langle 2|\hat{\varphi}|1\rangle/\langle 1|\hat{\varphi}|0\rangle$ ratio is an alternative approach [69]. However, RWA is not applicable for low frequency qubits such as a heavy fluxonium. Other methods dealing with counter-rotating errors [69] or resorting to flux diabatic gates [13] similar to the idea of Eq. 2.70 are the solutions.

2.6.2 Two-qubit gates

Two-qubit gates are entangling gates having the power to evolve the composite single-qubit states on two qubits into entangled states that are not separable. There are three common two-qubit gates in superconducting qubits:

$$\text{CNOT} = \begin{bmatrix} 1 & 0 & 0 & 0 \\ 0 & 1 & 0 & 0 \\ 0 & 0 & 0 & 1 \\ 0 & 0 & 1 & 0 \end{bmatrix}, \quad \text{iSWAP} = \begin{bmatrix} 1 & 0 & 0 & 0 \\ 0 & 0 & -i & 0 \\ 0 & -i & 0 & 0 \\ 0 & 0 & 0 & 1 \end{bmatrix}, \quad \text{CZ} = \begin{bmatrix} 1 & 0 & 0 & 0 \\ 0 & 1 & 0 & 0 \\ 0 & 0 & 1 & 0 \\ 0 & 0 & 0 & -1 \end{bmatrix}, \tag{2.72}$$

presented on the basis of $|00\rangle, |10\rangle, |01\rangle, |11\rangle$. All the three types of gates have been demonstrated on fluxonium qubits [3, 31, 32, 33, 34, 38]. CNOT represents a controlled rotation of one qubit conditional on the state of the other one, which is commonly implemented based on cross-resonance scheme [3, 38]. iSWAP swaps the qubit excitation with an additional phase i, which is important to entangle qubits because SWAP gate is not an entangling gate. Parametric drive at the frequency difference of the two qubits [34] enables iSWAP. CZ appends a selective phase on $|11\rangle$ state, which can be accumulated through geometric phase [31, 33] and through dynamic phase based on differential AC Stark Shifts [32]. We note that each two-qubit gate can be generated by another one with additional single-qubit gates. Accordingly, one multi qubit design typically performs only one type of two-qubit gate that fits the system best and has the lowest error. In this thesis, we focus on the cross-resonance gates characterized in Chapter 4.

Chapter 3: Integer Fluxonium Qubit

3.1 Integer Fluxonium Properties

To suppress qubits' sensitivity to the dominant dielectric loss, typical fluxonium lowers the qubit frequency ω_{01} to achieve smaller charge matrix element $\langle 1|\hat{n}|0\rangle$ following Eq. 2.32. From Eq. 2.15, we can see that suppressing the phase matrix element $\langle 1|\hat{\varphi}|0\rangle$ rather than ω_{01} can also lead to small $\langle 1|\hat{n}|0\rangle$ and thus resilience to dielectric loss. In addition to engineering the parity of wavefunction to reduce $\langle 1|\hat{\varphi}|0\rangle$, another direct way is simply localizing the wavefunction of $|0\rangle$ and $|1\rangle$ without overlapping each other. In fact, the disjointness of wavefunction suppresses not only dielectric loss but also other relaxation channels coupled through any form of phase operator φ. This can be achieved by changing the external flux bias off sweet spot [9], which unavoidably leads to stronger pure dephasing and lower T_2. Accordingly, the goal is to achieve disjoint eigenstates at the sweet spot similar to the idea of $0-\pi$ qubits [74], enabled by increasing the degrees of freedom to 2D potential well. In this chapter, we aim to achieve this goal by biasing the fluxonium at zero flux quantum, forming the so-called integer fluxonium qubit (IFQ), which still operates with a single degree of freedom. Zero magnetic field eliminates the need for a large current bias, thereby easing constraints related to the limited cooling power of a dilution fridge. The similar frequency range of IFQ to transmon indicates IFQ can fit the well-developed measurement design and setup for the widely adopted transmon.

3.1.1 Design of qubit parameters

The parameter regime for integer fluxonium is motivated by the following considerations. First, it is crucial that $E_J \gg E_L$, ensuring that the potential energy landscape exhibits multiple potential wells with local minima as shown in Fig 3.1(a). Second, $E_J \gg E_C$ to ensure the kinetic energy is small, making the wavefunctions localized in the wells similar to a slow particle trapped in these potential dips. Third, $\sqrt{8E_J E_C} \gg 2\pi^2 E_L$ to detune the two types of excitations: transitions in a single well (plasmon) and tunneling between different wells (fluxon). The plasmon transition represents the oscillation in one well, so the transition energy can be approximated as $\sqrt{8E_J E_C}$. This needs to be far-detuned from our qubit frequency, the fluxon transition frequency, which is given by the energy difference between the local minima of potential wells $\hbar\omega_{01} \approx 2\pi^2 E_L$. The frequency of a readout resonator can lie near the plasmon transition frequency to enable a dispersive shift for the qubit transition, similar to a typical fluxonium biased at half flux quantum.

3.1.2 Hamiltonian in fluxon basis

Even though the spectral properties of integer fluxonium can be numerically computed using the Hamiltonian in Eq. 2.10 as shown in Fig. 3.1(b) and (c), it is insightful to consider an effective model based solely on flux quantization and tunneling processes [43, 75] to achieve analytical expressions for some important features. This model is a good fit because IFQ's parameters are in the relatively deep phase-slip regime as discussed in the previous section. We first consider the basis of fluxon states $|m\rangle$, which represent a particle localized at the bottom of the mth Josephson potential well, as indexed in Fig. 3.1(a). We then introduce the phenomenological

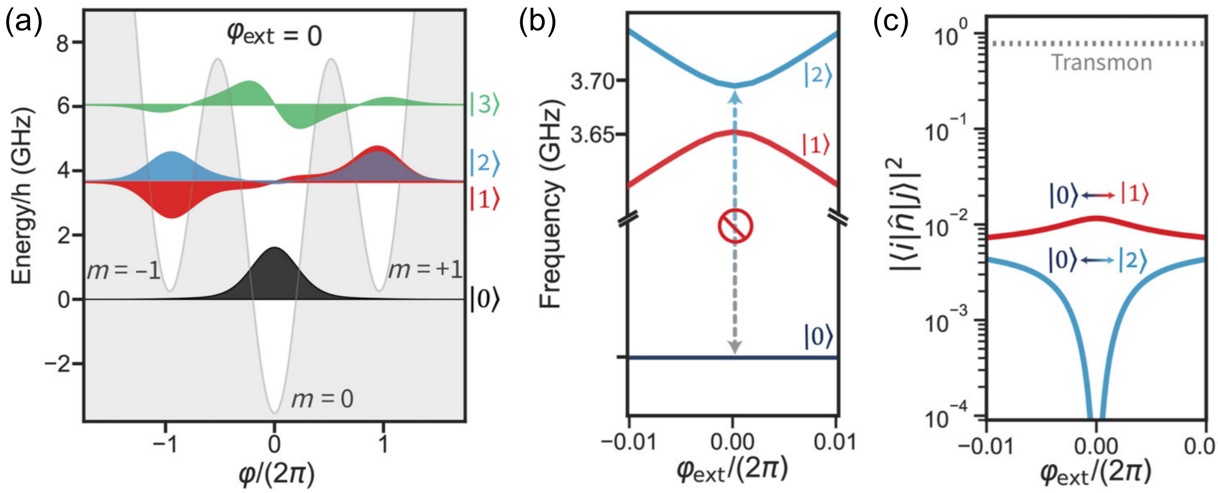

Figure 3.1: The wavefunctions, energy spectrum, and matrix elements of the lowest four eigenstates with E_J = 5 GHz, E_L = 0.2 GHz, and E_C = 1.5 GHz. (a) The wavefunctions and eigenenergies biased at zero flux quantum ($\varphi_{\mathrm{ext}} = 0$) along with the corresponding potential landscape. The qubit transition is $|0\rangle - |1\rangle$. (b),(c) The energy spectrum, charge matrix elements across different external flux bias near the sweet spot, respectively. At $\varphi_{\mathrm{ext}} = 0$, 0-2 matrix element is zero due to the even parity as shown in (a) and thus transition forbidden. The charge matrix element of a conventional transmon is also plotted for comparison, showing the lower sensitivity to dielectric loss of IFQ despite that the qubit frequencies are similar.

tunneling (phase slip) energy ϵ_1 and ϵ_2, corresponding to transitions that change m by ± 1 and ± 2, respectively. The two energies represents single- and double-fluxon tunneling processes , corresponding to 2π and 4π phase slip in the φ space, respectively. The effective Hamiltonian is thus given by

$$\hat{\mathcal{H}}_{\text{eff}} = \sum_m \frac{E_L^\Sigma}{2} \left(2\pi m - \varphi_{\text{ext}}\right)^2 |m\rangle\langle m| - \frac{\epsilon_1}{2}(|m\rangle\langle m+1| + |m+1\rangle\langle m|) + \frac{\epsilon_2}{2}(|m\rangle\langle m+2| + |m+2\rangle\langle m|), \tag{3.1}$$

where $E_L^\Sigma = \left(E_L^{-1} + E_J^{-1}\right)^{-1}$ is the total linearized loop inductance. $\epsilon_1 \gg \epsilon_2$, and the values of ϵ_1 and ϵ_2 are both exponentially suppressed by the ratio E_J/E_C [16], as Eq. 2.51 is valid in the limit $E_J/E_C \gg 1$ for example. At $\varphi_{\text{ext}} = 0$, we can calculate the eigenenergies of the lowest three states by diagonalizing the Hamiltonian Eq. 3.1 truncated to the subspace spanned by the relevant three fluxon states $|m = -1\rangle$, $|m = 0\rangle$, and $|m = 1\rangle$. Assuming $4\pi^2 E_L^\Sigma \gg \epsilon_1 \gg \epsilon_2$, the three eigenstates are

$$\begin{aligned} |0\rangle &\approx |m = 0\rangle + \alpha(|m = -1\rangle + |m = +1\rangle), \\ |1\rangle &\approx \frac{1}{\sqrt{2}}(|m = -1\rangle - |m = +1\rangle), \\ |2\rangle &\approx \frac{1}{\sqrt{2}}(|m = -1\rangle + |m = +1\rangle) - \sqrt{2}\alpha|m = 0\rangle, \end{aligned} \tag{3.2}$$

where $\alpha = \epsilon_1/4\pi^2 E_L^\Sigma$ is a small number. Accordingly,

$$\begin{aligned} \hbar\omega_{01} &= 2\pi^2 E_L^\Sigma + \alpha\epsilon_1 - \epsilon_2/2 \approx 2\pi^2 E_L^\Sigma, \\ \hbar\omega_{12} &= \alpha\epsilon_1 + \epsilon_2. \end{aligned} \tag{3.3}$$

We note that $\hat{\varphi} = 2\pi\hat{m}$, giving $\langle 0|\hat{\varphi}|2\rangle = 0$ and $\langle 0|\hat{\varphi}|1\rangle \approx 2\sqrt{2}\pi\alpha \ll 1$, aligned with our goal of disjoint computational states. We can next apply Eq. 2.15 to get

$$\langle 0|\hat{n}|1\rangle_{\varphi_{\text{ext}}=0} \approx \frac{\sqrt{2\pi}}{8}\frac{\epsilon_1}{E_C} \approx \sqrt{2}\langle 0|\hat{n}|1\rangle_{\varphi_{\text{ext}}=\pi}, \tag{3.4}$$

where the $\langle 0|\hat{n}|1\rangle$ of a conventional fluxonium biased at $\varphi_{\text{ext}} = 0.5$ is from the same derivation giving $\hbar\omega_{01} = \epsilon_1$ and $\langle 0|\hat{\varphi}|1\rangle \approx \pi$. We can see IFQ's sensitivity to dielectric loss is comparable to a typical fluxonium at $\varphi_{\text{ext}} = 0.5$, which is also shown in Fig. 2.5(c) and Fig. 3.1(c), but has much higher qubit frequency comparable to transmon. We note that the charge matrix element for transmon can be approximated as $\sqrt[4]{E_J/8E_C} \simeq 1$, which is plotted in Fig. 3.1(c) for comparison.

3.1.3 Leakage to state $|2\rangle$ and $|3\rangle$

Since the qubit frequency of IFQ is much higher than a typical fluxonium $\varphi_{\text{ext}} = 0.5$ and thus closer to the frequency of $|0\rangle - |3\rangle$ as shown in Fig. 3.1(a), it is more likely to cause off resonant leakage to $|3\rangle$ while driving $|0\rangle - |1\rangle$ as $\langle 0|\hat{n}|3\rangle$ is relatively large. Another possible channel is the leakage to $|2\rangle$. At $\varphi_{\text{ext}} = 0$, $\langle 0|\hat{n}|2\rangle$ is zero, and $\langle 1|\hat{n}|2\rangle$ is small because of small ω_{12}. Along with the large detuning $\omega_{01} - \omega_{12}$, the $|0\rangle - |1\rangle$ transition can safely serve as a qubit without leakage to $|2\rangle$. However, in reality, there is always a small deviation $\delta\varphi_{\text{ext}}$ off from $\varphi_{\text{ext}} = 0$, either due to instrument imprecision or flux noise such as the low frequency $1/f$ noise. As a result, the qubit drive acquires a small coupling to state $|0\rangle - |2\rangle$ proportional to the value of $\left(\frac{\partial\langle 0|\hat{n}|2\rangle}{\partial\varphi_{\text{ext}}}\right)\delta\varphi_{\text{ext}}$ near $\varphi_{\text{ext}} = 0$, which is not negligent because of the small detuning $\omega_{02} - \omega_{01} = \omega_{12}$. In addition, the more the integer fluxonium is protected from dielectric loss, the smaller the ϵ_1 becomes, and thus the smaller the ω_{12} is. We will investigate the effect of these leakage channels on gate operations in Section 3.3.

3.2 Spectrum and Coherence Measurements

The design of our IFQ device is shown in Fig. 3.2(a), capacitively coupled to the resonant mode of a 3D cavity for readout. The fabrication and measurement setups are similar to those in [11]. Figure 3.2(b) shows the spectrum near $\varphi_{\text{ext}} = 0$ of our IFQ device with qubit parameters provided in Table 3.1. The $|0\rangle - |3\rangle$ transition frequency is far detuned at 6.86 GHz. The $|\langle 0|\hat{n}|1\rangle|$ of this IFQ is around 0.056, which is similar to a typical fluxonium at $\varphi_{\text{ext}} = 0.5$ and is more than one order of magnitude below the typical transmon value.

Fitted Parameters	E_C/h (GHz)	E_L/h (GHz)	E_J/h (GHz)	E_L^{Σ}/h (GHz)	ϵ_1/h (GHz)	ϵ_2/h (GHz)	Measured Parameters	$\omega_{01}/2\pi$ (GHz)	$\omega_{12}/2\pi$ (GHz)
	1.47	0.22	6.78	0.206	0.091	0.009		4.14	0.011

Table 3.1: Qubit parameters of the IFQ device.

Coherence Times	$\overline{T_1}$ (μs)	$\overline{T_2^*}$ (μs)	$\overline{T_2^E}$ (μs)	Inferred Parameters	$\tan\delta_C$	$S_{\Phi_{\text{ext}}}^{1/f}$ (Φ_0)	T_{eff} (mK)
	255	118	185		1×10^{-5}	8.8×10^{-6}	50

Table 3.2: Coherence parameters of the IFQ device.

Table 3.2 summarizes the measured coherence times averaged over individual fits of repetitive interleaved measurements across many hours. For T_1, the extracted effective dielectric loss tangent $\tan\delta_C$ from Eq. 2.32 is close to 10^{-5}, which is not small and illustrates the effectiveness of dielectric loss protection in integer fluxonium qubits. Since our experiment cannot rule out other energy relaxation mechanisms, this value should be interpreted as an upper bound. This

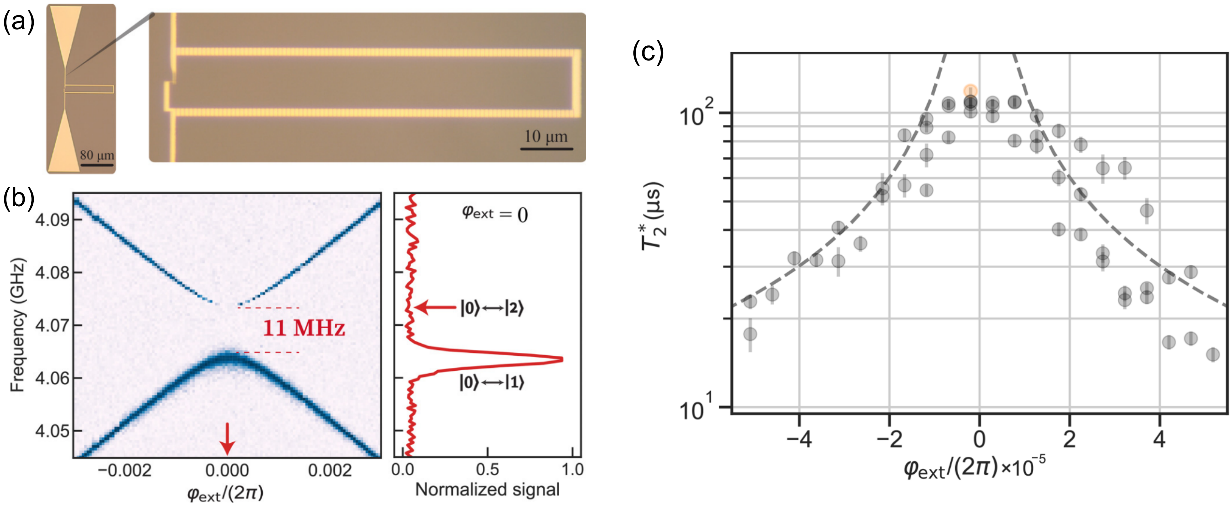

Figure 3.2: (a) An optical device photo of an integer fluxonium device. (b) The two-tone spectroscopy as a function of the excitation frequency and the flux bias near $\varphi_{\text{ext}} = 0$. The red signal trace shows the cross section at $\varphi_{\text{ext}} = 0$, indicating the absence of the forbidden $|0\rangle - |2\rangle$ transition signal. (c) The measured Ramsey coherence time T_2^* near $\varphi_{\text{ext}} = 0$. The dashed line is the first-order theoretical value due to $1/f$ flux noise, estimated using $1/T_2^* = (\frac{\partial\omega_{01}}{\partial\Phi_{\text{ext}}})S^{1/f}_{\Phi_{\text{ext}}}$ with $S^{1/f}_{\Phi_{\text{ext}}} = 8.8 \times 10^{-6}\Phi_0$.

relatively high estimate is not surprising, as our fabrication process does not employ advanced techniques for suppressing surface loss. Even though the detuning between qubit and the readout resonator at 7.46 GHz is smaller compared to a typical fluxonium, the estimated Purcell decay based on our device parameters using Eq. 2.35 corresponds to $T_1 > 10$ ms. For T_2, the deviation between T_2^* and T_2^E suggests the presence of low-frequency flux noise in the system. To investigate the $1/f$ flux noise, we measure T_2^* slightly away from the sweet spot as shown in Fig. 3.2(c), consistent with the first order flux noise channel with $S^{1/f}_{\Phi_{\text{ext}}} = 8.8 \times 10^{-6}\Phi_0$. This estimate is about a factor of 3 higher than the value usually found in fluxonium devices obtained using T_2^E rather than the more conservative T_2^* data as discussed in Eq. 2.46 and 2.47. We can further estimate the T_2 limit due to second order $1/f$ flux noise at the sweet spot following

$\Gamma_\phi^{(2)} \approx \frac{\partial^2\omega_{01}}{\partial\Phi_{\text{ext}}{}^2}(S_{\Phi_{\text{ext}}}^{1/f})^2 = \frac{\partial^2\omega_{01}}{\partial\varphi_{\text{ext}}{}^2}(S_{\Phi_{\text{ext}}}^{1/f})^2/{\phi_0}^2$. The second order flux sensitivity is

$$\frac{\partial^2\omega_{01}}{\partial{\varphi_{\text{ext}}}^2} \approx 8\pi^2\frac{{E_L}^2}{\hbar\omega_{12}} \tag{3.5}$$

derived from the second order perturbation theory by introducing $\delta\varphi_{\text{ext}}$ into Eq. 3.1 as perturbation near $\varphi_{\text{ext}} = 0$. The corresponding second order T_2 limit is longer than 10 ms despite of the more conservative $S_{\Phi_{\text{ext}}}^{1/f}$ value. The T_2^E at the sweet spot can be explained by thermal photon dephasing following Eq. 2.50 with the effective temperature of readout cavity $T_{\text{eff}} \approx 50$ mK, which agrees with the typical value found in the experiments with well-filtered measurement lines. This estimation is based on the measured cavity linewidth $\kappa/2\pi = 15$ MHz and dispersive shift $\chi_{01}/2\pi = 14.3$ MHz. All the inferred parameters for the decoherence channels discussed above are also provided in Table 3.2.

3.3 Gate Operations

In this section, we demonstrate the potential usefulness of IFQ by benchmarking the single-qubit Clifford gates.

3.3.1 Gate calibration

The qubit pulses are constant flat plateau pulses with Gaussian edges, with a 5-ns ramping time. We first determine the rough pulse parameters such as drive amplitude and frequency for a target pulse length by Rabi and Ramsey measurements, respectively, as discussed in 2. We next perform a multi-parameter optimization of fixed-length randomized benchmarking (RB) sequence fidelity, a method known as Optimized Randomized Benchmarking for Immediate Tune-up (ORBIT), with the Nelder–Mead algorithm. The concept of RB is discussed in Appendix A.4. This procedure fine-tunes all adjustable pulse parameters except for the pulse length.

3.3.2 Gate characterization and error budget

We characterize the averaged single-qubit gate fidelity using RB, with the details of this method provided in Appendix A.4. The highest averaged gate fidelity measured was $F = 0.9993(1)$, realized with a total π-pulse time of t_π = 88 ns as shown in Fig. 3.3(a). Note that the very small discrepancy of the fitted data from the exponential decay function can be due to fluctuations of the fidelity value in time during repetitive RB measurements.

For error budget, we investigate the gate errors for different gate times t_π. Our theory model includes three types of leading coherent errors shown in Fig. 3.3(b) in addition to incoherent errors. For the coherent errors, we simulate the time evolution operator of the driven system using the QuTiP package [76, 77] and estimate the gate fidelity

$$\mathcal{F} = \frac{\mathrm{Tr}(U^\dagger_{\mathrm{comp}} U_{\mathrm{comp}}) + \left|\mathrm{Tr}(U^\dagger_{\mathrm{comp}} U_{\mathrm{ideal}})\right|^2}{6} \tag{3.6}$$

[78], where U_{comp} is the evolution operator projected to the computational subspace. Different types of coherent errors can be estimated based on the corresponding matrix elements of the evolution operator. The first coherent error channel is the leakage to state $|3\rangle$, which is negligible in a reasonable range of t_π because of the large enough detuning $\omega_{03} - \omega_{01}$. A more possible scenario for errors is the occurrence of a small flux offset $\delta\Phi_{\mathrm{ext}}$ away from $\Phi_{\mathrm{ext}} = 0$. Such offsets can lead to three types of errors. (i) The $\langle 0|\hat{n}|2\rangle \propto \delta\varphi_{\mathrm{ext}}$ is small but non zero, and hence a sufficiently strong qubit drive would introduce leakage to state $|2\rangle$. (ii) If the low frequency flux

offset happens after the gate pulse was calibrated at $\phi_{\text{ext}} = 0$, the qubit frequency would shift by $\delta\omega_{01}$ and hence the qubit rotation would be off from the big circle trajectory of Bloch sphere and over rotate with slightly larger angle. Consequently, there is a coherent "detuning" error, on the order of $(\delta\omega_{01}/2\pi)^2 {t_\pi}^2$, for the gate time t_π. (iii) Finally, a flux offset increases the sensitivity of the qubit frequency to the $1/f$ flux noise and hence reduces the coherence time off sweet spot $T_2^*(\delta\varphi_{\text{ext}})$ as shown in Fig. 3.2(c). Consequently, we obtain a higher average incoherent error. For simplicity, this error is estimated for gate errors as $(t_\pi/T_2^*(\varphi_{\text{ext}}))/3$ in the limit $2T_1 \ll T_2^*$ [79, 80]. Fig. 3.3(b) shows an example of coherent errors with $\delta\Phi_{\text{ext}}/\Phi_0 = 3 \times 10^{-5}$. We find that the detuning error is negligible, while the state $|2\rangle$ leakage is suppressed to the 10^{-4} range. However, at such a flux offset, the coherence time already drops to about 40 μs, making incoherent error the dominant gate error. We compare the measured gate fidelity with the numerical estimates in Fig. 3.3(c), using five different flux offset values and summing up the three possible errors. It appears that the data can be explained almost entirely by the incoherent error in the presence of a flux offset that varies on a long time scale in the range $\delta\Phi_{\text{ext}}/\Phi_0 = (1-5) \times 10^{-5}$. It is worth noticing that our decomposition of single-qubit Clifford gates includes $\pi/2$ rotations and virtual Z gates, meaning that the measured gate errors may correspond to larger $\delta\Phi_{\text{ext}}$. We have noted the development of similar-size offsets during long-time spectroscopy measurements. In general, such flux offsets are not uncommon in fluxonium and they are usually mitigated by a more thorough magnetic shielding. Interestingly, for a flux offset $\delta\Phi_{\text{ext}}/\Phi_0 < 1 \times 10^{-5}$, the leakage to state $|2\rangle$ is negligible, in theory, even for relatively fast pulses ($t_\pi \approx 25$ ns). The ultimate flux stability of integer fluxonium devices as well as the limitations on the lowest practical gate time will be investigated in future works. In addition, we do not consider the effect of the finite device temperature causing leakage to $|2\rangle$ and additional dephasing of computational

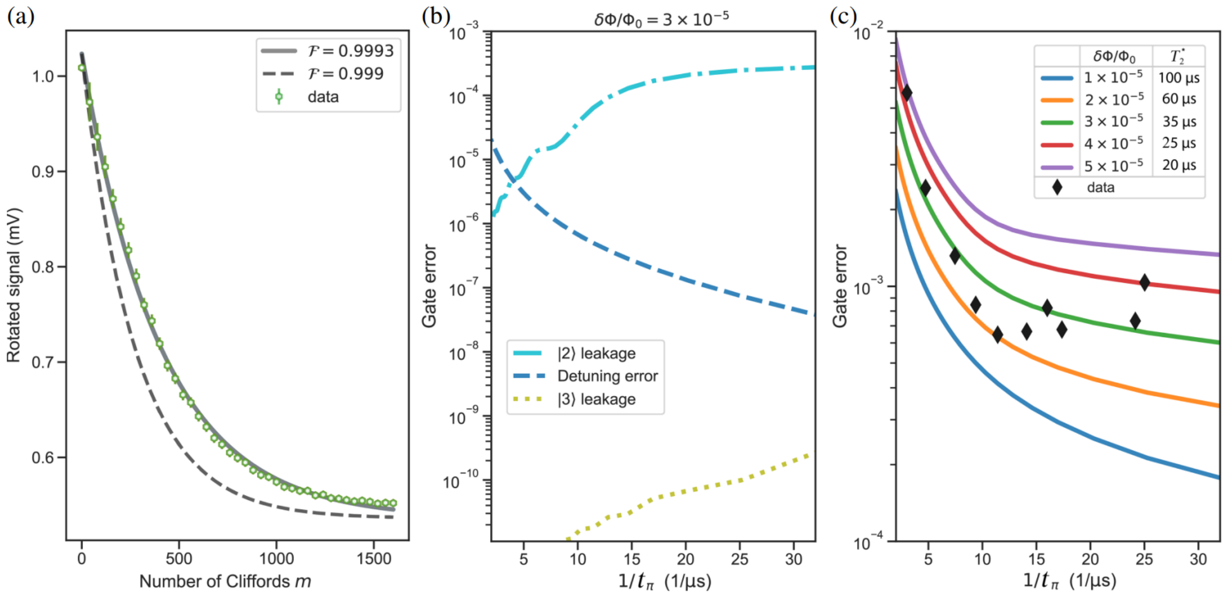

Figure 3.3: Single-qubit gate characterization of our IFQ. (a) The randomized benchmarking (RB) trace for the highest fidelity $F = 0.9993$, measured with a π-pulse time $t_\pi = 88$ ns. The reference dashed line corresponds to a fidelity $F = 0.999$, using the same A and B parameters in the theory model of RB provided in Appendix A.4. (b) An error budget of the calculated coherent errors at a flux offset of $\delta\Phi_{\text{ext}}/\Phi_0 = 3 \times 10^{-5}$: the detuning error (dashed line), the state $|2\rangle$ leakage (dot-dashed line), and the state $|3\rangle$ leakage (dotted line) for different gate time t_π. (c) Gate errors extracted from RB measurements as a function of gate time t_π (black diamonds) plotted with the theoretical total gate errors including coherent and incoherent errors calculated at different flux offset values. The incoherent error contribution is estimated using the values of T_2^* from Fig. 3.2(c).

space due to the pumping rate of $|1\rangle - |2\rangle$ coming from the unconventionally low frequency of ω_{12}, which needs to be further investigated in future experiments.

Chapter 4: Stable and Accurate Gates on Inductively Coupled Fluxonium Qubits

4.1 Coupling Scheme

In this section, we describe an inductively-coupled two-fluxonium device. The fluxonium circuits share a common junction, which acts as a linear mutual inductance. The drive is applied via the qubit's external antenna-like capacitors, which also couple both qubits to a 3D cavity for a joint dispersive readout. The antennas are convenient for creating wireless microwave drives, but they also create capacitive links between circuit terminals, and they need to be taken into account for accurate modeling of the interactions. A small mutual inductance is indeed sufficient to hybridize qubits with relatively far detuned transitions ($f_{01}^{A} = 150$ MHz, $f_{01}^{B} = 230$ MHz) to create an on-demand cross-resonance (CR) interaction (ZX-term) comparable to the Rabi rates of single-qubit gates while the static ZZ-term is suppressed to a few kHz. The capacitance cross-talk does not affect the magnitude of the ZX-term but influences the static ZZ-term. In particular, it creates a previously overlooked LC mode, which, in general, must be taken into account when identifying the spectrum and transition matrix elements of the coupled system. Observation and quantitative modeling of this mode, along with the demonstration of the nearly ideal transversely-coupled spin-$1/2$ Hamiltonian in the computational sub-space, constitute the main focus of this section.

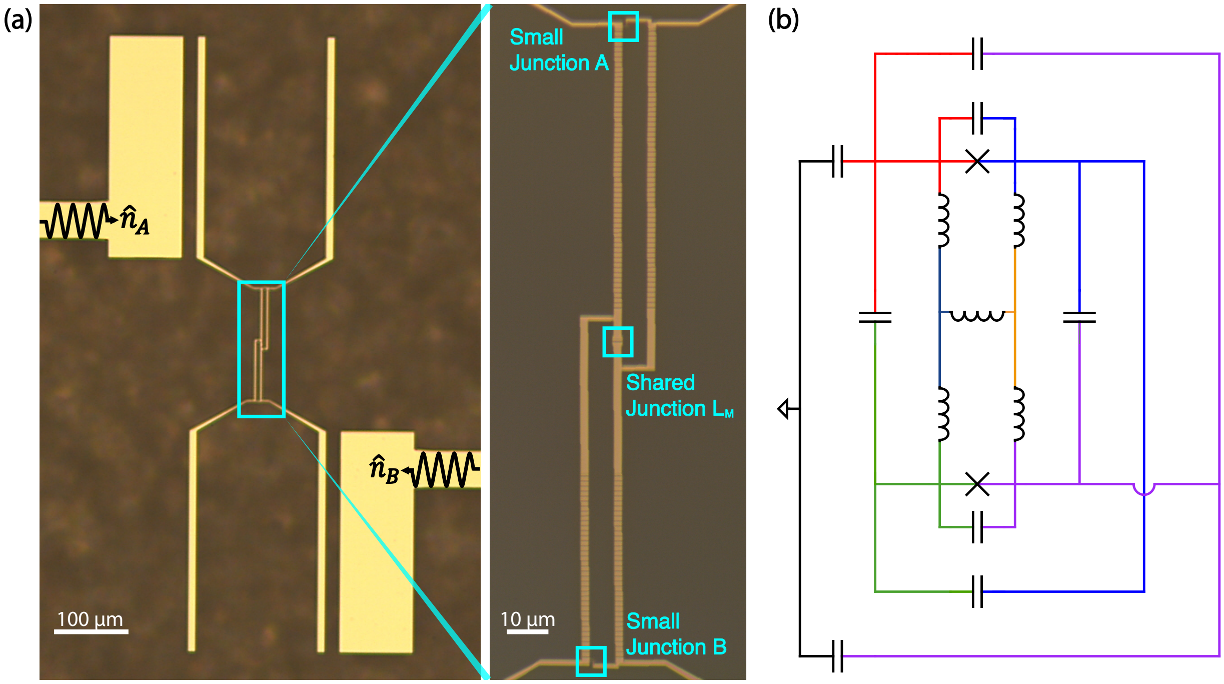

Figure 4.1: (a) The optical image of the two-fluxonium inductively coupled device. The joint readout cavity is not shown. The inset shows the mutual inductance L_M and locations of the fluxoniums' small junctions. The left and right leads are designed to drive qubits A and B, respectively, illustrated by the microwave signal symbols with the charge operator $\hat{n}_{A(B)}$. (b) The full circuit diagram of the device. Colors correspond to the nodes connecting inductors, capacitors, and small junctions.

4.1.1 Device and circuit model

Our device consists of two fluxoniums biased at the half-flux sweet spot without flux modulation that exhibit the behavior of a transversely coupled spin-1/2 system discussed in Section 2.5.1. The system's lowest energy states serve as the computational basis $|00\rangle$, $|10\rangle$, $|01\rangle$, and $|11\rangle$, revealing the symmetric nature of two coupled spin-1/2 as illustrated in the following sections.

We start with constructing the full Hamiltonian and demonstrate the analogy between our system and transversely coupled spin-1/2 systems later with the property derived from the device parameters of the Hamiltonian. The Hamiltonian of two inductively and capacitively coupled fluxonium circuits can be written as follows [68].

$$\frac{\hat{\mathcal{H}}_{\text{fl}}}{h} = \frac{\hat{\mathcal{H}}_A}{h} + \frac{\hat{\mathcal{H}}_B}{h} + J_C \hat{n}_A \hat{n}_B + J_L \hat{\varphi}_A \hat{\varphi}_B. \tag{4.1}$$

The first two terms describe uncoupled qubits (labeled $\alpha = A, B$),

$$\frac{\hat{\mathcal{H}}_\alpha}{h} = 4E_{C,\alpha}\hat{n}_\alpha^2 + \frac{1}{2}E_{L,\alpha}\hat{\varphi}_\alpha^2 - E_{J,\alpha}\cos\left(\hat{\varphi}_\alpha - \phi_{\text{ext}}\right), \tag{4.2}$$

where E_J, E_C, and E_L are the charging, Josephson, and inductive energy, respectively. The capacitive and inductive coupling strengths are J_C and J_L, and the charge operator is $2e\hat{n}$. The flux operator is $(\hbar/2e)\hat{\varphi}$ obey the canonical commutation relation $[\hat{n}, \hat{\varphi}] = i$; a global magnetic field (assuming equal area loops) creates a phase bias ϕ_{ext}. A more thorough circuit analysis for our device shown in Fig. 4.1(a) reveals the presence of an additional bosonic LC-mode based on the node flux analysis of Fig. 4.1(b), modifying the system Hamiltonian to

$$\frac{\hat{\mathcal{H}}}{h} = \frac{\hat{\mathcal{H}}_{\text{fl}}}{h} + f_{LC}\hat{a}^\dagger\hat{a} - i\sum_{\alpha=A,B} g_\alpha \hat{n}_\alpha \left(\hat{a} - \hat{a}^\dagger\right). \tag{4.3}$$

$\hat{a}$, and $\hat{a}^\dagger$ are the creation and annihilation operators of the bosonic mode. f_{LC} represents the LC-mode frequency. Its coupling strength to the qubit α is g_α. The physical picture of this bosonic mode is the LC resonator built from the inductance of the chain junctions and the capacitance between the upper and lower capacitor pads in Fig. 4.1(a). Combined with the readout resonator, we reach the full Hamiltonian

$$\begin{aligned}\hat{\mathcal{H}}_{\text{stat}} = {} & \hat{\mathcal{H}}_A + \hat{\mathcal{H}}_B + \hat{\mathcal{H}}_r + \hat{\mathcal{H}}_p \\ & + J_L \hat{\varphi}_A \hat{\varphi}_B + J_C \hat{n}_A \hat{n}_B \\ & - i[g_{A,r} \hat{n}_A (\hat{a}_r - \hat{a}_r^\dagger) + g_{B,r} \hat{n}_B (\hat{a}_r - \hat{a}_r^\dagger)] \\ & - i[g_{A,p} \hat{n}_A (\hat{a}_p - \hat{a}_p^\dagger) + g_{B,p} \hat{n}_B (\hat{a}_p - \hat{a}_p^\dagger)] \,, \end{aligned} \tag{4.4}$$

where $\hat{\mathcal{H}}_i = \hbar\omega_i \hat{a}_i^\dagger \hat{a}_i$ describes the readout and spurious LC bosonic modes with $i = r$ and p, respectively. The Hamiltonian parameters for the device in question, obtained from the analysis of the measured spectrum, are summarized in Table 4.5. We also note that the sign of J_L is always positive, while the sign of J_C can either depend on the details of the capacitive cross-talk network.

Qubit	$E_{C,\alpha}/h$ (GHz)	$E_{L,\alpha}/h$ (GHz)	$E_{J,\alpha}/h$ (GHz)	J_C/h (GHz)	J_L/h (GHz)	Bosonic Mode	$\omega_i/2\pi$ (GHz)	$g_{A,i}/h$ (GHz)	$g_{B,i}/h$ (GHz)
A	0.980	0.763	5.591	-0.038	0.0041	r	7.4750	-0.115	0.115
B	0.993	1.155	6.271			p	3.2165	-0.182	0.208

Table 4.1: Hamiltonian parameters of the two-qubit device.

4.1.2 System characterization

The measurement setup is illustrated in A.3. The chip is placed inside a 3D copper cavity with a resonance frequency of 7.475 GHz, and a linewidth $\kappa/2\pi = 9$ MHz for dispersive joint readout. External driving is introduced into the cavity through two input ports, with the more strongly coupled output port used to measure the transmission signal. The cavity is thermally anchored in the base plate of a dilution refrigerator at a temperature of 14 mK. The device spec-

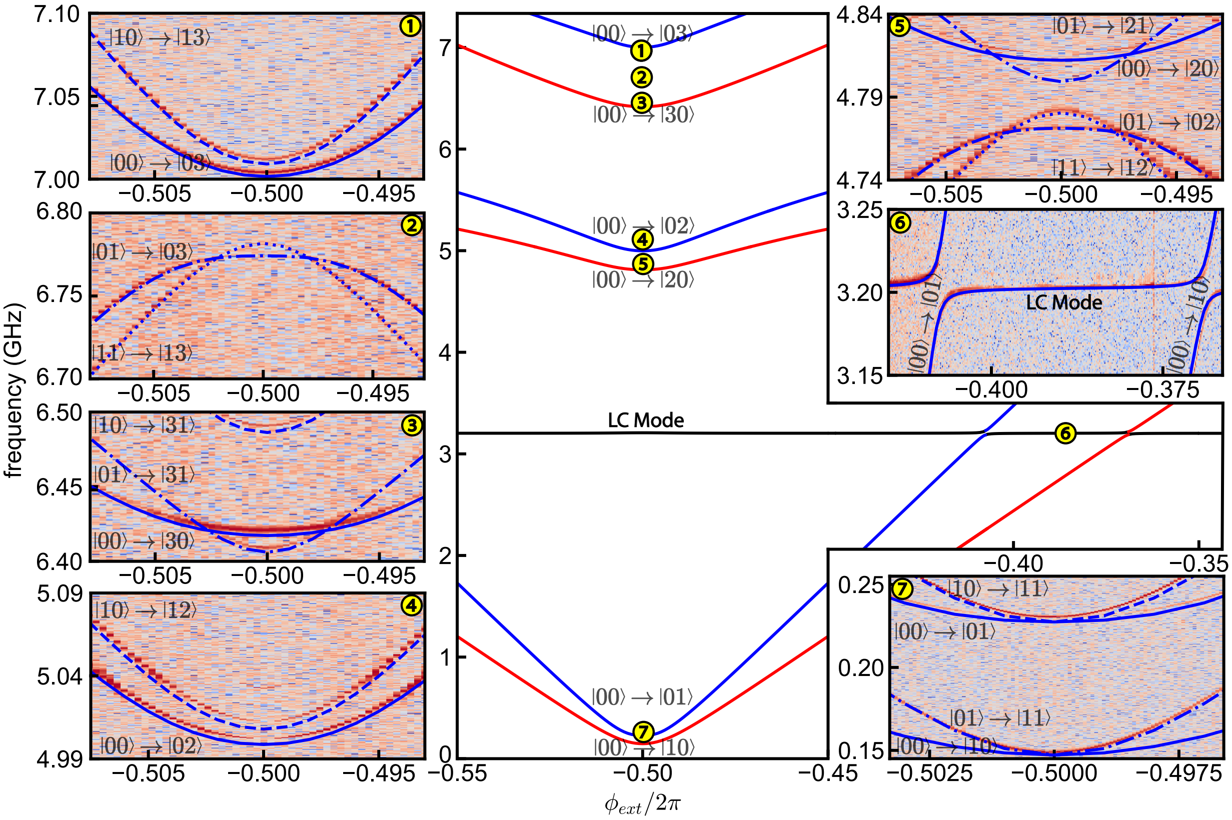

Figure 4.2: Fit spectral lines for qubit A (red) and B (blue), assuming adiabatic indexing of the coupled system. The data is shown in insets indexed from ① to ⑦. The computational sub-space is shown in inset ⑦, the stray LC-mode and its interaction with the qubits is shown in inset ⑥, and the other insets show various non-computational transitions, all in good agreement with theory.

trum is measured using a standard two-tone experiment technique, where the cavity readout tone follows the system excitation tone. By fitting the spectrum at various external flux points using the numerical diagonalization of the Hamiltonian presented in Eq. 4.3, the qubit parameters are extracted, as shown in Table 4.5.

Figure 4.2 shows the device spectrum with theoretical spectrum lines based on qubit parameters in Table 4.5, and the data is shown in the insets from ① to ⑦. Insets ① to ③ show the transitions involving the $|3\rangle$ state, ④ and ⑤ illustrate the transitions involving the $|2\rangle$ state, ⑥ highlights the LC-mode of the system, and inset ⑦ focuses on the transitions involving the $|1\rangle$

state at half flux quantum. The black line in the main figure represents the spurious LC-mode of the system. In the main figure, each index marks the corresponding region for the insets. The two-tone spectroscopy data in Fig. 4.2 reveals that the $|0\rangle - |1\rangle$ transition frequencies for qubits A and B are 0.15 GHz and 0.23 GHz, respectively. The $|1\rangle - |2\rangle$ transition frequencies are near 4.66 GHz and 4.78 GHz, giving the large anharmonicities of 4.51 GHz for qubit A and 4.54 GHz for qubit B. The relatively large anharmonicity compared with the qubit frequency indicates the leakage to higher energy levels while driving qubits can be significantly suppressed.

4.1.3 Static ZZ characterization

Figure 4.3(a) and (b) present the numerical charge and phase matrix elements, respectively, for the $|0\rangle - |1\rangle$ and $|1\rangle - |2\rangle$ transitions using our bare qubit parameters without any qubit-qubit coupling. We selected the $|1\rangle - |2\rangle$ transition to represent the non-computational space because it exhibits much larger values than other non-computational transitions. Notably, the ratio $|\langle 0|\hat{n}_\alpha|1\rangle/\langle 1|\hat{n}_\alpha|2\rangle| < 1$ implies that achieving strong hybridization of the $|01\rangle$ and $|10\rangle$ states without involving higher energy states is challenging, potentially leading to ZZ interactions if higher energy states are involved. Conversely, the ratio $|\langle 0|\hat{\varphi}_\alpha|1\rangle/\langle 1|\hat{\varphi}_\alpha|2\rangle| > 1$ suggests that the influence of higher energy states is suppressed. Combining with the large frequency detuning between the qubit A (B) transition and the $|1\rangle - |2\rangle$ transition of qubit B (A), this enables strong hybridization between the $|01\rangle$ and $|10\rangle$ states with negligible ZZ interaction, resembling a pair of transversely coupled spin-1/2. To be specific, we next analyze the scheme using our device parameters. In spin-based qubit representations, interactions are

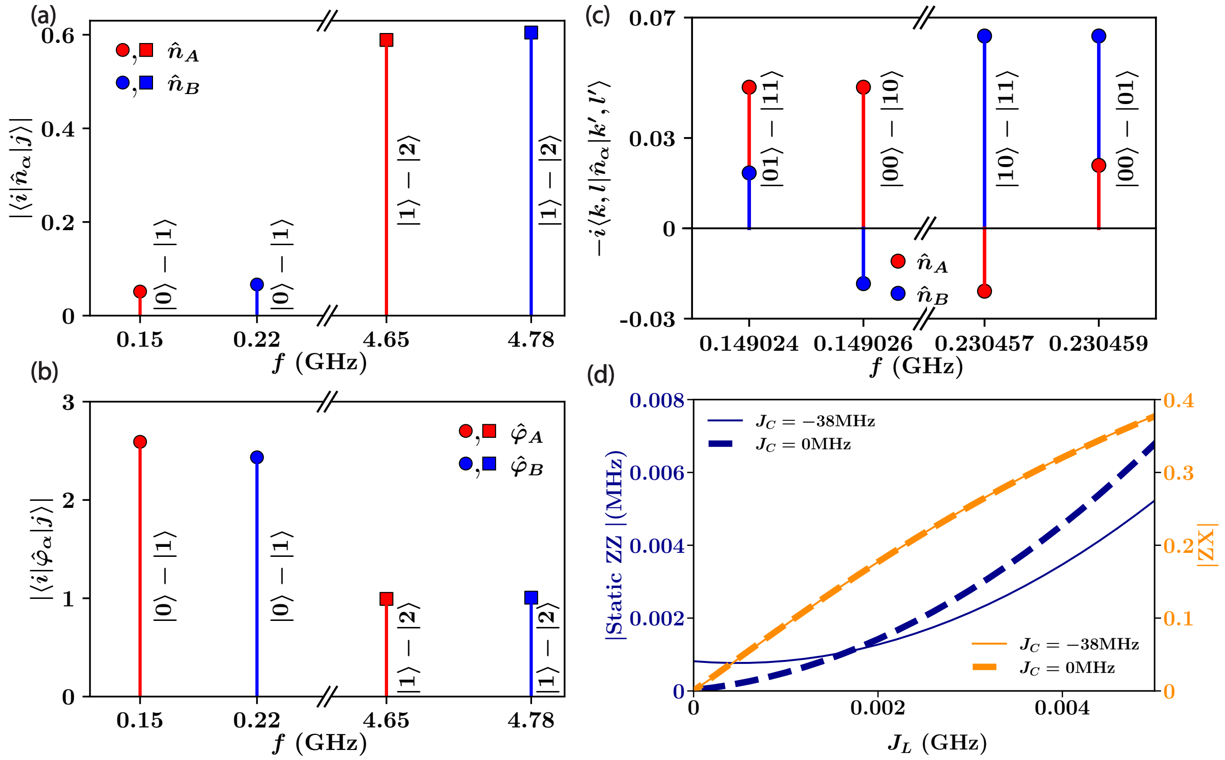

Figure 4.3: The charge (a) and phase (b) matrix elements of the two inidividual qubits without coupling. The qubit parameters are listed in Table I. (c) Two-qubit charge matrix elements for computational transitions. Note, their almost symmetric structure is nearly identical to those of a system of two transversly-coupled spin-half systems, following Eq. 2.57 and 2.58. The qubit frequencies are extracted from Ramsey measurements. (d) Numerical values of the static ZZ and the ZX-term. Note the coupling capacitances have no effect on the ZX-term and a minor effect on the ZZ-term.

typically expressed in terms of Pauli operators, such as $J\sigma_x\sigma_x$. In contrast, fluxonium qubits are described using charge ($\hat{n}$) and phase ($\hat{\varphi}$) operators, leading to capacitive coupling terms $J_C\hat{n}_A\hat{n}_B$ and inductive interactions $J_L\hat{\varphi}_A\hat{\varphi}_B$. To determine the coupling strength in the spin representation, the charge and phase matrix elements from Fig. 4.3(a), (b) must be considered. The capacitive and inductive coupling strengths can be evaluated using the following expressions: $|J_C\langle 0|\hat{n}_A|1\rangle\langle 0|\hat{n}_B|1\rangle|$ and $|J_L\langle 0|\hat{\varphi}_A|1\rangle\langle 0|\hat{\varphi}_B|1\rangle|$. With $J_C = -38\,\text{MHz}$ and $J_L = 4\,\text{MHz}$, the capacitive coupling contributes approximately $0.1\,\text{MHz}$, while the inductive coupling dominates at around $20\,\text{MHz}$ due to the large phase matrix elements, as shown in Fig. 4.3(b). The coupling to higher-level transitions due to the large $|\langle 1|\hat{n}_A|2\rangle|$ and $|\langle 1|\hat{n}_B|2\rangle|$ in Fig. 4.3(a) is significantly suppressed considering $|J_C\langle 1|\hat{n}_A|2\rangle\langle 0|\hat{n}_B|1\rangle|$ and $|J_C\langle 0|\hat{n}_A|1\rangle\langle 1|\hat{n}_B|2\rangle| \approx 1\,\text{MHz}$, which is still much smaller than the $4.5\,\text{GHz}$ anharmonicity. The same idea applies to $|J_L\langle 1|\hat{\varphi}_A|2\rangle\langle 0|\hat{\varphi}_B|1\rangle|$ and $|J_L\langle 0|\hat{\varphi}_A|1\rangle\langle 1|\hat{\varphi}_B|2\rangle| \approx 10\,\text{MHz}$.

As a result, our system utilizing direct coupling achieves a low static ZZ value, approximately 2 kHz. To accurately extract this value, we conduct Ramsey experiments on qubit B while setting qubit A to either its ground state or its excited state as shown in Fig. 4.4. The difference in the frequencies between the two Ramsey fringes is given by $\zeta_{ZZ}^{\text{static}}$. We then fit the oscillations to extract the two transition frequencies with a decaying sinusoidal function, and subtract the two frequencies to get the value of $\zeta_{ZZ}^{\text{static}}$:

$$\xi_{ZZ}^{\text{static}} = f_{|00\rangle-|01\rangle} - f_{|10\rangle-|11\rangle}. \tag{4.5}$$

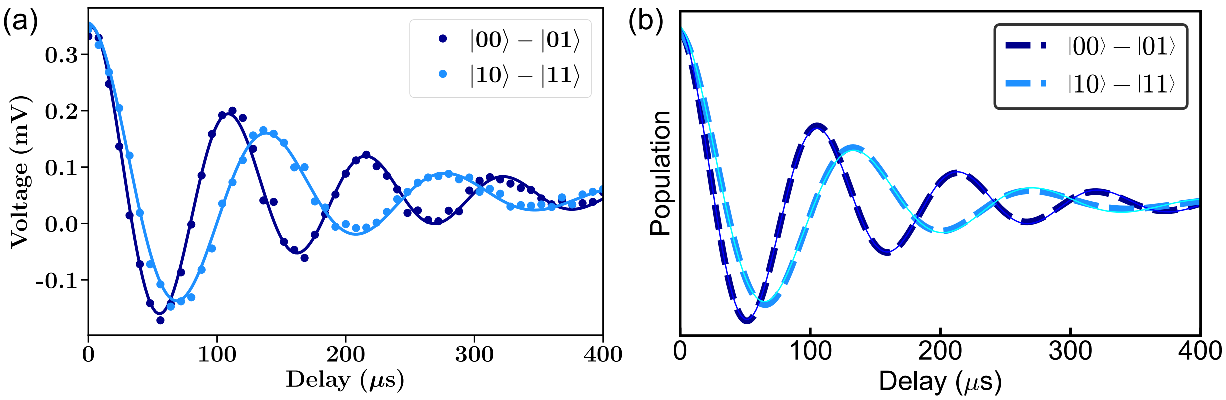

Figure 4.4: (a) Measured and (b) simulated Ramsey fringe of qubit B conditioned on the state of qubit A. The experiment involves measuring the static ZZ coupling strength with qubit A in the $|0\rangle$ state (dark blue) and in the $|1\rangle$ state (blue). The difference of the two Ramsey frequencies gives the static ZZ-shift, $\xi_{ZZ}^{\text{static}} = 2$ kHz. The measurement relies on a relatively long decoherence time of the two-qubit system. To investigate the effect of the control qubit relaxation during the Ramsey measurements, we simulate the full dynamics in (b) based on Lindblad master equations (dashed lines) and fit the evolution traces with a decaying sinusoidal function (solid thin lines) as we do for the experiments in (a). Both (a) and (b) show discrepancy when delay is larger than 200 μs. The fitting result in (b) shows that if the static ZZ value extracted from fitting is 2 kHz, the actual static ZZ of the system is 2.3 kHz.

4.1.4 Truncating to the 4 computational states

4.1.4.1 Cross-resonance interaction

Having established the accurate circuit model via spectroscopy, we proceed with truncating the system to its four lowest computational energy states:

$$\frac{\hat{\mathcal{H}}_{\text{eff}}}{h} = \frac{f_{01}^{A}}{2}\hat{\sigma}_z^A + \frac{f_{01}^{B}}{2}\hat{\sigma}_z^B + \frac{\xi_{ZZ}^{\text{static}}}{4}\hat{\sigma}_z^A\hat{\sigma}_z^B + \frac{\hat{\mathcal{H}}_{\text{drive}}}{h}, \tag{4.6}$$

where h is the Plank constant. $f_{01}^{A,B}$ is the frequency of qubits A and B, and $\hat{\sigma}_z^{A,B}$ are the corresponding Pauli operators. The quantity ξ_{ZZ}^{static} represents the static ZZ interaction rate measured in Fig. 4.4. The microwave drive Hamiltonian in the computational subspace reduces to

$$\frac{\hat{\mathcal{H}}_{\text{drive}}}{h} = \beta(t)\left(\xi_A^+ \hat{\sigma}_x^A + \xi_A^- \hat{\sigma}_x^A \hat{\sigma}_z^B + \xi_B^+ \hat{\sigma}_x^B + \xi_B^- \hat{\sigma}_z^A \hat{\sigma}_x^B\right), \tag{4.7}$$

where $\beta(t) = \bar{\beta}(t)\cos(2\pi f_d t + \phi)$ describes the time dependence of the drive determined by the drive frequency f_d, the phase ϕ, and the slow-varying drive-envelop function $\bar{\beta}(t)$. The real factors ξ_A^+, ξ_A^-, ξ_B^+, and ξ_B^- represent effective XI, XZ, IX, and ZX interactions, respectively, which can be written in terms of purely imaginary charge matrix elements as

$$\begin{aligned} i\xi_A^\pm &= \langle 00|\epsilon_A \hat{n}_A + \epsilon_B \hat{n}_B|10\rangle \pm \langle 01|\epsilon_A \hat{n}_A + \epsilon_B \hat{n}_B|11\rangle, \\ i\xi_B^\pm &= \langle 00|\epsilon_A \hat{n}_A + \epsilon_B \hat{n}_B|01\rangle \pm \langle 10|\epsilon_A \hat{n}_A + \epsilon_B \hat{n}_B|11\rangle. \end{aligned} \tag{4.8}$$

The drive amplitudes ϵ_A and ϵ_B are real and represent two in-phase drives on the two fluxoniums. The relation of ϵ_A, ϵ_B to the actual field amplitudes applied to the drive lines are discussed in Section 4.2.2.3. To further understand the relation between the interaction rates ξ_A^+, ξ_A^-, ξ_B^+, ξ_B^- and the two external drive fields ϵ_A, ϵ_B applied to fluxonium A, B, we can rewrite Eq. 4.8 as

$$\begin{bmatrix} \xi_A^\pm \\ \xi_B^\pm \end{bmatrix} = \begin{bmatrix} M_{AA}^\pm & M_{AB}^\pm \\ M_{BA}^\pm & M_{BB}^\pm \end{bmatrix} \begin{bmatrix} \epsilon_A \\ \epsilon_B \end{bmatrix}. \tag{4.9}$$

Table 4.2: Charge matrix elements of the transitions inside computational space for charge drives on the two fluxoniums.

$-i\langle kl\|\hat{n}_j\|k'l'\rangle$	$\hat{n}_A$	$\hat{n}_B$
$\|00\rangle - \|10\rangle$	0.046865	-0.018371
$\|01\rangle - \|11\rangle$	0.046871	0.018397
$\|00\rangle - \|01\rangle$	0.020908	0.063885
$\|10\rangle - \|11\rangle$	-0.020883	0.063873

with

$$\begin{aligned} M_{AA}^{\pm} &= -i[\langle 00|\, \hat{n}_A \,|10\rangle \pm \langle 01|\, \hat{n}_A \,|11\rangle], \\ M_{AB}^{\pm} &= -i[\langle 00|\, \hat{n}_B \,|10\rangle \pm \langle 01|\, \hat{n}_B \,|11\rangle], \\ M_{BA}^{\pm} &= -i[\langle 00|\, \hat{n}_A \,|01\rangle \pm \langle 10|\, \hat{n}_A \,|11\rangle], \\ M_{BB}^{\pm} &= -i[\langle 00|\, \hat{n}_B \,|01\rangle \pm \langle 10|\, \hat{n}_B \,|11\rangle]. \end{aligned} \tag{4.10}$$

Matrix elements $M_{kl}^{\pm}$ connect the interaction rates $\xi_k^{\pm}$ and the drive amplitudes ϵ_l with $k, l = \{A, B\}$.

4.1.4.2 Two-qubit charge matrix elements

In this section, we describe the charge matrix elements of the transitions within the computational space as shown in Fig. 4.3(c) and Table. 4.2. These matrix elements define the coefficients 4.8 of the time-dependent Hamiltonian (4.7). Specifically, we can treat these coefficients as four control knobs: (i) the local drive ϵ_A at the frequency f_{01}^A, (ii) the local drive ϵ_B at the frequency f_{01}^A, (iii) the local drive ϵ_B at the frequency f_{01}^B, and (iv) the local drive ϵ_A at the frequency f_{01}^B. These control knobs provide tuning the XI, XZ, IX, and ZX interaction rates individually, simplifying the operational complexity of cross-resonance gates.

A direct drive ϵ_A (ϵ_B) at the frequency f_{01}^A (f_{01}^B) causes the Rabi oscillations in qubit A (B)

Table 4.3: Matrix elements in Eq. (4.9) connecting the interaction rates $\xi_k^\pm$ and the local drive amplitudes ϵ_l with $k, l = A, B$.

M_{kl}^+	$l = A$	$l = B$	M_{kl}^-	$l = A$	$l = B$
$k = A$	0.093736	0.000026	$k = A$	-0.000006	-0.036768
$k = B$	0.000025	0.127758	$k = B$	0.041791	0.000012

subspace with the Rabi frequency determined by the matrix elements $\langle 01|\hat{n}_A|11\rangle$ and $\langle 00|\hat{n}_A|10\rangle$ ($\langle 10|\hat{n}_B|11\rangle$ and $\langle 00|\hat{n}_B|01\rangle$). These pairs of matrix elements have the same magnitude and sign regardless of the state of the other qubit, the condition necessary for single-qubit gates. On the other hand, a cross-resonant drive ϵ_A (ϵ_B) at the frequency f_{01}^B (f_{01}^A) generates rotation of qubit B (A) state with the Rabi frequency proportional to the matrix elements $\langle 10|\hat{n}_A|11\rangle$ and $\langle 00|\hat{n}_A|01\rangle$ ($\langle 01|\hat{n}_B|11\rangle$ and $\langle 00|\hat{n}_B|10\rangle$). Each pair of these matrix elements has the same magnitudes but opposite signs, resulting in state rotations in opposite directions, dependent on the state of qubit A (B). This behavior is suitable for conditional two-qubit gates. The four matrix elements relevant to the cross-resonant drive have magnitudes comparable to those relevant to the direct drive, indicating strong hybridization of computational states. The similarity of matrix elements under strong hybridization indicates the feature of a transversely coupled spin-1/2 system, providing a simple scenario for gate operations with low complexity.

Alternatively, we can try to understand the same physics by the values of $M_{kl}^\pm$ computed from Table 4.2, which are provided in Table 4.3. It is noteworthy that these values account for quantum crosstalks and are irrelevant to classical crosstalks. Within the CR gate scenario, we can apply any linear combination of the two local drives, ϵ_A and ϵ_B, at the frequency f_{01}^A or f_{01}^B, thus inducing resonant transitions in qubit A or B, respectively. To have a better understanding of our system, we can see M_{AA}^-, M_{BB}^-, M_{AB}^+, and M_{BA}^+ are all close to 0, meaning that the local drive ϵ_A (ϵ_B) at its own qubit frequency f_{01}^A (f_{01}^B) provides the XI (IX) interaction, while driving it at the qubit B (A) frequency f_{01}^{B} (f_{01}^{A}) provides the ZX (XZ) interaction, facilitating a simple scheme for gate operations. Note that the CR drive ϵ_B (ϵ_A) at the frequency f_{01}^{A} (f_{01}^{B}) corresponds to M_{AB}^{-} (M_{BA}^{-}), showing magnitude comparable to M_{AA}^{+} (M_{BB}^{+}). This indicates the strong hybridization of our computational space, providing a large XZ (ZX) rate under CR drive that is comparable to the XI (IX) rate of single-qubit gates. Even though the computational states are strongly hybridized, a single local drive ϵ_A (ϵ_B) at the frequency f_{01}^{A} (f_{01}^{B}) synchronizes single-qubit gates without XZ (ZX) interaction. The elements with magnitude well below 10^{-4} in Table 4.2 make our device suitable for single and two-qubit gates and is consistent with the features of transversely coupled spin-1/2 systems.

4.1.4.3 Magnitude of the ZX-term

We further investigate the resulting magnitude of the ZX-interaction under the same drive amplitude for single-qubit gates. We evaluate this entangling strength using the following expression:

$$\begin{aligned} |ZX| &= \left| \frac{\xi_B^{-}\left(\epsilon_A = \epsilon, \epsilon_B = 0\right)}{\xi_B^{+}\left(\epsilon_A = 0, \epsilon_B = \epsilon\right)} \right| \\ &= \left| \frac{\langle 00|\hat{n}_A|01\rangle - \langle 10|\hat{n}_A|11\rangle}{\langle 00|\hat{n}_B|01\rangle + \langle 10|\hat{n}_B|11\rangle} \right|, \end{aligned} \tag{4.11}$$

The numerator represents the cross-resonant drive with ϵ_A turned on, and ϵ_B turned off, and the denominator represents the direct drive with ϵ_A turned off, and ϵ_B turned on. Figure 4.3(d) shows $|ZX|$ as a function of the inductive coupling strength J_L along with the static ZZ phase accumulation rate. We observe that the ZX term grows linearly while the ZZ term grows quadratically in J_L. This facilitates a significant separation of the two frequency scales. For the device in question, a purely inductive coupling of $J_L = 4\ \mathrm{MHz}$ (neglecting the capacitive effects, that is setting $J_C = 0$ and $g_{A(B)} = 0$) results in a relatively small $\xi_{ZZ}^{\text{static}} = 5\ \text{kHz}$, while the ZX term can readily be close to 0.4. We also observe that the capacitive cross-talk does not affect the ZX-term at all for the device in question and helps suppress the ZZ-term a bit. The measured value of $2\ \mathrm{kHz}$ qualitatively agrees with the theoretical prediction. For comparison, previous work [38] utilizing capacitive coupling also employs direct coupling schemes designed for cross-resonance gates in charge-driven fluxonium systems. A key difference is the resulting static ZZ interaction, where the capacitive coupling case leads to a static ZZ of 900 kHz, while our inductively coupled system achieves a significantly lower value of 2 kHz.

4.2 Gate Operations

Among the plethora of high-fidelity gate schemes tested on transmons, those based on cross-resonance (CR) driving [25, 26, 81, 82, 83, 84, 85] would particularly benefit from the strong anharmonicity of fluxoniums [86]. In this case, the qubit frequencies are fixed to their half-quantum flux “sweet-spots” and the two-qubit dynamics under a CR-drive remains confined to the logical subspace, thereby not only eliminating leakage, but also minimizing the decoherence-related errors. In comparison, incoherent errors are likely to be enhanced in schemes relying on either a temporary departure from the sweet spot [35, 36, 87], or on a temporary population of the non-computational states [31, 32, 33]. A CR-gate on a pair of capacitively coupled fluxoniums was recently implemented [38], where it was shown that virtual excitations of the non-computational states can enhance the gate speed but simultaneously introduce a quantum cross-talk in the form of a static ZZ-term. The same effect is present in capacitively-coupled transmons and leads to coherent errors [88]. The quantum cross-talk can be canceled without suppressing the qubit-qubit hybridization by applying off-resonant drive to non-computational transitions [32, 38] or by the use of coupler modes [26, 27, 28, 29, 33, 33, 34, 35, 61, 62, 63, 64, 65, 89, 90, 91, 92, 93, 94, 95, 96, 97, 98, 99], but at the expense of increasing the complexity of the gate.

In the search for a maximally simple gate scheme, we revisit the original demonstration of a CR-type gate (also known as "selective darkening" or "direct CNOT" gate) on a pair of inductively coupled flux qubits [100], the ancestors of high-coherence fluxoniums. While the original demonstration did not result in high-fidelity benchmarks, it triggered further research of CR-type gates on capacitively-coupled C-shunted flux qubits [101] and transmons [102, 103]. It can be shown, however, that a pair of inductively-coupled fluxoniums does behave almost exactly as a pair of exchange-coupled spin-$1/2$ systems for a broad range of circuit parameters [2, 66, 68]. In particular, the quantum cross-talk is nearly absent without the need for narrow device parameter matching, coupler elements, sophisticated control pulses, or other complications. Thus an inductive coupling of fluxoniums allows us to test the cross-resonance gate the way it was originally envisioned two decades ago for a pair of true two-level systems [104].

Simplifying the gate scheme is likely crucial for achieving a robust highest-fidelity operation. There have been a number of demonstrations of two-qubit gates on transmons and fluxoniums with a fidelity approaching 99.9% [22, 25, 28, 29, 33, 34]. However, there are still very few that reliably cross this threshold [33, 34]. Furthermore, maintaining the gate fidelity beyond 99.9% during prolonged operations without requiring frequent recalibration is also important. In this section, we report a controlled π rotation (CX_{π}) gate with a duration of approximately 60 ns (equivalent to the CNOT gate after a virtual rotation). The gate fidelity was estimated using con-

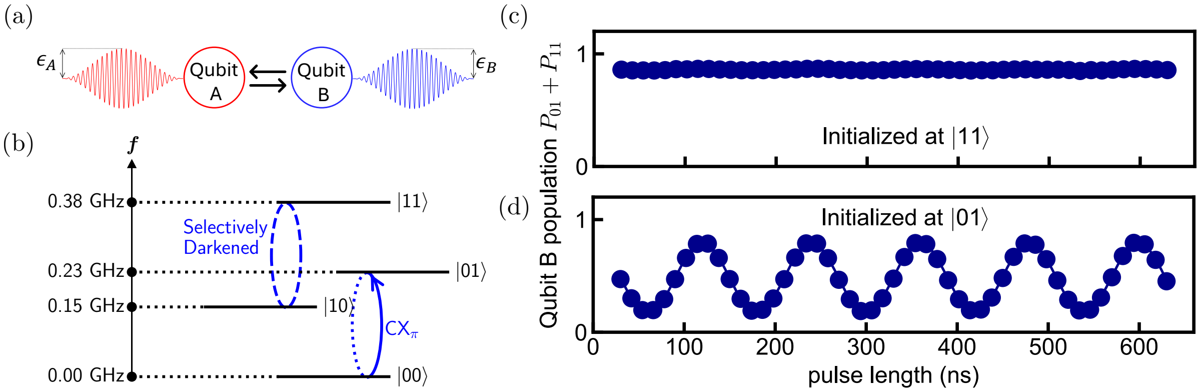

Figure 4.5: (a) Illustration of two local charge drives for various gate operations. (b) Energy levels of our two-qubit system. The blue lines illustrate the scheme of the two-qubit CX_π gate based on selective darkening. (c),(d) Conditional Rabi oscillation of qubit B initialized at $|11\rangle$,$|01\rangle$, respectively, comparing the dynamics of the dark ($|10\rangle$-$|11\rangle$) and bright ($|00\rangle$-$|01\rangle$) transitions under selective darkening CR drive. The small oscillation in (c) is due to imperfect initialization causing residual population initialized at $|01\rangle$.

ventional randomized benchmarking described in appendix A.4 and its maximal value reaches 99.94%. More importantly, we show that fidelity stays above 99.9% for a period of 24 days following a manual optimization of 8 nearly decoupled parameters. We believe that this stability was achieved in part due to the simplification of the device (no coupler elements, no parameter matching) and the gate protocol (no driving of non-computational transitions, no flux tuning, and no pulse-shaping for leakage mitigation).

We apply microwave drives to manipulate our qubits as shown in Fig. 4.5(a). Figure 4.5(b) shows the qubit frequencies and level structures of the system. We fix the external magnetic field to bias qubits at the flux-insensitive sweet spot. The details of experimental procedures, such as initialization and readout, are provided in Appendix A.3.

4.2.1 Gate concept

In this section, we specify the essential conditions of the two CR gates, direct CX_π based on selective darkening and $ZX_{-\pi/2}$. For the description later in this section, we label the control qubit as A and the target qubit as B. In the $ZX_{-\pi/2}$ scheme, the two target qubit transitions rotate by the same angle but with opposite directions conditional on the control qubit state. The latter is achieved if $\langle 00|\hat{H}_{\text{drive}}|01\rangle = -\langle 10|\hat{H}_{\text{drive}}|11\rangle$. For CX_π gate based on selective darkening, we need to darken one of the target qubit transitions. In this paper, we choose $\langle 10|\hat{H}_{\text{drive}}|11\rangle = 0$, as illustrated in Fig. 4.5(b).

4.2.1.1 $ZX_{-\pi/2}$ gate

We provide a perspective on the gate operations using expression 4.7. To perform $ZX_{-\pi/2}$ gate, we drive the system resonantly at the transition frequency f_{01}^B of qubit B. We choose the drive amplitudes $\epsilon_{A,B}$ so that ξ_B^+ is strongly reduced. Thanks to the tiny value of the coefficient M_{BA}^+, see Table 4.2, this requirement is satisfied if $\epsilon_B = 0$ and $\epsilon_A \neq 0$. The conditional rotation of the target qubit is then achieved due to the resonant drive of qubit B transition with term $\xi_B^- = M_{BA}^- \epsilon_A$. Note that the terms driving the control qubit, $\xi_A^\pm$, do not vanish in this case and are responsible for the undesirable transitions of the control qubit. However, the contribution to the gate error for these transitions remain below 10^{-4} for gate times exceeding 50 ns.

4.2.1.2 CX_π gate

The CX_π gate with $\langle 10|\hat{H}_{\text{drive}}|11\rangle = 0$ requires $\xi_B^- = \xi_B^+$, which is satisfied by choosing $\epsilon_A/\epsilon_B \approx M_{BB}^+/M_{BA}^-$. This condition for our system is satisfied when the amplitudes $\epsilon_{A,B}$ are comparable to each other and do not require an irradiation of one of the qubits with extremely strong drive to have the gate time t_{gate} determined by the drive amplitude according to the following relation $\xi_B^- = \xi_B^+ \propto 1/t_{\mathrm{gate}}$. The off-resonant drive for the control qubit is defined by $\xi_A^\pm$ coefficients and cause transitions with relatively low probabilities for the gates longer than 50 ns, see Section 4.2.4.

4.2.1.3 Single-qubit gates

Next, we argue that our device is also suitable for single-qubit gates that require $\xi_{A,B}^- = 0$ and $\xi_{A,B}^+ \neq 0$. The values of coefficients $M_{kl}^\pm$ in Table 4.2 shows that a direct resonant drive of qubit A ($\epsilon_A \neq 0$ and $\epsilon_B = 0$) or qubit B ($\epsilon_A = 0$ and $\epsilon_B \neq 0$) will generate a rotation of the quantum state in the corresponding qubit computational subspace independent of the other qubit state.

We mention that our system is not restricted to selecting a particular fluxonium pair as the control-target qubits. The description above also applies to the gate operations driving at f_{01}^A. For example, our $ZX_{-\pi/2}$ experiments discussed in Section 4.2.3.2 utilize qubit A(B) as the target(control) qubit. In this case, the essential condition for the $ZX_{-\pi/2}$ gate is $\xi_A^+ = 0$.

4.2.2 Gate calibration

Our drive frequency f_d is on-resonant with the frequency of the bright transition $|00\rangle - |01\rangle$, which is extracted from the Ramsey measurement. To implement high-fidelity gates, we next iterate through tune-up sequences that are sensitive to specific errors and calibrate against the target parameters with a large and varying number of pulses to amplify the error for precise tuning.

Going beyond previous methods of calibrations, we sweep both the target pulse parameters and the numbers of repetitive pulses. This method reveals some signatures of untargeted errors such as the Stark shifts of dark transitions and single-qubit gate error, and allows us to determine the optimal pulse parameters in the presence of these additional imperfections, suppressing coherent errors down to the order of 10^{-4} without using any "black-box" optimization strategies. Our tune-up approach thus also offers more transparency and helps identify the dominant source of error when the fidelity dips after running the gate for a period of time. Further details are provided in the next section 4.2.2.1. The seven fine-tuned target parameters of our CR pulse are listed below along with the corresponding goals for a CX_π gate as an example: the relative amplitude and phase of the two port drives to selectively darken the $|10\rangle$-$|11\rangle$ transition, the DRAG coefficient [72, 73] with fixed drive frequency to achieve a big circle trajectory on the Bloch sphere, the overall drive amplitude to ensure a π rotation angle, the common pulse phase to align the rotation axis to X rotation, and the single-qubit phase accumulation of A and B due to the CR pulse to determine the phase values of virtual Z [105] compensation. The whole tuning process takes roughly three hours. Section 4.2.2.1 describes the time cost of each step and demonstrates the detailed procedure of CX_π gate tuning. Similar tune-up procedures for direct CNOT gates have been reported in [25, 38]. The tuning of $ZX_{-\pi/2}$ gate and single-qubit gates are also provided in Section 4.2.2.1 and 4.2.2.2, respectively.

4.2.2.1 Tune-ups of two-qubit cross-resonance gates

In experiments, two microwave drives are applied to the two qubits with a phase difference, which needs to be calibrated and canceled. This modifies the drive term of Hamiltonian to

$$\frac{\hat{H}_{\text{mw}}}{h} = \frac{\bar{\beta}(t)}{2}\left(e^{-i2\pi f_d t}(\epsilon_A \hat{n}_A + \epsilon_B \hat{n}_B) + \text{h.c.}\right), \tag{4.12}$$

where $\bar{\beta}(t)$ is a smooth function describing the drive amplitude at frequency f_d. The complex coefficients $\epsilon_{A,B}$ describe the amplitude and phase shift of the drive. Alternatively, we can also define a new variable, η, to better elaborate our tune-up process with $|\eta| = \epsilon_B/\epsilon_A$ (ϵ_A, ϵ_B are real), accounting for the relative amplitude of the two local drives. Our AWG needs to apply a phase offset arg(η) between the two drives to address any phase delay due to cables or electronics, making the pulses reaching our sample in-phase with a phase difference of 0 or π.

CX_π ***gate:***

Our CR pulse induce phase accumulation due to ac Stark shifts or higher-order CR effect [86], especially after increasing the drive amplitude for faster gates. Accordingly, we further define θ_A and θ_B as the phase accumulation of qubit A and B and introduce the evolution matrix of the CR pulse for a CX_π gate

$$\begin{pmatrix} 1 & 0 & 0 & 0 \\ 0 & e^{i\theta_B} & 0 & 0 \\ 0 & 0 & 0 & e^{i\theta_A} \\ 0 & 0 & e^{i\theta_A} & 0 \end{pmatrix}. \tag{4.13}$$

Here, we assume that the pulse is well tuned to induce a X rotation, and thus one single variable θ_A can cover the lower two matrix elements. To compensate θ_A and θ_B, we apply single-qubit virtual Z gates before ($-\theta_B/2$ on B) and after ($-\theta_B/2$ on B, $\theta_B/2 - \theta_A$ on A) the CR pulse to realize a CNOT gate [38, 86]. Note that a CNOT gate is equivalent to a CX_π followed by a S gate on qubit A, which can be implemented by a virtual Z gate at no additional cost. In this letter, we benchmark the CX_π gate

$$\begin{pmatrix} 1 & 0 & 0 & 0 \\ 0 & 1 & 0 & 0 \\ 0 & 0 & 0 & -i \\ 0 & 0 & -i & 0 \end{pmatrix} \tag{4.14}$$

instead of a textbook CNOT to point out the dynamics of the conditional rotation governed by Hamiltonian, while the results also apply to a CNOT gate.

Next, we demonstrate the tune-up process determining the eight target parameters, f_d, $|\eta|$, arg(η), ϵ_A, DRAG coefficient, ϕ, θ_A, and θ_B, in details. Note that we fix η while tuning ϵ_A, making it actually an overall amplitude tuning. We should point out that we do not perform any black-box optimizations such as Nelder-Mead or machine learning algorithms. We rely on the following calibration procedure targeting the eight parameters individually, allowing a shorter time cost and higher transparency. Among these tune-up criteria, we put emphasis on achieving the darkening condition with more iterations because the corresponding gate error is larger than the bright transition according to our analysis in Section 4.2.4. Additionally, the limited error amplification of the dark transition discussed later requires longer averaging time to get the precise values of the two corresponding target parameters. Each corresponding tune-up measurement takes more than ten minutes compared with the other steps taking only a few minutes. The whole tuning process takes roughly three hours. Note that our duty cycle for each measurement is over 100 μs due to hardware limitations, which is longer than the cycle length needed for a few hundreds of 60 ns pulses. The total tuning time can be largely suppressed with shorter duty cycles and automation codes. Fig. 4.7(a) shows the demodulated IQ values of the four computational states we prepare, serving as a scale for the latter calibrations.

First, f_d is simply the frequency of the bright transition $|00\rangle - |01\rangle$, which is extracted from Ramsey experiments as shown in Fig. 4.6(a). We fix this value for all the tuning procedures later.

Before fine-tuning, we first aim at the sub-precise values of $|\eta|$ and arg(η) to achieve the darkening condition. Since we can only achieve selective darkening with these two parameters being accurate, we iterate through the calibrations sweeping these two values to approach the darkening condition. The measurement we do for this calibration is first setting a rather low ϵ_A to avoid any crazy dynamics under high power and then sweeping the pulse width of our CR drive as shown in Fig. 4.6(b) to check the rabi oscillation of the dark transition $|10\rangle - |11\rangle$ and minimize the rabi frequeny until there's no oscillation showing a simple decay trace. The initial value of $|\eta|$ can be roughly calculated using Table. 4.2, so we first fix this rough $|\eta|$ and sweep arg(η) to get the rough arg(η) value. Fig. 4.7(b) shows the corresponding data for example. Then we go back to sweep $|\eta|$ for a more accurate value. We repeat this cycle of $|\eta|$ and arg(η) sweeping for a few times and determine the sub-precise values of these two parameters for the next step.

Then we move on to get the sub-precise ϵ_A for the target pulse width we set. We perform Rabi oscillation measurements as shown in Fig. 4.6(c) and sweep ϵ_A until our target pulse width induces a π rotation for the bright transition. Taking a 60 ns CX_π for example, one can set a pulse width of 600 ns (multiples of 60 ns) and find the corresponding ϵ_A giving the peak value

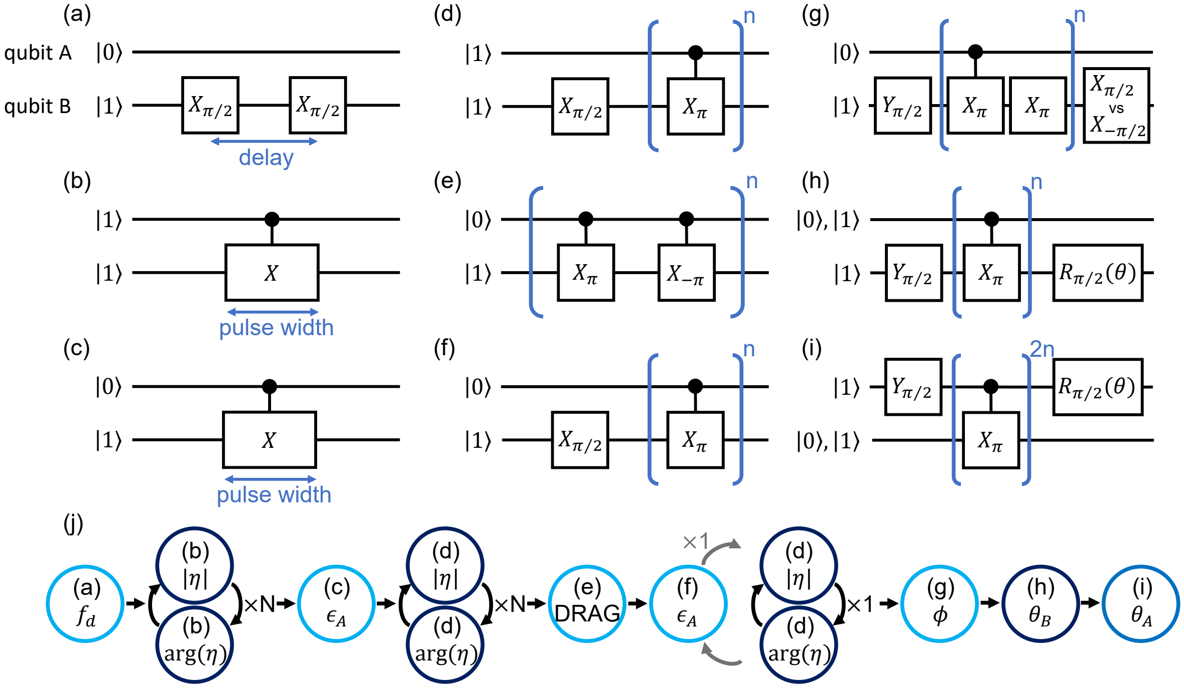

Figure 4.6: Pulse sequences and flow chart for CX_π gate tune-up with corresponding data shown in Fig. 4.7: (a) Determining drive frequency by Ramsey experiments. (b)-(c) Rough tuning getting the sub-precise values of the overall amplitude, relative amplitude, and relative phase of the two drives. (b) Calibrating relative amplitude and phase by nulling Rabi frequency to achieve darkening condition. (c) Setting target pulse width and calibrating the corresponding overall amplitude by measuring Rabi oscillation experiments. (d)-(i) Fine tuning with a large varying number of CR pulses to amplify the target error for precise calibration. (d) Calibrating relative amplitudes and relative phase by checking darkening condition, making sure qubit B does not rotate. (e) DRAG calibration by repeating CR pulses with alternating amplitude, making sure that qubit B is driven along the big circle on Bloch sphere. (f) Calibrating the overall drive amplitude by making sure there is no over or under rotations. (g) Calibrating the rotation axis misalignment of CR pulses with respect to the single qubit gate of B, making sure the rotation axis aligns with the X-axis of qubit B. (h),(i) Measuring the single qubit phases of qubit A,B, respectively, needed for compensating phase accumulation due to each CR pulse. Same sequences confirm all accumulated phases are corrected after calibration. (j) Illustration of the full two-qubit gate calibration process. The pulse sequences and corresponding target parameters are provided in the graphical circles. Dark (light) blue circles indicate the dark (bright) transition, while the last normal blue one denotes the control qubit transitions. The iteration number N typically equals to 2 or 3.

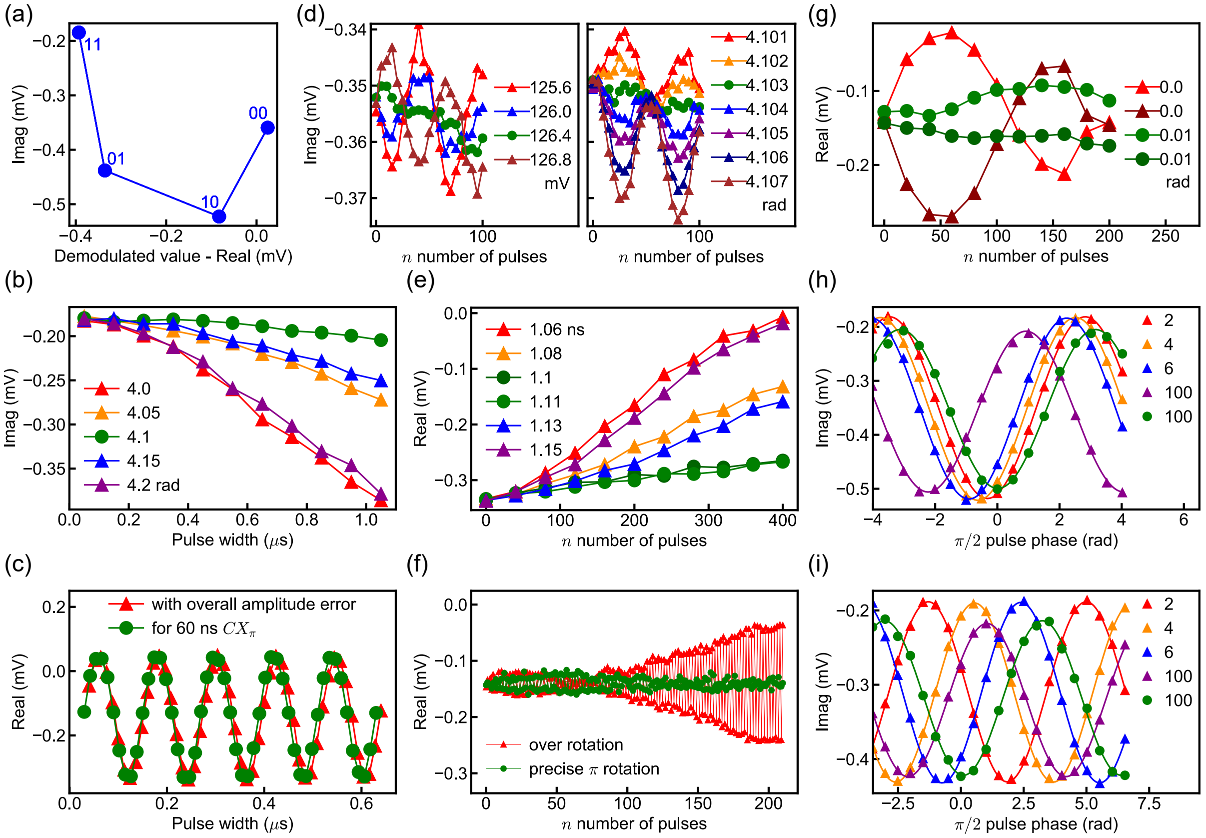

Figure 4.7: Corresponding CX_π gate tune-up data for Fig. 4.6 (b)-(i). The optimized trace (green circle) for each target parameters are shown along with the corresponding error syndrome (red triangle). (a) The demodulated IQ values of the four computational states we prepared, serving as a reference for (b)-(i). We later show the real part for the bright transition $|00\rangle - |01\rangle$ and the imaginary part for the dark transition $|10\rangle - |11\rangle$ in order to show a better contrast. (b) Nulling oscillation frequency to achieve darkening condition, showing the relative phase sweeping as an example, while the relative amplitude sweeping has the same syndrome. (c) Rabi oscillations of a well tuned overall amplitude corresponding to a 60 ns target pulse width and the one with under rotation. (d) Two example data of the iteration through the relative amplitude (left panel) and phase (right panel) sweeping to approach the darkening condition, making sure no detuned Rabi oscillation is observed. (e) Sweeping DRAG and Nulling oscillation frequency to move the rotation axis onto the equator, making qubit B driven along the big circle on Bloch sphere. (f) Repetition of π rotations in the bright transition, where precise π rotations freeze qubit B population at the fifty-fifty state, while over and under rotations move population up and down with respect to the fifty-fifty state. (g) Comparison of the cases with and without a pulse phase offset between single qubit π gates and CR pulses in order to compensate the latitude axis misalignment. The light (dark) color represents the case with a $X_{-\pi/2}$ ($X_{\pi/2}$) at the end. When the rotation axes are well aligned, the oscillations slow down without overlapping. (h),(i) Traces with different number of CR pulse repetition to extract single-qubit phase accumulation for qubit A, qubit B, respectively. When the phases are well compensated, the cosine functions move back to the case of zero CR pulse repetition which has no offset.

while sweeping ϵ_A. Fig. 4.7(c) shows the calibration results and the case with the ϵ_A error.

Starting from this paragraph, we conduct fine-tuning experiments for target parameters using a large varying number of CR pulses n to amplify the target error for precise calibration. For each target parameter, we start with a small n, compensate the corresponding error, increase n, compensate the error again, and repeat this cycle until n reaches a few hundreds.

We start with arg(η) and $|\eta|$ for achieving darkening condition using the sequence shown in Fig. 4.6(d). The $X_{\pi/2}$ pulse at the beginning moves qubit B to superposition state to increase the signal sensitivity to any unwanted rotation with respect to X axis. We iterate through the sweeping of $|\eta|$ and arg(η) to get the precise values after confirming no unwanted rotation is observed. Fig. 4.7(d) shows the data of $|\eta|$ and arg(η) sweeping. The two kinds of oscillations observed while sweeping $|\eta|$ and arg(η) can be understood as detuned X and Y rotations, respectively, where the detuning comes from the Stark shift or other second order effects on the dark transition. This detuning is much larger than rabi frequency, making the rotation rate approximately the same as detuning. Thus the rotation angle after one pulse is the same as the phase accumulated, agreeing well with the measured value of θ_B. Note that the error amplification of the unwanted dark transition rotation angle is limited by this small detuning. That is, further increasing the number of repetition pulse can not further amplify the error and give higher accuracy of the target parameters. Accordingly, we simply increase the average number of each measurement, making this calibration the most time consuming step compared with the other target parameters. We do supplementary check to make sure there's also no unwanted rotation with respect to Y axis by changing the $X_{\pi/2}$ at the beginning to $Y_{\pi/2}$.

Alternate pulse train experiments as shown in Fig. 4.6(e) amplify the error coming from drive frequency detuning. The trajectory leaves the big circle on the Bloch sphere due to the tilted rotation axis and gets further away if alternating the pulse phases with π difference. Thus, parameters such as f_d and DRAG coefficient which is also known as dynamical frequency tuning [72, 73] can be optimized using this experiments. Here we only sweep and optimize DRAG coefficient for simplicity as shown in Fig. 4.7(e). Slightly detuned drive frequency f_d with another well optimized DRAG coefficient can be a new pair giving you a big circle trajectory and even a higher gate fidelity. In this paper, we do not find another error syndrome to optimize f_d. Changing f_d of our CR pulse involves the optimization or correction for single qubit gates, making the tune-up process complicated. Instead, we make f_d on resonant with the bright transition to simplify the tune-up procedures.

Next, we sweep ϵ_A to achieve precise π rotation for the bright transition using Fig. 4.6(f). The $X_{\pi/2}$ pulse again aim to increase the sensitivity to errors. Fig. 4.7(f) shows the result after calibration and the symptom of over and under rotation. The signals of the even and odd number of pulses jump back and forth with respect to the initial value indicating the rotation angle is off from π. One can also sweep pulse width instead of ϵ_A for shorter gate times as we did for our 48.6 ns CX_π, especially when the microwave components respond nonlinearly to the setted amplitude values. For example, the saturation of IQ mixer under high power could change $|\eta|$ after tuning ϵ_A and thus break the darkening condition.

In reality, adjusting one of η, DRAG coefficient, and ϵ_A may change the optimal values of the others, thus one can iterate through Fig. 4.6(d),(e),(f) for higher accuracy. In practice, we calibrate these three target parameters seperately for only a few times and find that the previous values almost don't change after tuning the latter ones. However, we still carefully design the fine-tuning order of these three parameters to minimize the gate error as discussed below. In theory, the darkening condition can be achieved with accurate η and is independent of DRAG coefficient and ϵ_A, so we choose η as the first fine-tuned parameter. Next, adjusting one of DRAG and ϵ_A slightly change the other one corresponding to a π rotation. We select DRAG to tune first because the gate error due to non-optimal DRAG is very small compared with the other two parameters, coming from our calculation based on measured data. For example, a 93 ns CX_π pulse without DRAG has 50 kHz drive frequency detuning from the frequency corresponding to a rotation axis on the equator, resulting in gate errors on the order of 10^{-5} from the tilted rotation axis. We also find the optimal DRAG coefficient has magnitude of 1 ns, and the change of this DRAG after tuning other parameters is less than 0.1 ns. Even though we do not iterate back to tune DRAG again, this tiny change only induce additional error much lower than 10^{-5}. We thus only calibrate DRAG once and then iterate through ϵ_A and η calibration once as shown in Fig. 4.6(j), where we slightly tune η and ϵ_A if necessary. This routine is accurate enough and much faster than simultaneously performing a three-dimensional calibration.

We next tune ϕ, the last pulse parameter of our CR pulse, giving a pulse phase offset compared with the single-qubit gates of qubit B. Fig. 4.6(g) considers the rotation axis misalignment between single-qubit gates and our CR pulse. This pulse sequence is sensitive to latitude misalignment, for which we can tune the CR pulse phase to compensate. The corresponding syndrome for latitude misalignment is two overlapped and swapping oscillations shown in Fig. 4.7(g), which are for the two cases with $X_{\pi/2}$ or $-X_{\pi/2}$ at the end of the pulse sequence. Note that the signal due to longitude misalignment error is removed by the $X_{\pi/2}$ at the end but can still show up if there's over or under rotation angle off from π. The corresponding syndrome when there's no latitude misalignment is these two oscillations becoming seperate without overlapping each other. We often see this feature of longitude misalignment along with over/under rotation error due to either CR pulses or single qubit π gates while tuning up ϕ despite the fact that our CR rotation axis is already on the equator. The reason is that single qubit gate rotation axis is usually a little off from the equator which will be discussed later in Section 4.2.2.2. The over/under rotation probably comes from the incomplete calibration of the CR pulse or single qubit gate rotation angle. Despite the error coming from single qubit gates, we are still able to calibrate the latitude misalignment by making sure the two oscillation patterns do not overlap.

The final step is calibrating θ_A, θ_B using Fig. 4.6(h), (i), respectively, where we sweep the pulse phase θ of the $\pi/2$ gate at the end. We extract θ_A and θ_B by fitting the data in Fig. 4.7(h), (i) to a cosine function with phase offset. Note that the accumulated phase on the control qubit have additional $\pi/2$ from the nature of control rotation governed by system Hamiltoniuan. We exclude this contribution and compare the phase accumulation of different CX_π gate times, which are inversely proportional to the gate times agreeing with the Stark shift and second order effect. We then compensate θ_A and θ_B as mentioned earlier and measured the same experiments again to ensure no phase accumulation is observed. Note that the order of tuning Fig. 4.6(g) and Fig. 4.6(h),(i) is important, because the extraction and compensation of θ_A and θ_B we mentioned assume that the CR pulse is already a well tuned X rotation. Taking the ϕ we measured for example, the CR gate gets additional 2×10^{-5} error if the order is flipped.

The graphical flow chart in Fig. 4.6(j) summarizes the full calibration process.

$ZX_{-\pi/2}$ ***gate:***

For our $ZX_{-\pi/2}$ experiments, qubit A and B are the target and control qubits, respectively, with the CR drive $\hat{n}_B$ at the frequency f_{10}^A. The calibration follows the tune-up procedures of CX_π tuning the same eight parameters, the only difference is that the goals of some target parameters change. We again list all the fine-tuned parameters of our $ZX_{-\pi/2}$ pulse and the corresponding goals as below: the relative phase of the two port drives making sure they are in-phase by checking the selectively darkening condition of the $|00\rangle$-$|10\rangle$ transition, the relative amplitude of the two port drives to induce the same rotation speed but opposite rotation direction for the two target qubit transitions, the DRAG coefficient with fixed drive frequency to achieve a big circle trajectory on the Bloch sphere, the overall drive amplitude to ensure a $\pi/2$ rotation angle, the common pulse phase to align the rotation axis to X rotation, and the single-qubit phase accumulation of A and B due to the CR pulse to determine the phase values of virtual Z compensation. Here we only compensate the phase accumulation θ_c on the control qubit transitions because the two target qubit transitions are under rotation, and thus we observe no phase accumulated. Table. 4.2 indicates the Stark shifts of the two control qubit transitions are the same. Therefore, we found that applying one virtual Z gate with θ_c phase on qubit B is enough to take care of the accumulated single-qubit phases.

4.2.2.2 Tune-ups of single-qubit gates

Fig. 4.8 illustrates the calibration of our single-qubit gates with an offset cosine pulse shape without flattop. The target parameters are all the same as the CX_π case except ϕ. We first determine the sub-precise f_d by spectroscopy as shown in Fig. 4.8(a). We next aim at arg(η) because we need simultaneous two port drives to compensate classical crosstalks. Selective darkening requires accurate η, and we thus determine arg(η) by satisfying the darkening condition as shown in Fig. 4.8(b). Fig. 4.8(c) determines the sub-precise values of $|\eta|$ and ϵ_A. Next, we determine the f_d for qubit A and B by Ramsey measurements, making them on resonant with $|00\rangle - |10\rangle$ and $|00\rangle - |01\rangle$ as shown in Fig. 4.8(d). We perform the same tune-up sequences as CX_π to fine tune the DRAG, $|\eta|$, and ϵ_A as illustrated in Fig. 4.8(e),(f),(g). We last measured the accumulated

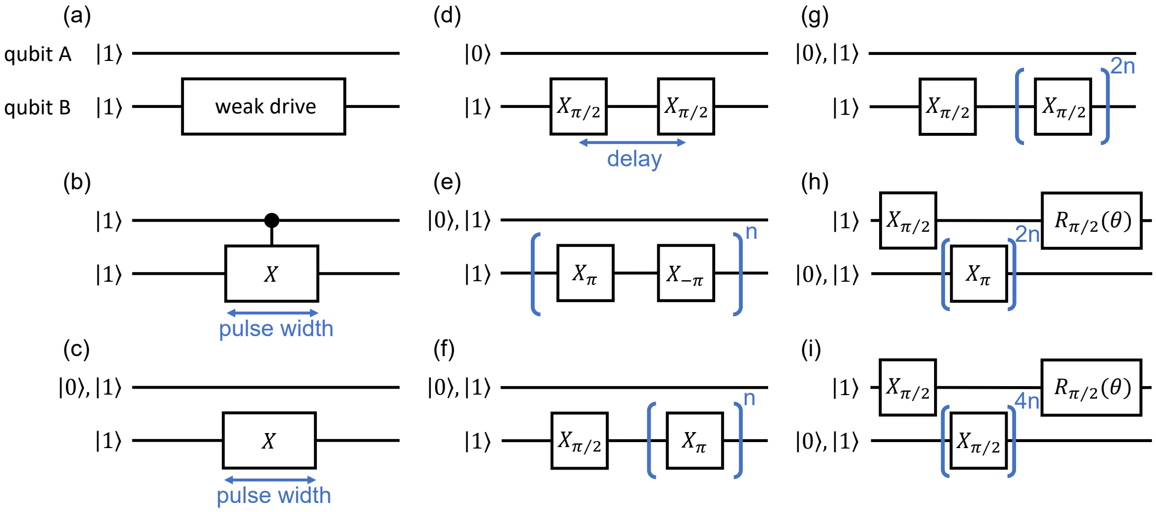

Figure 4.8: Single-qubit X_π and $X_{\pi/2}$ tune up procedures, showing pulse sequences for calibrating qubit B. Calibration for qubit A follows the same sequences with qubit A and B exchanged. (a) Measuring low power spectroscopy of the qubit transitions for drive frequency. (b) Sweeping the relative amplitude and phase of the two drives to achieve darkening condition, determining the relative drive phase needed for the compensation drive on the other qubit. (c) Rabi oscillation experiments. First we calibrate the relative amplitude of the two drives to synchronize the two Rabi rates conditional on the other qubit. Then we sweep the overall amplitude and determine X_π pulse width. (d) Ramsey experiments to determine the precise drive frequency. (e)-(i) Fine tuning with a large varying number of X_π or $X_{\pi/2}$ pulses to amplify the errors for precise calibration. (e) DRAG calibration by repeating X_π pulses with alternating amplitude, making rotation trajectories close to the big circle on Bloch sphere. (f),(g) Calibrating the overall and relative drive amplitudes for X_π, $X_{\pi/2}$, respectively, making sure there is no over or under rotations. (h),(i) Measuring the accumulated phases coming from the Stark shifts of qubit A due to X_π, $X_{\pi/2}$ of qubit B, respectively.

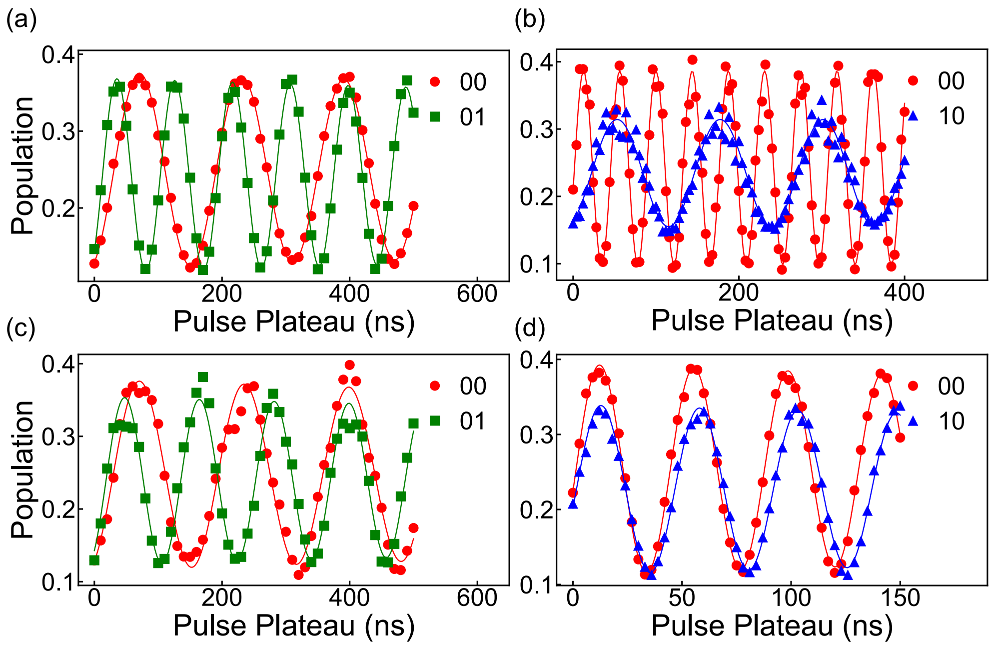

Figure 4.9: Rabi oscillation measurements to characterize classical crosstalks. The corresponding port, target qubit frequency, measured Rabi rate, and the calculated η are listed below: (a) Port A, f_{01}^{A}: $\Omega_{00-10} = 6.24$ MHz, $\Omega_{01-11} = 11.05$ MHz, $\eta_A = 0.7$ (b) Port A, f_{01}^{B}: $\Omega_{00-01} = 22.88$ MHz, $\Omega_{10-11} = 8.05$ MHz. $\eta_A = 0.69$ (c) Port B, f_{01}^{A}: $\Omega_{00-10} = 6.14$ MHz, $\Omega_{01-11} = 8.57$ MHz. $\eta_B = 14.99$ (d) Port B, f_{01}^{B}: $\Omega_{00-01} = 23.20$ MHz, $\Omega_{10-11} = 22.20$ MHz. $\eta_B = 14.83$

phase due to Stark shifts utilizing the sequences in Fig. 4.8(h),(i).

As shown in Fig. 4.8, we need to optimize $|\eta|$ and ϵ_A individually for X_π and $X_{\pi/2}$ instead of setting ϵ_A directly to half because of the saturation of IQ mixer where we observe nonlinear amplitude response while tuning the drive amplitude. Note that applying virtual Z compensation for the phases in Fig. 4.8(h),(i) cannot change the results of individual RB but affect the outcome of simultaneous RB. One needs to check single-qubit Clifford decomposition to determine if applying this phase compensation is helpful.

4.2.2.3 Calibration of classical crosstalks

Note that in a realistic system, each drive from the two ports influences both qubits. Consequently, $|\eta|$ is not merely the ratio of the two drive amplitudes we apply for the two ports.

Driven at	f_{01}^A	f_{01}^B
η_A	0.70	0.69
η_B	14.99	14.83

Table 4.4: The calculated values of η_A and η_B from Fig. 4.9.

Nonetheless, we can still adjust the ratio of these two amplitudes to construct any combination of ϵ_A and ϵ_B we need. To characterize this classical crosstalk effect, we define η_A and η_B as the $|\eta|$ while individually driving port A and B, respectively. In Fig. 4.9, We drive each port solely and measure Rabi rates to extract η_A and η_B at the frequency f_{01}^A and f_{01}^B. Taking Fig. 4.9(a) for example, we drive port A at the frequency f_{01}^A and measure the Rabi frequency Ω_{00-10} and Ω_{01-11} of the transition $|00\rangle - |10\rangle$ and $|01\rangle - |11\rangle$, respectively. Following the expression of Eq. 4.12, we know

$$\frac{\Omega_{00-10}}{\Omega_{01-11}} = \frac{\langle 00|\hat{n}_A|10\rangle + \eta_A\langle 00|\hat{n}_B|10\rangle}{\langle 01|\hat{n}_A|11\rangle + \eta_A\langle 01|\hat{n}_B|11\rangle}. \tag{4.15}$$

Incorporating with Table 4.2, we can calculate the value of η_A for the frequency f_{01}^A. Similarly, we can also drive port A at the frequency f_{01}^B, port B at f_{01}^A, and port B at f_{01}^B with corresponding results shown in Fig. 4.9(b),(c), and (d), respectively. Table 4.4 concludes the values of η_A and η_B.

4.2.3 Gate characterization

4.2.3.1 RB measurements for single-qubit gates

The measured single-qubit Clifford-gate fidelities, F_I and F_s, extracted from individual and simultaneous randomized benchmarking (RB) discussed in Appendix A.4 for each qubit

Table 4.5: Fluxonium qubit parameters and performance. α represents anharmonicity. F_I and F_s are the average fidelities per Clifford gate extracted from individual and simultaneous randomized benchmarking, respectively.

	Qubit A	Qubit B
f_{01}(GHz)	0.15	0.23
α (GHz)	4.51	4.54
ξ_{ZZ}^{static}(MHz)	0.002	
$T_1(\mu s)$	260	160
$T_2^*(\mu s)$	100	110
$T_2^E(\mu s)$	200	150
$F_I(\%)$	99.976	99.96
$F_S(\%)$	99.93	99.913

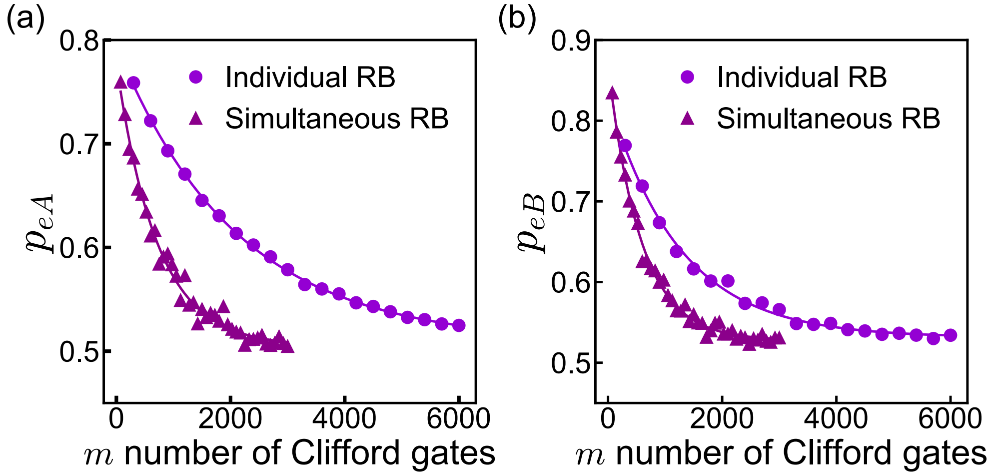

Figure 4.10: Single-qubit gate RB. (a), (b) Individual and simultaneous RB for qubit A, B, respectively.

are presented in Table 4.5, which summarizes the key parameters of our fluxonium qubits. Our decomposition of the single-qubit Clifford group utilizes virtual Z gates, which perform frame updates and change the phase of subsequent X and Y pulses, following the representation described in [32]. Fig. 4.10 shows the results of individual and simultaneous RB for our 61 ns (64 ns) A (B) single-qubit gates.

4.2.3.2 RB measurements for two-qubit cross-resonance gates

We perform interleaved randomized benchmarking (IRB) [83] discussed in Appendix A.4 to characterize our CR gates with an offset cosine pulse shape without flattop. We focus more on the characterization of CX_π in this section.

CX_π gate:

Figure 4.11(a) shows the results of 100 randomized gate sequences for a 60 ns CX_π gate with the extracted infidelity of 6×10^{-4}, along with two other different gate times all reaching fidelity higher than 99.9%. To better characterize the stability of gates, we increase the number of CX_π gates interleaved n up to 10 to amplify the error. Fig. 4.11(b) shows the IRB traces of the $n = 10$ case for example. The corresponding infidelity is much larger than the error bar, enabling us to monitor the gate performance over time without ambiguity, as shown in the next paragraph. We plot the fidelities versus n for the 60 ns idling identity and CX_π gates in Fig. 4.11(c) and extract the fidelity of the identity gate through linear fit.

In Fig. 4.12(a), we showcase all the IRB measurements spanning over three weeks without any recalibration interleaved to demonstrate the stability of our device. We simply let a measurement computer repeatedly recall the same configuration files to perform the same IRB with all parameters being the same. By interleaving CX_π gate IRB with identity gate IRB as shown in the inset of Fig. 4.12(a), we demonstrate that our CX_π is mostly limited by incoherent errors. The two gate fidelities are measured alternately on the time scale of days, providing statistics that minimize the effect of coherence time fluctuation. The difference between the two fidelities points out that the additional errors are on the order of 2×10^{-4}, setting a upper bound for coherent errors. In Fig. 4.12(b), 6 sets of IRB measurements for 60 ns CX_π versus n are presented

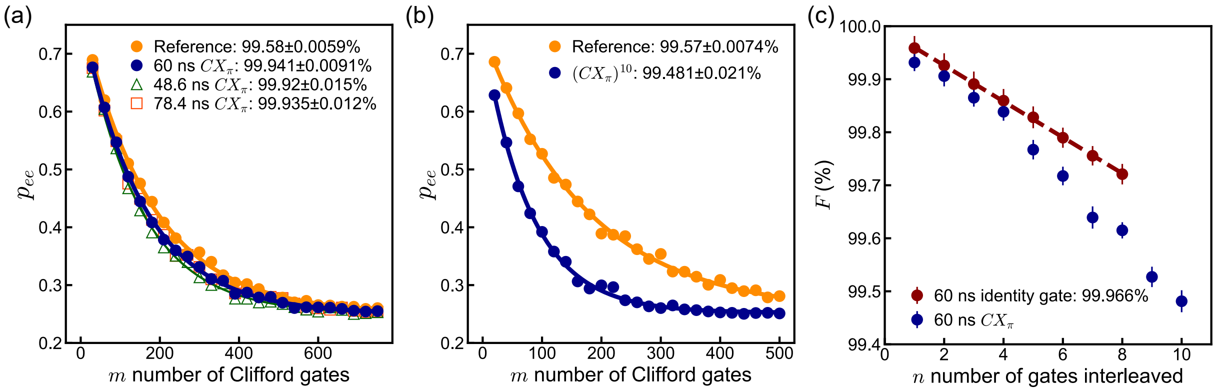

Figure 4.11: IRB results. (a), (b) IRB of the 60 ns CX_π with $n = 1, 10$, respectively. The results of different gate times are also provided in (a). We construct the two-qubit Clifford group with, on average, 4.5 physical single-qubit gates (incorporating virtual Z gates) and 1.5 CX_π gates per Clifford gate. The reference error per two-qubit Clifford extracted from the standard RB is consistent with the average number of gates and the corresponding gate infidelity. (c) Fidelities of CX_π and idling identity gates with different n. Here, we show the fidelity number extracted from the linear fit for the 60 ns identity gate.

together, giving the information of repeatability within 20 days and the possible reasons for the fidelity fluctuation as discussed in the caption.

$ZX_{-\pi/2}$ gate:

Fig. 4.13 characterizes the fidelity and stability of our 89 ns $ZX_{-\pi/2}$. The data points measured on day 2 average over more randomized sequences and thus have longer measurement time and smaller error bars. We preserve the 99.9% fidelity across 3 days without recalibration interleaved.

4.2.4 Error budget

4.2.4.1 Simulation methods for error budget

To assess the sources of coherent error in the selective-darkening gate, we perform simulations where the applied drive implements a π-rotation between the $|00\rangle$ and $|01\rangle$ states (the

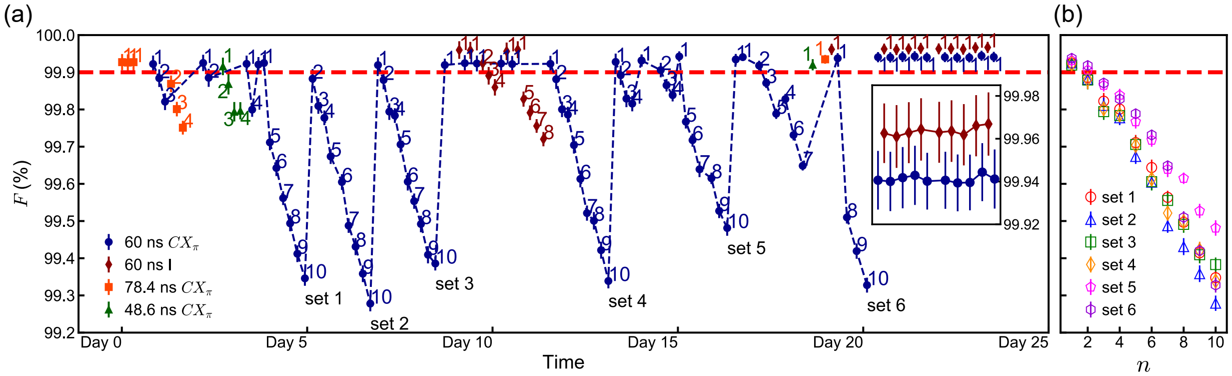

Figure 4.12: IRB measurements spanning over 3 weeks without any recalibration, demonstrating the stability of CX_π gates. (a) All measured IRB fidelities with an auxiliary line indicating 99.9%. The numbers next to the data points represent the number of interleaved CX_π gate n. Our fridge warmed up due to a power outage on Day 25, which ended the measurement. The inset zooms in the result of interleaving CX_π IRB with idling identity gate IRB from Day 20 to Day 25. The CX_π and identity gates have average fidelity above 99.94% and 99.96%, respectively. This difference of 2×10^{-4} sets the upper bound for coherent errors. (b) Comparison of all 6 sets of fidelities versus n. The fifth set reaches the highest fidelities, coming from a gradual change near Day 15. Starting from the eighth data point of set 6, fidelities drop back to the values of the previous sets, happening right after the reboot of arbitrary waveform generator (AWG). Thus the fluctuation of fidelities may relate to the instability of AWG.

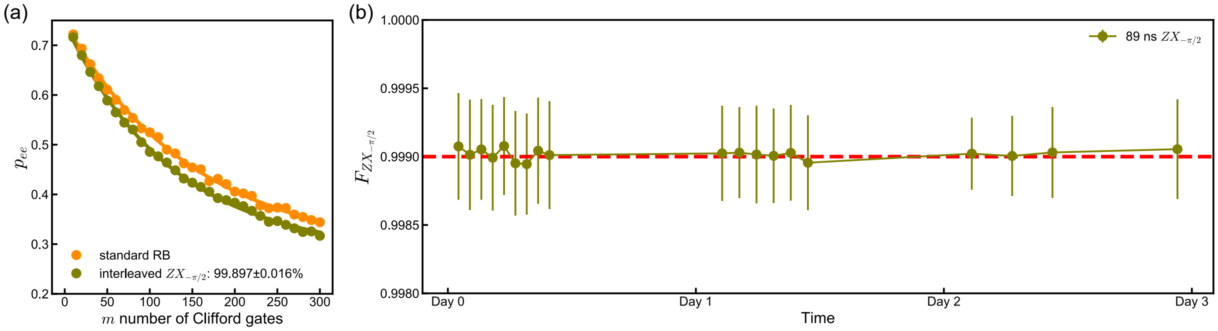

Figure 4.13: $ZX_{-\pi/2}$ IRB results. (a) IRB traces presented with the extracted gate fidelity. (b) Stability demonstration across 3 days.

bright transition), while leaving the $|10\rangle \leftrightarrow |11\rangle$ subspace unaffected (the dark transition). The time evolution operator of the driven system is computed using the QuTiP package [76, 77], and subsequently projected onto the 4×4 computational subspace to obtain the simulated evolution matrix $\hat{U}_{\text{sim}}$. We then evaluate the fidelity of this operation with respect to the ideal CX_π gate $\hat{U}_{\text{ideal}}$ (4.14) using the standard gate fidelity expression [106]

$$F = \frac{\mathrm{Tr}\left(\hat{U}^\dagger_{\text{sim}}\hat{U}_{\text{sim}}\right) + \left|\mathrm{Tr}\left[\hat{U}_{\text{ideal}}\hat{U}_{\text{sim}}\right]\right|^2}{20} \,. \tag{4.16}$$

The infidelity of the CNOT gate can be decomposed into different error types as [86]

$$1 - F = \mathcal{E}^0_{\text{ctrl}} + \mathcal{E}^1_{\text{ctrl}} + \mathcal{E}_{\text{dark}} + \mathcal{E}_{\text{bright}} + \mathcal{E}_{\text{leak}} \,. \tag{4.17}$$

Here, we categorize the gate error into five contributions:

- $\mathcal{E}^0_{\text{ctrl}} = (P_{00\to10} + P_{10\to00} + P_{01\to10} + P_{10\to01})/5$, the probability of control qubit flip with respect to the expected final state when target qubit is in state $|0\rangle$;
- $\mathcal{E}^1_{\text{ctrl}} = (P_{01\to11} + P_{11\to01} + P_{00\to11} + P_{11\to00})/5$, the probability of control qubit flip with respect to the expected final state when target qubit is in state $|1\rangle$;
- $\mathcal{E}_{\text{dark}} = (P_{10\to11} + P_{11\to10})/5$, the probability of the unwanted excitation for dark transition $|10\rangle \leftrightarrow |11\rangle$;
- $\mathcal{E}_{\text{bright}} = (P_{00\to00} + P_{01\to01})/5$, the probability of imperfect Rabi flip between the bright states $|00\rangle \leftrightarrow |01\rangle$;
- $\mathcal{E}_{\text{leak}} = 1 - \mathrm{Tr}\{\hat{U}^\dagger_{\text{sim}}\hat{U}_{\text{sim}}\}/4$, the leakage probability outside the computational subspace.

The five error probabilities are determined by the matrix elements of the simulated evolution operator $\hat{U}_{\text{sim}}$:

$$P_{ab\to a'b'} = |\langle ab|\,\hat{U}_{\text{sim}}\,|a'b'\rangle|^2 \tag{4.18}$$

We group the four error probabilities $P_{00\to10}$, $P_{10\to00}$, $P_{01\to10}$, $P_{10\to01}$ into $\mathcal{E}^0_{\text{ctrl}}$ as the differences among these values are observed to be less than 10% of their magnitudes. The $|00\rangle \to |10\rangle$ and $|10\rangle \to |00\rangle$ process are symmetric and therefore expected to occur with nearly identical probabilities. The $|01\rangle \leftrightarrow |10\rangle$ transition can be interpreted as a combination of a control qubit flip $|00\rangle \leftrightarrow |10\rangle$ and the bright transition flip $|01\rangle \leftrightarrow |00\rangle$. Since the bright transition flip probability is close to 1 under well-calibrated drives, the overall probability of swapping the transition $|01\rangle \leftrightarrow |10\rangle$ is primarily determined by the probability of control qubit flip $|00\rangle \leftrightarrow |10\rangle$, making it close to $P_{00\to10}$ and $P_{10\to00}$ numerically. The same reason applies to $P_{01\to11}$, $P_{11\to01}$, $P_{00\to11}$, $P_{11\to00}$, which are grouped into $\mathcal{E}^1_{\text{ctrl}}$. The pulse optimization process in the simulations follows the experimental calibration procedures, with further details provided in [3].

Our model includes two qubits and two resonator modes, each requiring a truncated Hilbert space of at least dimension 5 to ensure numerical accuracy. This makes numerically solving the master equation for decoherence computationally demanding. However, since the gate durations are approximately three orders of magnitude shorter than the coherence times, we estimate the incoherent error contributions using a first-order analytical expression instead [79, 80]:

$$\Delta F_{\text{incoherent}} \simeq \frac{1}{5}\frac{t_{\text{gate}}}{T_{1,A}} + \frac{1}{5}\frac{t_{\text{gate}}}{T_{1,B}} + \frac{2}{5}\frac{t_{\text{gate}}}{T^E_{2,A}} + \frac{2}{5}\frac{t_{\text{gate}}}{T^E_{2,B}}. \tag{4.19}$$

Here t_{gate} is the gate time of the CX_π gate, and the applied T_1 and T^E_2 values are from Table 4.5.

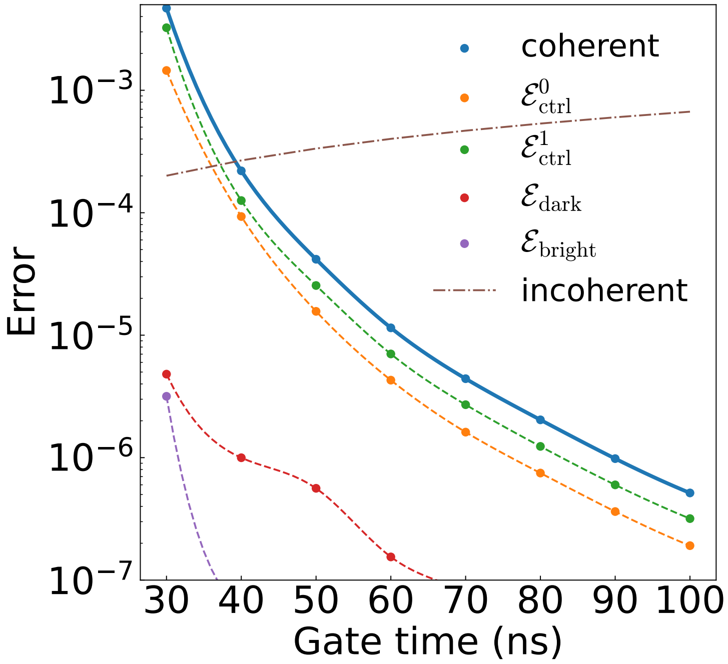

Figure 4.14: Error budget of the CX_π gate for different gate times. The solid line is the coherent error of the optimized gate. The dashed lines are the decomposition of the coherent error into different error channels. The errors, $\mathcal{E}^0_{\text{ctrl}}$ ($\mathcal{E}^1_{\text{ctrl}}$), $\mathcal{E}_{\text{dark}}$, and $\mathcal{E}_{\text{bright}}$, represent the unwanted excitation of the control qubit transition when target qubit is in state $|0\rangle$ ($|1\rangle$), the dark transition, and the bright transition, respectively. These values are determined by the matrix elements of the simulated evolution operator. The dotted-dashed line is the analytical estimation of the incoherent error using Eq. 4.19.

4.2.4.2 Simulation results of error budget

To investigate the infidelity of the CX_π gates on our device, we run simulations evaluating the sources of coherent errors for different gate times as shown in Fig. 4.14. While it is preferred to have as short a gate time as possible to reduce the effect of decoherence, as shorter gate time requires a stronger drive, there is a lower bound on the gate time due to control errors. In our case, the dominating error originates from control qubit flips that happen even though the drive frequency is detuned from the control qubit frequency. This unwanted excitation comes from diabatic process, as discussed in Section 2.6.1.3. Such a control qubit flip error dominates the coherent error of our simulated gate, reaching 10^{-5} with a gate time of 60 ns. The error can further exceed 10^{-3} by shortening the gate below 30 ns. The other coherent errors, including the bright and dark transition errors and the leakage error, have a negligible contribution to the total gate error. In particular, the leakage error is well below 10^{-7} for all these gate times and thus not present in the figure. The negligible leakage comes from the strong anharmonicity of fluxonium, suppressing leakage out of computational subspace during the drive. The difference between the simulated 10^{-5} coherent error and the measured upper bound of 2×10^{-4} for coherent errors is probably due to the drive envelope delay coming from the cable length difference between the two port drives. The cable length difference between our two port drives is a few tens of centimeters, inducing the drive envelope delay of a few nanoseconds. We do not calibrate against this delay in our experiments, so we further simulate this effect for our 60 ns CX_{π} as shown in Fig. 4.15. We sweep the delay up to 5 ns and observe a significant rise of the dark transition error to the order of 10^{-4}. This agrees with the measured upper bound of 2×10^{-4} for coherent errors. The bright transition error can also go above 10^{-5}, while the control qubit flip and leakage errors are still well below 10^{-5} under this effect and are not shown in Fig. 4.15. This shows the importance of synchronizing drive envelopes especially for coherent errors below 10^{-4}. Such errors could be mitigated by calibrating the envelope delay through sweeping the delay between two non-commuting pulses applied at the two ports, respectively, or improving microwave engineering to equalize the cable length in future experiments.

We next simulate single-qubit X gates to investigate the additional error sources of simultaneous single-qubit gates compared with individual single-qubit gates. The lowest simulated coherent errors of the individual X gate on qubit A, the individual X gate on qubit B, and the simultaneous X gates on both qubits are 8×10^{-5}, 8×10^{-6}, and 6×10^{-4}, respectively. For

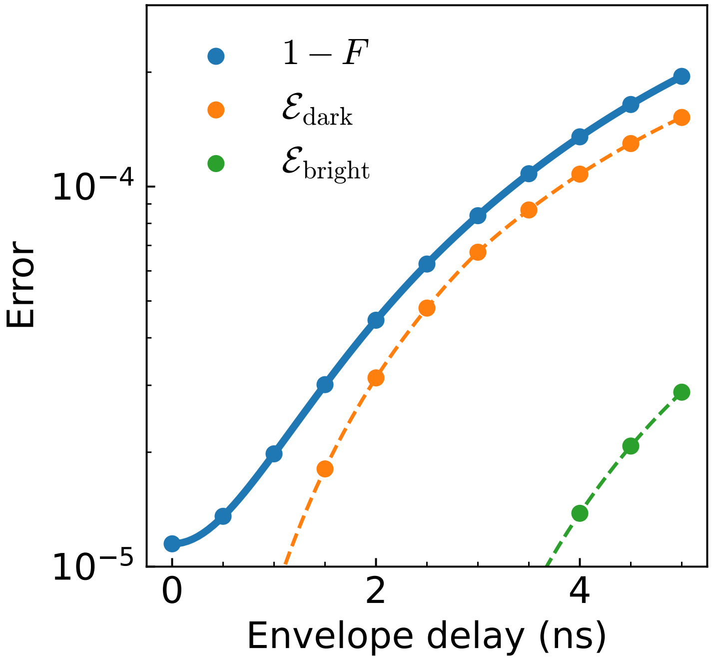

Figure 4.15: Error budget of 60 ns CX_π gate for different drive envelope delay. The solid line is the coherent error of the optimized gate. The dashed lines are the decomposition of the coherent error into different error channels.

comparison, we estimate the coherent error upper bounds based on the RB measurements in Section 4.2.3.1 and the estimated incoherent errors following [80]. The coherent error upper bounds are 1×10^{-4}, 2×10^{-4}, and 8×10^{-4} for the individual gate on qubit A, the individual gate on qubit B, and the simultaneous gate pair, respectively. Note that these bounds are estimated for the average errors of the whole single-qubit Clifford group. The estimated errors agrees well with the bounds, and we suspect that the relatively large difference between the estimated values based on experimental data and the simulated values of the individual X gate on qubit B comes from improper calibration and the swap errors observed while tuning up. Following the experiments, we don't optimize the drive frequencies of individual gates for the simulated values above, while the errors of the individual X gate on qubit A and the simultaneous X gate pair can be lowered down to 1×10^{-5} and 4×10^{-4}, respectively, by doing so. In addition, we only optimize the

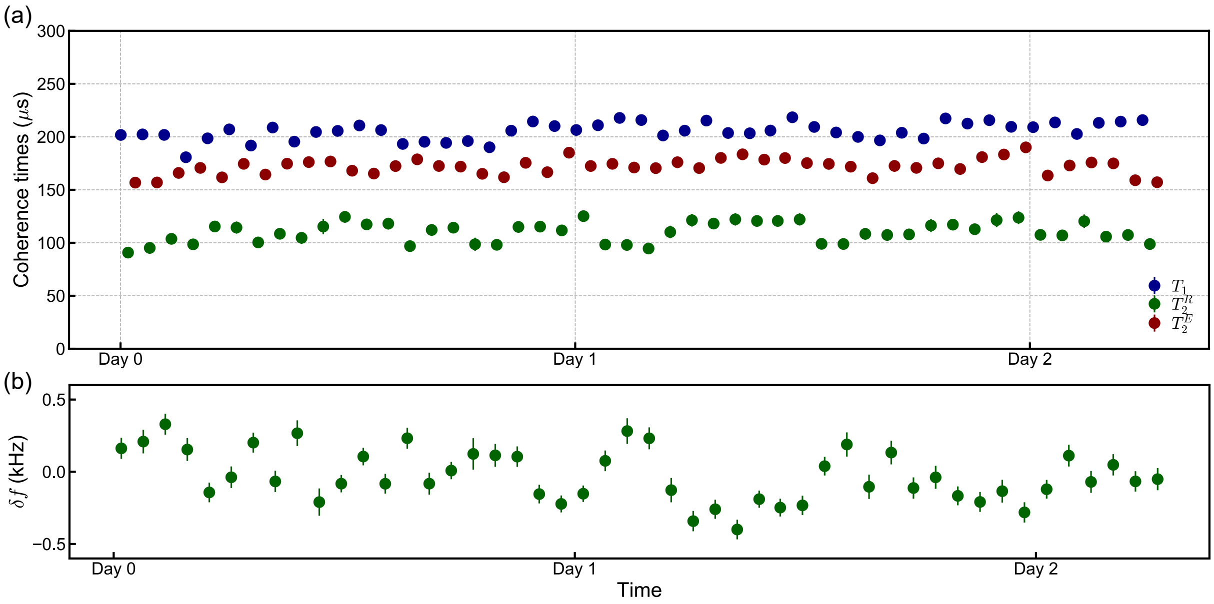

Figure 4.16: Stability characterization of qubit B frequency and coherence times for over two days. (a) Coherence times interleaved with each other. (b) The fluctuation of qubit frequency extracted from the Ramsey measurements in (a).

individual X gates and directly apply both simultaneously to achieve the simultaneous X gate pair above. If we further optimize the two drive frequencies of the X gate pair, the simulated error can be suppressed to 7×10^{-5}, indicating that there's still room to improve single-qubit gates. The difference between the optimized drive frequencies of the individual X gates and the simultaneous X gate pair is above 100 kHz, agreeing with an error over 10^{-4} due to detuning. We interpret this behavior as an indicator that the induced Stark shifts contribute significantly to the coherent error of simultaneous gates. Larger qubit-qubit detuning in future devices can mitigate this effect and the swap error while driving two qubits simultaneously.

4.2.5 Metrics supporting the high gate stability

In this section, we present the stability characterization of the metrics other than RB such as flux biases, qubit frequencies, and coherence times. The current biases of the two coils are 1.68 mA and 1.979 mA for all the measurements, calibrated three months earlier than the beginning of the 24-day RB measurements. We checked these current biases every two weeks to make sure that the half-flux sweet spots of the two qubits are always matched. The coherence time measurements of qubit B are shown in Fig. 4.16, where we monitored T_1, Ramsey decay time T_2^R, echo decay time T_2^E, and qubit frequency for over two days prior to the RB measurements. The qubit frequency $f_{01}^B + \delta f$ is extracted from the Ramsey measurements in Fig. 4.16(a) with the fluctuation δf smaller than 1 kHz as shown in Fig. 4.16(b). Here we measure the averaged demodulated signal without performing single shot measurements in order to extract one set of T_1 and T_2 values every one hour. This method takes much longer time for qubit A because of its smaller dispersive shift and the geometry of Fig. A.3(a), and thus we only measured one set of coherence times for qubit A using single shot readout before the RB measurements. All the coherence times and qubit frequency of both qubits discussed above agree well with the values provided in table 4.5 that were measured on Day 15 of Fig. 4.12(a). Using Equation 4.19, the estimated fidelity variation between the worst and best coherence time cases is 0.005%. For qubit frequency fluctuation, the simulated gate fidelity difference due to 1 kHz detuning is lower than 10^{-7}. These values agree with the observed fidelity fluctuations from Fig. 4.12.

4.3 Discussion

Two recent experiments have benchmarked entangling gates based on inductively coupled fluxoniums [34, 37], utilizing flux drives for gate operations. The first report [37] performs rf dynamical decoupling drive to counter the dephasing due to flux noise and improve coherence times with an order of magnitude, achieving 20 ns fast gates but still with a coherence time drop when the flux drive is applied. The fluxonium qubits of the latter work [34] are coupled through a tunable coupler, consisting of a static harmonic mode and a flux-tunable fluxonium-like mode. In comparison, our scheme does not rely on fast flux modulation which eliminates a channel for decoherence.

Nearly complete suppression of quantum cross-talk by inductive coupling (illustrated by the nearly zero matrix elements in Table 1) leads to three orders smaller static ZZ accumulation rate in comparison to the first demonstration of the CR gate on capacitvely-coupled fluxoniums [38], along with an order of magnitude suppression of the total gate error due to a higher (but far from record-high) coherence time (see Fig. 4.16). The freedom to choose a CX_π or a $ZX_{-\pi/2}$ gate manifests the versatility of the CR-gate family; the difference between these two options for our system can be briefly summarized as follows. The $ZX_{-\pi/2}$ is subject to additional coherent errors such as dynamical ZZ errors in comparison with the CX_π, for which we apply single-qubit virtual Z gates to compensate ZZ dynamics as illustrated in Section 4.2.2.1. On the other hand, the $ZX_{-\pi/2}$ of our system requires only a single local drive on the control qubit, reducing the technical complexity of gate operations.

We next discuss the discrepancy of individual and simultaneous single-qubit RB measurements. The resonant direct drive terms in Hamiltonian 4.7 defined by coefficients M^+_{AA} and M^+_{BB}

provide the leading contribution to single-qubit gates. The contribution from the non-resonant cross-drives is considered to be small. In fact, the 80 MHz qubit-qubit detuning $\delta = |f_{01}^{A} - f_{01}^{B}|$ is relatively close to the Rabi frequency $\propto 1/t_{gate}$, and the cross resonance coefficients M_{AB}^{-}, M_{BA}^{-} in Table 4.2 are only a few times smaller than the direct coefficients M_{AA}^{+} and M_{BB}^{+}. This indicates the contribution of cross-resonant terms in Hamiltonian 4.7 has to be taken into account. The corresponding Stark shifts further degrade the performance of simultaneous gates. To investigate this effect, we simulate the coherent errors of the individual X gates on each qubit and the simultaneous X gate pair on both qubits in Section 4.2.4, showing the Stark shift effect through the deviation of optimized drive frequency between individual and simultaneous gates and indicating the possible improvement through further drive frequency optimization of single-qubit gates.

The degradation of single-qubit gates due to stronger hybridization manifests another trade-off relation between single-qubit and two-qubit gates while tuning the qubit-qubit coupling strength J_L. Future devices with larger δ can mitigate this effect for the same Rabi frequency and, thus, the same gate time. Since the hybridization ratio is proportional to J_L/δ, the smaller ratio of cross resonance coefficients to direct coefficients (M_{AB}^{-}/M_{AA}^{+}, M_{BA}^{-}/M_{BB}^{+}) due to larger δ can be tuned back to the same ratio with stronger qubit-qubit coupling. In this case, we would get the same two-qubit gate speed and better performance of simultaneous single-qubit gates. The larger δ will also benefit the two-qubit CX_{π} gate by reducing the control qubit errors, allowing shorter gate times. Operating at a larger coupling J_L would increase the small residual static ZZ-term, which can be mitigated either by engineering the spectrum of non-computational transitions or adding an additional capacitive coupling J_C [68]. Another solution is keeping the coupling J_L relatively small but increasing δ along with the CR drive amplitude. Increasing both the frequency separation and the drive amplitude keeps the two-qubit gate time short but can suppress the control qubit flip error. To investigate this effect, we simulate the 60 ns CX_π gate with larger δ by tuning E_J to make qubit B (A) frequency 40 MHz higher (lower), achieving a 120 MHz frequency separation. The simulated total coherent error is 3×10^{-6} (2×10^{-6}) while the total control qubit flip error $\mathcal{E}^0_{\text{ctrl}} + \mathcal{E}^1_{\text{ctrl}}$ is around 1×10^{-6} for both cases. This is an order of magnitude smaller than the case of $\delta =$ 80 MHz, for which the fine tuning can only lower the error down to 1×10^{-5}. Thus, a larger qubit-qubit detuning δ enables better performance of single and two qubit gates and it is a promising strategy considering a relatively wide window of possible frequencies for high-coherence fluxoniums [11].

We finally comment on the scalability of direct inductive coupling. For scaling up, we can use stars of inductively coupled fluxoniums assisted by quasi-3D techniques such as air bridges and flip-chip design. The interactions between stars could be achieved through different mechanisms such as shared junctions or geometric mutual inductance. Local independent flux-bias lines with the characterization and mitigation of the corresponding multi-qubit crosstalk can be achieved following the previous work [107], which also gives a good example of the 2D layout. Gate schemes utilizing charge drives only require DC flux bias, for which the flux crosstalk is relatively easy to deal with. Combining flux lines with charge lines on a multi qubit chip has been achieved [108]. To reduce engineering complexity, inductively coupled 2D readout resonators can also help with the arrangement of charge lines and lowering the system size, which have already been experimentally demonstrated for fluxonium qubits [1]. The unwanted capacitive crosstalk could be suppressed by larger qubit-qubit distance and ground planes. While the scalability challenges are undeniable, our current two-qubit demonstration motivates further research into inductively-coupled qubit networks.

Chapter 5: Summary and Outlook

5.1 Summary

We have explored and operated a single integer fluxonium qubit in a zero magnetic field and in the frequency range typical for operating transmon qubits. It has a comparably high T_1 and gate fidelity, despite a much lower quality of the circuit dielectrics. The value of the corresponding sensitivity $\langle 0|\hat{n}|1\rangle$ can be controllably reduced by increasing the ratio E_J/E_C almost independent of the qubit frequency following Eq. 2.15. The only apparent catch of the IFQ design is the doublet nature of the excited state of the qubit, which may result in a leakage of quantum information outside the computational subspace. Nevertheless, we have experimentally demonstrated that even in a relatively extreme case of $\omega_{12}/2\pi$ = 11 MHz, the gate error remains below 0.1% with a gate time between 50 and 100 ns thanks to the parity selection rule at $\varphi_{\text{ext}} = 0$. The theoretical estimates of the leakage error are as low as 10^{-4} provided that the flux bias is stable to about $\delta\Phi_{\text{ext}}/\Phi_0 \approx 1 \times 10^{-5}$. The limits of the flux stability will be investigated in future work.

For our two-qubit device, we have implemented a system of two inductively coupled but capacitively driven fluxonium qubits. The device behaves as a nearly ideal transversely-coupled spin-1/2 system and is thus well suited for all-microwave fixed-frequency cross-resonance two-qubit gates [109, 110]. It is interesting to note that the values of the qubit frequencies f_{01}^A and f_{01}^B

are relatively far from each other than in transmon experiments, which provides more freedom in the choice of circuit parameters. The strength of ZX-interaction is proportional to $J_L/|f_{01}^A - f_{01}^B|$ just like in the case of purely two-level systems. The static ZZ-term is suppressed into the low-kHz range thanks to the combination of a large frequency detuning of the non-computational states and the property of the flux matrix elements in Fig. 4.3(b). Tuning the coupling capacitance can help suppress the ZZ -term to zero, but it also needs to consider the corresponding change of g_A, g_B, and f_{LC} of the stray LC-mode. This case would be a liability in terms of coherent and incoherent errors during gate operations. Although LC mode does not introduce significant detrimental effects in our current design, additional spurious LC modes could introduce unwanted interactions in multi-qubit architectures. These can be mitigated by ensuring sufficient detuning from qubit frequencies and small enough coupling constants to qubits, which can be achieved by minimizing the capacitive coupling between qubits. Since inductive coupling is preferred for qubit-qubit interactions, minimizing capacitive links aligns with the goal of reducing the unwanted coupling strength J_C. Another strategy to eliminate LC modes entirely is the implementation of geometric mutual inductance, which could be achieved by the assistance of air bridges or flip-chip designs.

For the implementation of our two-qubit gate, we achieved a 60 ns direct CX_π gate with a record high fidelity 99.94% in a pair of inductively-coupled fluxonium qubits, using a selective darkening/cross-resonance interaction scheme. In contrast to other experiments on superconducting circuits, the two-qubit dynamics in our device are nearly completely decoupled from the circuit's non-computational transitions, the qubits behave as a pair of transversely-coupled two-level systems. The gate fidelity exhibits an unprecedented level of stability, remaining beyond 99.9% for over 3 weeks without any recalibration. While there are some obvious experimental pre-requisites for observing such stability, such as stable flux bias, long coherence time, and phase-locking of microwave sources, our experiment contains no exceptions in this respect. Rather, we believe a further simplification of both the device circuit and the control procedures minimizes the number of error channels and results in the gate stability: our gate is implemented by sequentially tuning 8 weakly-coupled parameters, suppressing one error at a time. We stress that our smooth and simple pulses without precise shaping have not been optimized to prevent leakage outside the logical sub-space, which is automatically taken care of by the strong anharmonicity of our coupled two-qubit system, controlling the dynamics in the 4-state computational subspace.

5.2 Outlook

Although fluxonium is robust against leakage errors for single-qubit and two-qubit gate schemes within computational subspace thanks to its highly anharmonic spectrum, leakage during readout can be problematic. This is because its unique selection rule allows transitions between non-neighboring states, opening different channels and mechanisms for measurement induced state transition (MIST) compared to transmon [111, 112, 113]. Recent research regarding fluxonium readout still demonstrate the potential of high fidelity readout with proper qubit parameters and readout frequency placement near the 0-3 and 1-4 transitions [114], enabling fidelity close to 99.9% [115]. To counter MIST, several alternative readout schemes other than dispersive readout have been proposed for transmon [116, 117, 118, 119]. However, the underlying mechanism of MIST in fluxonium remains to be thoroughly investigated, as such understanding is crucial for developing effective mitigation strategies. In addition to MIST to higher energy levels, TLS can be a possible reason for MIST within computational subspace due to the Stark shift of qubit frequency [120], signifying the importance of addressing dielectric-related issues.

Fluxonium benefits from the reduced sensitivity to dielectric loss by lowering $\langle 0|\hat{n}|1\rangle$, and another question is whether we can improve the capacitor design and the quality of dielectrics to lower $\tan\delta_C$. The typical E_C of Fluxonium is larger than transmon, corresponding to a smaller qubit capacitance. The corresponding optimization of participation ratio for dielectric loss through diluting the electric field requires carefully considered capacitance budget including the distance and size of pads. The small qubit capacitance also results in extra constraint to achieve strong enough coupling strength to capacitively coupled readout resonators or neighboring qubits. Regarding the material aspect, Tantalum pads and pad etch process [121] do not improve fluxonium as much as they do for transmon, potentially attributed to the presence of the dielectric materials related to chain junctions, which do not present in transmon. Various alternatives for JJ arrays have been realized, including stacked JJs [122], spiral structures [123], van der Waals materials [124], and disordered superconductor materials [125]. However, their dominant loss channels distinct from those in the JJ arrays used in this thesis, such as quasi particles in granular aluminum [126] and defects in NbTiN [127], remain to be thoroughly investigated and mitigated. Understanding of the underlying loss mechanisms is the critical goal for optimizing performance.

Appendix A: Methods

A.1 Device Simulation and Design

We simulate the capacitive links in our device using the eigenmode solver of HFSS in ANSYS Electronics Desktop as shown in Fig. A.1. The capacitance C between different pads can be extracted by assigning linear inductance L between pads using a lumped sheet, and the solved eigenmode frequency $1/\sqrt{LC}$ gives the simulated value of C. To extract the capacitive coupling strength g between modes, taking the two qubit modes for example, one qubit's inductance is fixed to set ω_a, while the other is swept to vary ω_b. As ω_b approaches ω_a, an avoided crossing appears in the eigenmode spectrum. The minimal frequency splitting corresponds to $2g$. The same method also applies to the extraction of qubit-cavity coupling strength.

A.2 Fabrication

Our device is fabricated on a 9 mm × 4 mm, and 430 μm thickness sapphire substrate. The resist is spin-coated onto the diced chip, starting with a layer of MMA resist followed by a layer of PMMA resist. An Elionix system is used for e-beam writing to pattern the design onto the resist-coated chip. After development, a mask is created to outline the qubit structures. The double-angle deposition is carried out using a Plassys deposition system, with aluminum de-

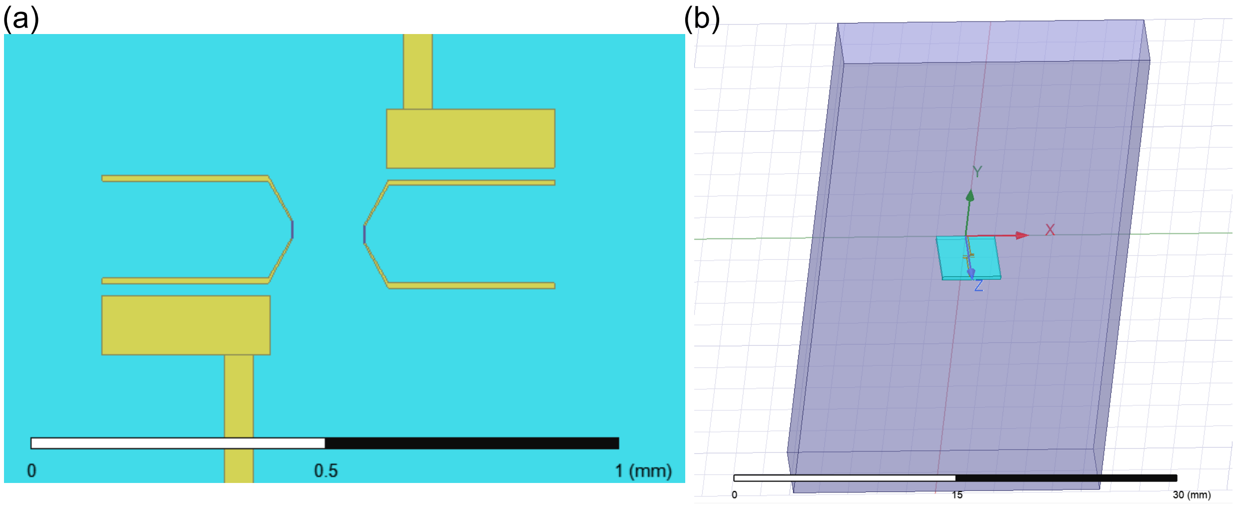

Figure A.1: HFSS 3D model of (a) the capacitor pads of our two-qubit device in a (b) 3D cavity.

posited at two angles to form the qubit structures. The process concludes with a lift-off procedure to remove excess material, leaving the patterned qubit devices. More detailed fabrication process is described in [14].

A.3 Experimental Setup

The measurement setups are similar to those previously reported in [11, 32]. In this section, we focus on our two-qubit experiments for example to illustrate the difference especially the room temperature setup shown in Fig. A.2. We send external driving into the cavity through two input ports and measure the transmission signal with the third port. The device image is shown in Fig. 4.1(a).

We perform dispersive readout using a 3D copper cavity resonator with frequency of 7.475 GHz and linewidth of 9 MHz. We carry out a single-shot joint readout of the two qubit states using a Josephson traveling parametric-wave amplifier (JTWPA) provided by Lincoln labs [128] to preamplify the readout signal. The dispersive shifts of qubit A and B are 3 and 6.5 MHz,

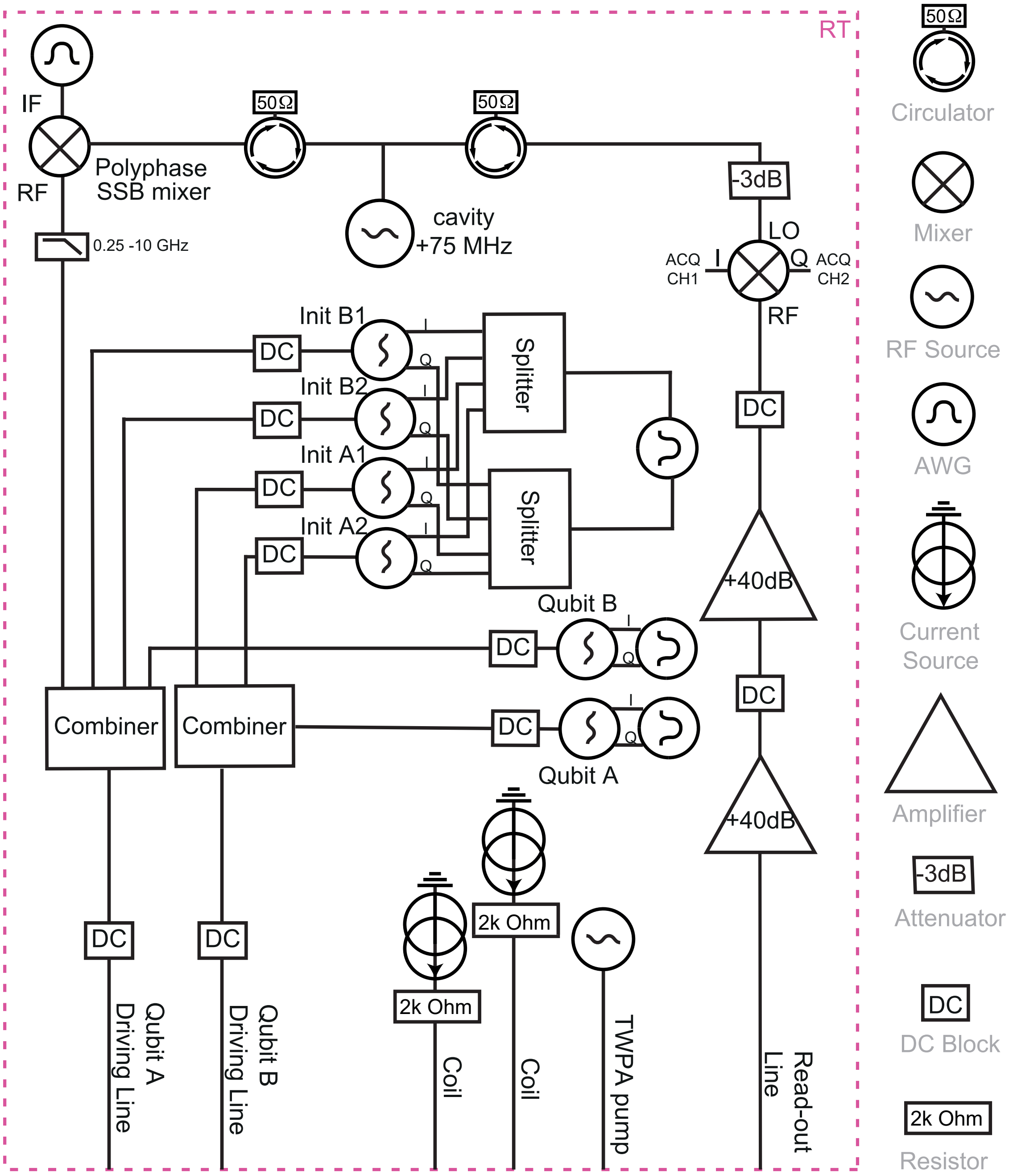

Figure A.2: Schematics of experimental setup.

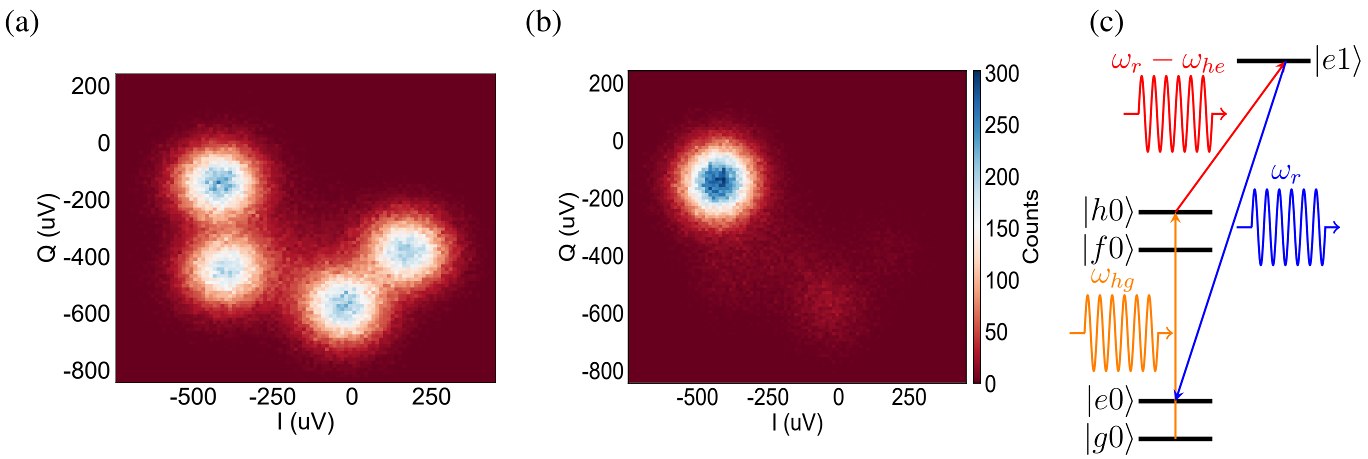

Figure A.3: (a) Single shot histograms showing the four blobs corresponding to the four computational states. (b) Single shot histograms measured after initialization. (c) Initialization scheme using an intermediate state. We apply two tone pumping along with the fast decay rate of cavity photons to initialize qubits to excited states.

respectively. By fitting the single-shot histograms as illustrated in Fig. A.3(a) with four Gaussian distributions, we extract the population of the four computational states for each experiment.

Our initialization protocol involves simultaneously driving on the $|g0\rangle \rightarrow |h0\rangle$ and $|h0\rangle \rightarrow |e1\rangle$ transitions for 25 μs, following [13]. Compared with the physical temperature, the high cavity frequency (7.475GHz) along with a low quality factor of 800 leads to rapid photon loss from the $|e1\rangle$ state to the $|e0\rangle$ state as illustrated in A.3(c). This prepares qubits A and B in a mixed state with measured excited state populations of 88% and 87%. The corresponding single-shot histograms are shown in A.3(b). This state initialization enables accurate characterization of gate errors, and we did not focus on improving initialization in this paper.

A.4 Gate Characterization Techniques: Randomized Benchmarking

Randomized Benchmarking (RB) [129, 130, 131] is a widely used technique for evaluating the average fidelity of gates within the Clifford group [132]. Building on this concept, several related methods have been developed to target specific aspects of fidelity such as purity benchmarking (PB) to measure the average incoherent error of the Clifford group and cross-entropy benchmarking (XEB) to measure the fidelity of a non-Clifford gate. In this thesis, we focus on Clifford gates and Interleaved Randomized Benchmarking (IRB) [133] that enables the characterization of the fidelity of individual Clifford gates.

The single-qubit Clifford group contains 24 distinct gates, modulo an overall phase factor. These gates correspond to all possible rotations between the six axial states, i.e., the eigenstates of the Pauli operators on the Bloch sphere. The specific decomposition of each Clifford gate may vary depending on the pulse set used in an experiment. In this thesis, each Clifford gate is constructed with one X or Y rotation with additional Z rotations as illustrated in Table A.1, which has on average 1.833 pulses per Clifford gate. The two-qubit Clifford group comprises 11520 distinct gates. These gates can be categorized into four classes: those composed of single-qubit operations, CNOT-like gates, iSWAP-like gates, and SWAP-like gates. Similar to the single-qubit case, each two-qubit Clifford gate can have multiple representations. For instance, using CZ gates along with single-qubit gates, one can construct the full set of two-qubit Clifford gates. On average, this approach requires 1.5 CZ gates and 5.583 physical single-qubit gates (incorporating virtual Z gates for the single-qubit Z rotations) per Clifford gate.

For standard RB measurements, a sequence of randomly selected Clifford gates C_i is applied to the qubit, with a different random seed used for each sequence length m, i.e., the number of Clifford gates. Due to the properties of Clifford gates, closure under composition and the existence of inverses, there always exists one recovery gate C_r that ideally returns the qubit to its initial state. Thus, the overall operation should implement the identity. However, in practice, accumulated gate errors cause deviations from the ideal final state. By measuring the final

one X or Y rotation with Z rotations
I
X_π
X_π, Z_π
Z_π
$Y_{\pi/2}, Z_{\pi/2}$
$Y_{-\pi/2}, Z_{-\pi/2}$
$Y_{\pi/2}, Z_{-\pi/2}$
$Y_{-\pi/2}, Z_{\pi/2}$
$X_{\pi/2}, Z_{-\pi/2}$
$X_{-\pi/2}, Z_{\pi/2}$
$X_{\pi/2}, Z_{\pi/2}$
$X_{-\pi/2}, Z_{-\pi/2}$
$X_{\pi/2}$
$X_{-\pi/2}$
$Y_{\pi/2}$
$Y_{-\pi/2}$
$Z_{-\pi/2}$
$Z_{\pi/2}$
$Z_{\pi/2}, X_{\pi/2}, Z_{\pi/2}$
$Z_{\pi/2}, X_{-\pi/2}, Z_{\pi/2}$
$Z_{-\pi/2}, Y_{\pi/2}, Z_{-\pi/2}$
$Z_{-\pi/2}, Y_{-\pi/2}, Z_{-\pi/2}$
$Z_{-\pi/2}, X_\pi, Z_{-\pi}$
$Z_{\pi/2}, X_\pi, Z_{-\pi}$

Table A.1: Decomposition of single-qubit Clifford gates.

state population and averaging over many random Clifford sequences of the same length, one can quantify the effect of these errors. The sequence fidelity follows

$$F_{\text{seq}}(m) = Ap^m + B, \tag{A.1}$$

where A and B account for the State Preparation And Measurement (SPAM) and the recovery gate errors. The parameter p characterizes depolarization and is related to the average error rate r of a Clifford gate by the relation

$$r = \frac{(d-1)(1-p)}{d},$$

where $d = 2^n$ is the dimension of the Hilbert space for n qubits. One can also calculate the gate error per pulse as $r_{\text{pulse}} = r/1.833$, which is applied in Chapter 3.

For IRB, we insert a target Clifford gate G after each Clifford gate C_i in the RB sequence with a new C_r to recover the sequence including G. We can evaluate the fidelity of the target gate G by comparing the depolarizing parameters extracted from RB and IRB measurements. Let p_G be the depolarizing parameter extracted from the IRB measurement, and the error rate of gate G is given by

$$r_G = \frac{(d-1)\left(1 - \frac{p_G}{p}\right)}{d}$$

. The corresponding gate fidelity is then defined as $F_G = 1 - r_G$. Additionally, one can insert n repeated G in the sequence, i.e., G^n, which remains a Clifford gate. In this case, incoherent errors scale linearly with n, while coherent errors accumulate non-linearly as we observe in Chapter 4.

Bibliography

[1] Raymond A. Mencia, Wei-Ju Lin, Hyunheung Cho, Maxim G. Vavilov, and Vladimir E. Manucharyan. Integer fluxonium qubit. *PRX Quantum*, 5:040318, Nov 2024.

[2] Wei-Ju Lin, Hyunheung Cho, Yinqi Chen, Maxim G Vavilov, Chen Wang, and Vladimir E Manucharyan. Verifying the analogy between transversely coupled spin-1/2 systems and inductively-coupled fluxoniums. *New Journal of Physics*, 27(3):033012, mar 2025.

[3] Wei-Ju Lin, Hyunheung Cho, Yinqi Chen, Maxim G. Vavilov, Chen Wang, and Vladimir E. Manucharyan. 24 days-stable cnot gate on fluxonium qubits with over 99.9% fidelity. *PRX Quantum*, 6:010349, Mar 2025.

[4] B.D. Josephson. Possible new effects in superconductive tunnelling. *Physics Letters*, 1(7):251–253, 1962.

[5] Alexandre Blais, Arne L. Grimsmo, S. M. Girvin, and Andreas Wallraff. Circuit quantum electrodynamics. *Rev. Mod. Phys.*, 93:025005, May 2021.

[6] Jens Koch, Terri M. Yu, Jay Gambetta, A. A. Houck, D. I. Schuster, J. Majer, Alexandre Blais, M. H. Devoret, S. M. Girvin, and R. J. Schoelkopf. Charge-insensitive qubit design derived from the cooper pair box. *Phys. Rev. A*, 76:042319, Oct 2007.

[7] Google Quantum AI and Collaborators. Overcoming leakage in quantum error correction. *Nature Physics*, 19:1780, Dec 2023.

[8] Vladimir E Manucharyan, Jens Koch, Leonid I Glazman, and Michel H Devoret. Fluxonium: Single cooper-pair circuit free of charge offsets. *Science*, 326(5949):113–116, 2009.

[9] Yen-Hsiang Lin, Long B. Nguyen, Nicholas Grabon, Jonathan San Miguel, Natalia Pankratova, and Vladimir E. Manucharyan. Demonstration of protection of a superconducting qubit from energy decay. *Phys. Rev. Lett.*, 120:150503, Apr 2018.

[10] N. Earnest, S. Chakram, Y. Lu, N. Irons, R. K. Naik, N. Leung, L. Ocola, D. A. Czaplewski, B. Baker, Jay Lawrence, Jens Koch, and D. I. Schuster. Realization of a Λ system with metastable states of a capacitively shunted fluxonium. *Phys. Rev. Lett.*, 120:150504, Apr 2018.

[11] Long B. Nguyen, Yen-Hsiang Lin, Aaron Somoroff, Raymond Mencia, Nicholas Grabon, and Vladimir E. Manucharyan. High-coherence fluxonium qubit. *Phys. Rev. X*, 9:041041, Nov 2019.

[12] Pranav S. Mundada, András Gyenis, Ziwen Huang, Jens Koch, and Andrew A. Houck. Floquet-engineered enhancement of coherence times in a driven fluxonium qubit. *Phys. Rev. Appl.*, 14:054033, Nov 2020.

[13] Helin Zhang, Srivatsan Chakram, Tanay Roy, Nathan Earnest, Yao Lu, Ziwen Huang, D. K. Weiss, Jens Koch, and David I. Schuster. Universal fast-flux control of a coherent, low-frequency qubit. *Phys. Rev. X*, 11:011010, Jan 2021.

[14] Aaron Somoroff, Quentin Ficheux, Raymond A. Mencia, Haonan Xiong, Roman Kuzmin, and Vladimir E. Manucharyan. Millisecond coherence in a superconducting qubit. *Phys. Rev. Lett.*, 130:267001, Jun 2023.

[15] Hantao Sun, Feng Wu, Hsiang-Sheng Ku, Xizheng Ma, Jin Qin, Zhijun Song, Tenghui Wang, Gengyan Zhang, Jingwei Zhou, Yaoyun Shi, Hui-Hai Zhao, and Chunqing Deng. Characterization of loss mechanisms in a fluxonium qubit. *Phys. Rev. Appl.*, 20:034016, Sep 2023.

[16] Waël Ardati, Sébastien Léger, Shelender Kumar, Vishnu Narayanan Suresh, Dorian Nicolas, Cyril Mori, Francesca D'Esposito, Tereza Vakhtel, Olivier Buisson, Quentin Ficheux, and Nicolas Roch. Using bifluxon tunneling to protect the fluxonium qubit. *Phys. Rev. X*, 14:041014, Oct 2024.

[17] David P. DiVincenzo. The physical implementation of quantum computation. *Fortschritte der Physik*, 48(9-11):771–783, 2000.

[18] Google Quantum AI and Collaborators. Quantum error correction below the surface code threshold. *Nature*, 638:920, Feb 2025.

[19] R. Barends, J. Kelly, A. Megrant, A. Veitia, D. Sank, E. Jeffrey, T. C. White, J. Mutus, A. G. Fowler, B. Campbell, Y. Chen, Z. Chen, B. Chiaro, A. Dunsworth, C. Neill, P. O'Malley, P. Roushan, A. Vainsencher, J. Wenner, A. N. Korotkov, A. N. Cleland, and John M. Martinis. Superconducting quantum circuits at the surface code threshold for fault tolerance. *Nature*, 508:500, Apr 2014.

[20] R. Barends, C. M. Quintana, A. G. Petukhov, Yu Chen, D. Kafri, K. Kechedzhi, R. Collins, O. Naaman, S. Boixo, F. Arute, K. Arya, D. Buell, B. Burkett, Z. Chen, B. Chiaro, A. Dunsworth, B. Foxen, A. Fowler, C. Gidney, M. Giustina, R. Graff, T. Huang, E. Jeffrey, J. Kelly, P. V. Klimov, F. Kostritsa, D. Landhuis, E. Lucero, M. McEwen, A. Megrant, X. Mi, J. Mutus, M. Neeley, C. Neill, E. Ostby, P. Roushan, D. Sank, K. J. Satzinger, A. Vainsencher, T. White, J. Yao, P. Yeh, A. Zalcman, H. Neven, V. N. Smelyanskiy, and John M. Martinis. Diabatic gates for frequency-tunable superconducting qubits. *Phys. Rev. Lett.*, 123:210501, Nov 2019.

[21] Shaowei Li, Anthony D. Castellano, Shiyu Wang, Yulin Wu, Ming Gong, Zhiguang Yan, Hao Rong, Hui Deng, Chen Zha, Cheng Guo, Lihua Sun, Chengzhi Peng, Xiaobo Zhu, and Jian-Wei Pan. Realisation of high-fidelity nonadiabatic cz gates with superconducting qubits. *npj Quantum Information*, 5:84, Oct 2019.

[22] V. Negîrneac, H. Ali, N. Muthusubramanian, F. Battistel, R. Sagastizabal, M. S. Moreira, J. F. Marques, W. J. Vlothuizen, M. Beekman, C. Zachariadis, N. Haider, A. Bruno, and L. DiCarlo. High-fidelity controlled-z gate with maximal intermediate leakage operating at the speed limit in a superconducting quantum processor. *Phys. Rev. Lett.*, 126:220502, Jun 2021.

[23] Long B Nguyen, Yosep Kim, Akel Hashim, Noah Goss, Brian Marinelli, Bibek Bhandari, Debmalya Das, Ravi K Naik, John Mark Kreikebaum, Andrew N Jordan, et al. Programmable heisenberg interactions between floquet qubits. *Nature Physics*, pages 1–7, 2024.

[24] Bradley K. Mitchell, Ravi K. Naik, Alexis Morvan, Akel Hashim, John Mark Kreikebaum, Brian Marinelli, Wim Lavrijsen, Kasra Nowrouzi, David I. Santiago, and Irfan Siddiqi. Hardware-efficient microwave-activated tunable coupling between superconducting qubits. *Phys. Rev. Lett.*, 127:200502, Nov 2021.

[25] K. X. Wei, E. Magesan, I. Lauer, S. Srinivasan, D. F. Bogorin, S. Carnevale, G. A. Keefe, Y. Kim, D. Klaus, W. Landers, N. Sundaresan, C. Wang, E. J. Zhang, M. Steffen, O. E. Dial, D. C. McKay, and A. Kandala. Hamiltonian engineering with multicolor drives for fast entangling gates and quantum crosstalk cancellation. *Phys. Rev. Lett.*, 129:060501, Aug 2022.

[26] A. Kandala, K. X. Wei, S. Srinivasan, E. Magesan, S. Carnevale, G. A. Keefe, D. Klaus, O. Dial, and D. C. McKay. Demonstration of a high-fidelity cnot gate for fixed-frequency transmons with engineered zz suppression. *Phys. Rev. Lett.*, 127:130501, Sep 2021.

[27] Yuan Xu, Ji Chu, Jiahao Yuan, Jiawei Qiu, Yuxuan Zhou, Libo Zhang, Xinsheng Tan, Yang Yu, Song Liu, Jian Li, Fei Yan, and Dapeng Yu. High-fidelity, high-scalability two-qubit gate scheme for superconducting qubits. *Phys. Rev. Lett.*, 125:240503, Dec 2020.

[28] J. Stehlik, D. M. Zajac, D. L. Underwood, T. Phung, J. Blair, S. Carnevale, D. Klaus, G. A. Keefe, A. Carniol, M. Kumph, Matthias Steffen, and O. E. Dial. Tunable coupling architecture for fixed-frequency transmon superconducting qubits. *Phys. Rev. Lett.*, 127:080505, Aug 2021.

[29] Youngkyu Sung, Leon Ding, Jochen Braumüller, Antti Vepsäläinen, Bharath Kannan, Morten Kjaergaard, Ami Greene, Gabriel O. Samach, Chris McNally, David Kim, Alexander Melville, Bethany M. Niedzielski, Mollie E. Schwartz, Jonilyn L. Yoder, Terry P. Orlando, Simon Gustavsson, and William D. Oliver. Realization of high-fidelity cz and zz-free iswap gates with a tunable coupler. *Phys. Rev. X*, 11:021058, Jun 2021.

[30] B. Foxen, C. Neill, A. Dunsworth, P. Roushan, B. Chiaro, A. Megrant, J. Kelly, Zijun Chen, K. Satzinger, R. Barends, F. Arute, K. Arya, R. Babbush, D. Bacon, J. C. Bardin, S. Boixo,

D. Buell, B. Burkett, Yu Chen, R. Collins, E. Farhi, A. Fowler, C. Gidney, M. Giustina, R. Graff, M. Harrigan, T. Huang, S. V. Isakov, E. Jeffrey, Z. Jiang, D. Kafri, K. Kechedzhi, P. Klimov, A. Korotkov, F. Kostritsa, D. Landhuis, E. Lucero, J. McClean, M. McEwen, X. Mi, M. Mohseni, J. Y. Mutus, O. Naaman, M. Neeley, M. Niu, A. Petukhov, C. Quintana, N. Rubin, D. Sank, V. Smelyanskiy, A. Vainsencher, T. C. White, Z. Yao, P. Yeh, A. Zalcman, H. Neven, and J. M. Martinis. Demonstrating a continuous set of two-qubit gates for near-term quantum algorithms. *Phys. Rev. Lett.*, 125:120504, Sep 2020.

[31] Quentin Ficheux, Long B. Nguyen, Aaron Somoroff, Haonan Xiong, Konstantin N. Nesterov, Maxim G. Vavilov, and Vladimir E. Manucharyan. Fast logic with slow qubits: Microwave-activated controlled-z gate on low-frequency fluxoniums. *Phys. Rev. X*, 11:021026, May 2021.

[32] Haonan Xiong, Quentin Ficheux, Aaron Somoroff, Long B. Nguyen, Ebru Dogan, Dario Rosenstock, Chen Wang, Konstantin N. Nesterov, Maxim G. Vavilov, and Vladimir E. Manucharyan. Arbitrary controlled-phase gate on fluxonium qubits using differential ac stark shifts. *Phys. Rev. Res.*, 4:023040, Apr 2022.

[33] Leon Ding, Max Hays, Youngkyu Sung, Bharath Kannan, Junyoung An, Agustin Di Paolo, Amir H. Karamlou, Thomas M. Hazard, Kate Azar, David K. Kim, Bethany M. Niedzielski, Alexander Melville, Mollie E. Schwartz, Jonilyn L. Yoder, Terry P. Orlando, Simon Gustavsson, Jeffrey A. Grover, Kyle Serniak, and William D. Oliver. High-fidelity, frequency-flexible two-qubit fluxonium gates with a transmon coupler. *Phys. Rev. X*, 13:031035, Sep 2023.

[34] Helin Zhang, Chunyang Ding, D.K. Weiss, Ziwen Huang, Yuwei Ma, Charles Guinn, Sara Sussman, Sai Pavan Chitta, Danyang Chen, Andrew A. Houck, Jens Koch, and David I. Schuster. Tunable inductive coupler for high-fidelity gates between fluxonium qubits. *PRX Quantum*, 5:020326, May 2024.

[35] Ilya N Moskalenko, Ilya A Simakov, Nikolay N Abramov, Alexander A Grigorev, Dmitry O Moskalev, Anastasiya A Pishchimova, Nikita S Smirnov, Evgeniy V Zikiy, Ilya A Rodionov, and Ilya S Besedin. High fidelity two-qubit gates on fluxoniums using a tunable coupler. *npj Quantum Information*, 8(1):130, 2022.

[36] Feng Bao, Hao Deng, Dawei Ding, Ran Gao, Xun Gao, Cupjin Huang, Xun Jiang, Hsiang-Sheng Ku, Zhisheng Li, Xizheng Ma, Xiaotong Ni, Jin Qin, Zhijun Song, Hantao Sun, Chengchun Tang, Tenghui Wang, Feng Wu, Tian Xia, Wenlong Yu, Fang Zhang, Gengyan Zhang, Xiaohang Zhang, Jingwei Zhou, Xing Zhu, Yaoyun Shi, Jianxin Chen, Hui-Hai Zhao, and Chunqing Deng. Fluxonium: An alternative qubit platform for high-fidelity operations. *Phys. Rev. Lett.*, 129:010502, Jun 2022.

[37] Xizheng Ma, Gengyan Zhang, Feng Wu, Feng Bao, Xu Chang, Jianjun Chen, Hao Deng, Ran Gao, Xun Gao, Lijuan Hu, Honghong Ji, Hsiang-Sheng Ku, Kannan Lu, Lu Ma, Liyong Mao, Zhijun Song, Hantao Sun, Chengchun Tang, Fei Wang, Hongcheng Wang, Tenghui Wang, Tian Xia, Make Ying, Huijuan Zhan, Tao Zhou, Mengyu Zhu, Qingbin Zhu, Yaoyun Shi, Hui-Hai Zhao, and Chunqing Deng. Native approach to controlled-z gates in inductively coupled fluxonium qubits. *Phys. Rev. Lett.*, 132:060602, Feb 2024.

[38] Ebru Dogan, Dario Rosenstock, Loïck Le Guevel, Haonan Xiong, Raymond A. Mencia, Aaron Somoroff, Konstantin N. Nesterov, Maxim G. Vavilov, Vladimir E. Manucharyan, and Chen Wang. Two-fluxonium cross-resonance gate. *Phys. Rev. Appl.*, 20:024011, Aug 2023.

[39] Y. Nakamura, Yu. A. Pashkin, and J. S. Tsai. Coherent control of macroscopic quantum states in a single-cooper-pair box. *Nature*, 398(6730):786–788, 1999.

[40] Atharv Joshi, Kyungjoo Noh, and Yvonne Y Gao. Quantum information processing with bosonic qubits in circuit qed. *Quantum Science and Technology*, 6(3):033001, apr 2021.

[41] Peter Groszkowski and Jens Koch. Scqubits: a python package for superconducting qubits. *Quantum*, 5:583, 2021.

[42] Jacob Bryon, D.K. Weiss, Xinyuan You, Sara Sussman, Xanthe Croot, Ziwen Huang, Jens Koch, and Andrew A. Houck. Time-dependent magnetic flux in devices for circuit quantum electrodynamics. *Phys. Rev. Appl.*, 19:034031, Mar 2023.

[43] V. E. Manucharyan. Superinductance. *PhD thesis*, 2012.

[44] Long B. Nguyen. Toward the fluxonium quantum processor. *PhD thesis*, 2020.

[45] S. M. Girvin. Circuit qed: superconducting qubits coupled to microwave photons. In *Quantum Machines: Measurement and Control of Engineered Quantum Systems: Lecture Notes of the Les Houches Summer School: Volume 96, July 2011*. Oxford University Press, 06 2014.

[46] R. J. Schoelkopf, A. A. Clerk, S. M. Girvin, K. W. Lehnert, and M. H. Devoret. *Qubits as Spectrometers of Quantum Noise*, pages 175–203. Springer Netherlands, Dordrecht, 2003.

[47] C. Wang, C. Axline, Y. Y. Gao, T. Brecht, Y. Chu, L. Frunzio, M. H. Devoret, and R. J. Schoelkopf. Surface participation and dielectric loss in superconducting qubits. *Applied Physics Letters*, 107(16):162601, 10 2015.

[48] M H Devoret. Quantum fluctuations in electrical circuits, Dec 1997.

[49] Simon Gustavsson, Fei Yan, Gianluigi Catelani, Jonas Bylander, Archana Kamal, Jeffrey Birenbaum, David Hover, Danna Rosenberg, Gabriel Samach, Adam P. Sears, Steven J. Weber, Jonilyn L. Yoder, John Clarke, Andrew J. Kerman, Fumiki Yoshihara, Yasunobu Nakamura, Terry P. Orlando, and William D. Oliver. Suppressing relaxation in superconducting qubits by quasiparticle pumping. *Science*, 354(6319):1573–1577, 2016.

[50] E. M. Purcell. *Spontaneous Emission Probabilities at Radio Frequencies*, pages 839–839. Springer US, Boston, MA, 1995.

[51] E. L. Hahn. Spin echoes. *Phys. Rev.*, 80:580–594, Nov 1950.

[52] S. Meiboom and D. Gill. Modified spin-echo method for measuring nuclear relaxation times. *Review of Scientific Instruments*, 29(8):688–691, 08 1958.

[53] H. Y. Carr and E. M. Purcell. Effects of diffusion on free precession in nuclear magnetic resonance experiments. *Phys. Rev.*, 94:630–638, May 1954.

[54] Yuriy Makhlin and Alexander Shnirman. Dephasing of solid-state qubits at optimal points. *Phys. Rev. Lett.*, 92:178301, Apr 2004.

[55] Chad Rigetti, Jay M. Gambetta, Stefano Poletto, B. L. T. Plourde, Jerry M. Chow, A. D. Córcoles, John A. Smolin, Seth T. Merkel, J. R. Rozen, George A. Keefe, Mary B. Rothwell, Mark B. Ketchen, and M. Steffen. Superconducting qubit in a waveguide cavity with a coherence time approaching 0.1 ms. *Phys. Rev. B*, 86:100506, Sep 2012.

[56] Vladimir E. Manucharyan, Nicholas A. Masluk, Archana Kamal, Jens Koch, Leonid I. Glazman, and Michel H. Devoret. Evidence for coherent quantum phase slips across a josephson junction array. *Phys. Rev. B*, 85:024521, Jan 2012.

[57] Mallika T. Randeria, Thomas M. Hazard, Agustin Di Paolo, Kate Azar, Max Hays, Leon Ding, Junyoung An, Michael Gingras, Bethany M. Niedzielski, Hannah Stickler, Jeffrey A. Grover, Jonilyn L. Yoder, Mollie E. Schwartz, William D. Oliver, and Kyle Serniak. Dephasing in fluxonium qubits from coherent quantum phase slips. *PRX Quantum*, 5:030341, Aug 2024.

[58] M. H. Devoret and R. J. Schoelkopf. Superconducting Circuits for Quantum Information: An Outlook. *Science*, 339(6124):1169, 2013.

[59] G. Wendin. Quantum information processing with superconducting circuits: a review. *Rep. Prog. Phys.*, 80:106001, 2017.

[60] M. Kjaergaard, M. E. Schwartz, J. Braumüller, P. Krantz, J. I-J Wang, S. Gustavsson, and W. D. Oliver. Superconducting Qubits: Current State of Play. *Annu. Rev. Condens. Matter Phys.*, 11:369, 2020.

[61] David C. McKay, Stefan Filipp, Antonio Mezzacapo, Easwar Magesan, Jerry M. Chow, and Jay M. Gambetta. Universal gate for fixed-frequency qubits via a tunable bus. *Phys. Rev. Appl.*, 6:064007, Dec 2016.

[62] Fei Yan, Philip Krantz, Youngkyu Sung, Morten Kjaergaard, Daniel L. Campbell, Terry P. Orlando, Simon Gustavsson, and William D. Oliver. Tunable coupling scheme for implementing high-fidelity two-qubit gates. *Phys. Rev. Appl.*, 10:054062, Nov 2018.

[63] Pranav Mundada, Gengyan Zhang, Thomas Hazard, and Andrew Houck. Suppression of qubit crosstalk in a tunable coupling superconducting circuit. *Phys. Rev. Appl.*, 12:054023, Nov 2019.

[64] Michele C. Collodo, Johannes Herrmann, Nathan Lacroix, Christian Kraglund Andersen, Ants Remm, Stefania Lazar, Jean-Claude Besse, Theo Walter, Andreas Wallraff, and Christopher Eichler. Implementation of conditional phase gates based on tunable zz interactions. *Phys. Rev. Lett.*, 125:240502, Dec 2020.

[65] R. C. Bialczak, M. Ansmann, M. Hofheinz, M. Lenander, E. Lucero, M. Neeley, A. D. O'Connell, D. Sank, H. Wang, M. Weides, J. Wenner, T. Yamamoto, A. N. Cleland, and J. M. Martinis. Fast tunable coupler for superconducting qubits. *Phys. Rev. Lett.*, 106:060501, Feb 2011.

[66] Konstantin N. Nesterov, Ivan V. Pechenezhskiy, Chen Wang, Vladimir E. Manucharyan, and Maxim G. Vavilov. Microwave-activated controlled-z gate for fixed-frequency fluxonium qubits. *Phys. Rev. A*, 98:030301, Sep 2018.

[67] Xizheng Ma, Gengyan Zhang, Feng Wu, Feng Bao, Xu Chang, Jianjun Chen, Hao Deng, Ran Gao, Xun Gao, Lijuan Hu, Honghong Ji, Hsiang-Sheng Ku, Kannan Lu, Lu Ma, Liyong Mao, Zhijun Song, Hantao Sun, Chengchun Tang, Fei Wang, Hongcheng Wang, Tenghui Wang, Tian Xia, Make Ying, Huijuan Zhan, Tao Zhou, Mengyu Zhu, Qingbin Zhu, Yaoyun Shi, Hui-Hai Zhao, and Chunqing Deng. Native approach to controlled-z gates in inductively coupled fluxonium qubits. *Phys. Rev. Lett.*, 132:060602, Feb 2024.

[68] Long B. Nguyen, Gerwin Koolstra, Yosep Kim, Alexis Morvan, Trevor Chistolini, Shraddha Singh, Konstantin N. Nesterov, Christian Jünger, Larry Chen, Zahra Pedramrazi, Bradley K. Mitchell, John Mark Kreikebaum, Shruti Puri, David I. Santiago, and Irfan Siddiqi. Blueprint for a high-performance fluxonium quantum processor. *PRX Quantum*, 3:037001, Aug 2022.

[69] David A. Rower, Leon Ding, Helin Zhang, Max Hays, Junyoung An, Patrick M. Harrington, Ilan T. Rosen, Jeffrey M. Gertler, Thomas M. Hazard, Bethany M. Niedzielski, Mollie E. Schwartz, Simon Gustavsson, Kyle Serniak, Jeffrey A. Grover, and William D. Oliver. Suppressing counter-rotating errors for fast single-qubit gates with fluxonium. *PRX Quantum*, 5:040342, Dec 2024.

[70] David C. McKay, Christopher J. Wood, Sarah Sheldon, Jerry M. Chow, and Jay M. Gambetta. Efficient z gates for quantum computing. *Phys. Rev. A*, 96:022330, Aug 2017.

[71] D. A. Stech. *Quantum and Atom Optics*. 2007.

[72] J. M. Gambetta, F. Motzoi, S. T. Merkel, and F. K. Wilhelm. Analytic control methods for high-fidelity unitary operations in a weakly nonlinear oscillator. *Phys. Rev. A*, 83:012308, Jan 2011.

[73] F. Motzoi, J. M. Gambetta, P. Rebentrost, and F. K. Wilhelm. Simple pulses for elimination of leakage in weakly nonlinear qubits. *Phys. Rev. Lett.*, 103:110501, Sep 2009.

[74] András Gyenis, Pranav S. Mundada, Agustin Di Paolo, Thomas M. Hazard, Xinyuan You, David I. Schuster, Jens Koch, Alexandre Blais, and Andrew A. Houck. Experimental realization of a protected superconducting circuit derived from the 0–π qubit. *PRX Quantum*, 2:010339, Mar 2021.

[75] K. A. Matveev, A. I. Larkin, and L. I. Glazman. Persistent current in superconducting nanorings. *Phys. Rev. Lett.*, 89:096802, Aug 2002.

[76] J. R. Johansson, P. D. Nation, and F. Nori. QuTiP: An open-source Python framework for the dynamics of open quantum systems. *Comp. Phys. Comm.*, 183(8):1760, 8 2012.

[77] J. R. Johansson, P. D. Nation, and F. Nori. QuTiP 2: A Python framework for the dynamics of open quantum systems. *Comp. Phys. Comm.*, 184(4):1234, 4 2013.

[78] Line Hjortshøj Pedersen, Niels Martin Møller, and Klaus Mølmer. Fidelity of quantum operations. *Physics Letters A*, 367(1):47–51, 2007.

[79] Vinay Tripathi, Mostafa Khezri, and Alexander N. Korotkov. Operation and intrinsic error budget of a two-qubit cross-resonance gate. *Phys. Rev. A*, 100:012301, Jul 2019.

[80] Tahereh Abad, Jorge Fernández-Pendás, Anton Frisk Kockum, and Göran Johansson. Universal fidelity reduction of quantum operations from weak dissipation. *Phys. Rev. Lett.*, 129:150504, Oct 2022.

[81] Sarah Sheldon, Easwar Magesan, Jerry M. Chow, and Jay M. Gambetta. Procedure for systematically tuning up cross-talk in the cross-resonance gate. *Phys. Rev. A*, 93:060302, Jun 2016.

[82] Kentaro Heya and Naoki Kanazawa. Cross-cross resonance gate. *PRX Quantum*, 2:040336, Nov 2021.

[83] A D Córcoles, Jay M Gambetta, Jerry M Chow, John A Smolin, Matthew Ware, Joel Strand, B L T Plourde, and M Steffen. Process verification of two-qubit quantum gates by randomized benchmarking. *Phys. Rev. A*, 87:030301, 2013.

[84] Sumeru Hazra, Kishor V. Salunkhe, Anirban Bhattacharjee, Gaurav Bothara, Suman Kundu, Tanay Roy, Meghan P. Patankar, and R. Vijay. Engineering cross resonance interaction in multi-modal quantum circuits. *Applied Physics Letters*, 116(15):152601, 04 2020.

[85] A.D. Patterson, J. Rahamim, T. Tsunoda, P.A. Spring, S. Jebari, K. Ratter, M. Mergenthaler, G. Tancredi, B. Vlastakis, M. Esposito, and P.J. Leek. Calibration of a cross-resonance two-qubit gate between directly coupled transmons. *Phys. Rev. Appl.*, 12:064013, Dec 2019.

[86] Konstantin N. Nesterov, Chen Wang, Vladimir E. Manucharyan, and Maxim G. Vavilov. cnot gates for fluxonium qubits via selective darkening of transitions. *Phys. Rev. Appl.*, 18:034063, Sep 2022.

[87] Yinqi Chen, Konstantin N. Nesterov, Vladimir E. Manucharyan, and Maxim G. Vavilov. Fast flux entangling gate for fluxonium circuits. *Phys. Rev. Appl.*, 18:034027, Sep 2022.

[88] David C. McKay, Sarah Sheldon, John A. Smolin, Jerry M. Chow, and Jay M. Gambetta. Three-qubit randomized benchmarking. *Phys. Rev. Lett.*, 122:200502, May 2019.

[89] S. J. Srinivasan, A. J. Hoffman, J. M. Gambetta, and A. A. Houck. Tunable coupling in circuit quantum electrodynamics using a superconducting charge qubit with a v-shaped energy level diagram. *Phys. Rev. Lett.*, 106:083601, Feb 2011.

[90] Yu Chen, C. Neill, P. Roushan, N. Leung, M. Fang, R. Barends, J. Kelly, B. Campbell, Z. Chen, B. Chiaro, A. Dunsworth, E. Jeffrey, A. Megrant, J. Y. Mutus, P. J. J. O'Malley, C. M. Quintana, D. Sank, A. Vainsencher, J. Wenner, T. C. White, Michael R. Geller, A. N. Cleland, and John M. Martinis. Qubit architecture with high coherence and fast tunable coupling. *Phys. Rev. Lett.*, 113:220502, Nov 2014.

[91] L. Casparis, N. J. Pearson, A. Kringhøj, T. W. Larsen, F. Kuemmeth, J. Nygård, P. Krogstrup, K. D. Petersson, and C. M. Marcus. Voltage-controlled superconducting quantum bus. *Phys. Rev. B*, 99:085434, Feb 2019.

[92] M. Ganzhorn, D.J. Egger, P. Barkoutsos, P. Ollitrault, G. Salis, N. Moll, M. Roth, A. Fuhrer, P. Mueller, S. Woerner, I. Tavernelli, and S. Filipp. Gate-efficient simulation of molecular eigenstates on a quantum computer. *Phys. Rev. Appl.*, 11:044092, Apr 2019.

[93] Jaseung Ku, Xuexin Xu, Markus Brink, David C. McKay, Jared B. Hertzberg, Mohammad H. Ansari, and B. L. T. Plourde. Suppression of unwanted zz interactions in a hybrid two-qubit system. *Phys. Rev. Lett.*, 125:200504, Nov 2020.

[94] Matthew Reagor, Christopher B. Osborn, Nikolas Tezak, Alexa Staley, Guenevere Prawiroatmodjo, Michael Scheer, Nasser Alidoust, Eyob A. Sete, Nicolas Didier, Marcus P. da Silva, Ezer Acala, Joel Angeles, Andrew Bestwick, Maxwell Block, Benjamin Bloom, Adam Bradley, Catvu Bui, Shane Caldwell, Lauren Capelluto, Rick Chilcott, Jeff Cordova, Genya Crossman, Michael Curtis, Saniya Deshpande, Tristan El Bouayadi, Daniel Girshovich, Sabrina Hong, Alex Hudson, Peter Karalekas, Kat Kuang, Michael Lenihan, Riccardo Manenti, Thomas Manning, Jayss Marshall, Yuvraj Mohan, William O'Brien, Johannes Otterbach, Alexander Papageorge, Jean-Philip Paquette, Michael Pelstring, Anthony Polloreno, Vijay Rawat, Colm A. Ryan, Russ Renzas, Nick Rubin, Damon Russel, Michael Rust, Diego Scarabelli, Michael Selvanayagam, Rodney Sinclair, Robert Smith, Mark Suska, Ting-Wai To, Mehrnoosh Vahidpour, Nagesh Vodrahalli, Tyler Whyland, Kamal Yadav, William Zeng, and Chad T. Rigetti. Demonstration of universal parametric entangling gates on a multi-qubit lattice. *Science Advances*, 4(2):eaao3603, 2018.

[95] X. Li, T. Cai, H. Yan, Z. Wang, X. Pan, Y. Ma, W. Cai, J. Han, Z. Hua, X. Han, Y. Wu, H. Zhang, H. Wang, Yipu Song, Luming Duan, and Luyan Sun. Tunable coupler for realizing a controlled-phase gate with dynamically decoupled regime in a superconducting circuit. *Phys. Rev. Appl.*, 14:024070, Aug 2020.

[96] X. Y. Han, T. Q. Cai, X. G. Li, Y. K. Wu, Y. W. Ma, Y. L. Ma, J. H. Wang, H. Y. Zhang, Y. P. Song, and L. M. Duan. Error analysis in suppression of unwanted qubit interactions for a parametric gate in a tunable superconducting circuit. *Phys. Rev. A*, 102:022619, Aug 2020.

[97] Sandoko Kosen, Hang-Xi Li, Marcus Rommel, Daryoush Shiri, Christopher Warren, Leif Grönberg, Jaakko Salonen, Tahereh Abad, Janka Biznárová, Marco Caputo, Liangyu Chen, Kestutis Grigoras, Göran Johansson, Anton Frisk Kockum, Christian Križan, Daniel Pérez Lozano, Graham J Norris, Amr Osman, Jorge Fernández-Pendás, Alberto

Ronzani, Anita Fadavi Roudsari, Slawomir Simbierowicz, Giovanna Tancredi, Andreas Wallraff, Christopher Eichler, Joonas Govenius, and Jonas Bylander. Building blocks of a flip-chip integrated superconducting quantum processor. *Quantum Science and Technology*, 7(3):035018, jun 2022.

[98] Christopher W. Warren, Jorge Fernández-Pendás, Shahnawaz Ahmed, Tahereh Abad, Andreas Bengtsson, Janka Biznárová, Kamanasish Debnath, Xiu Gu, Christian Križan, Amr Osman, Anita Fadavi Roudsari, Per Delsing, Göran Johansson, Anton Frisk Kockum, Giovanna Tancredi, and Jonas Bylander. Extensive characterization and implementation of a family of three-qubit gates at the coherence limit. *npj Quantum Information*, 9:44, May 2023.

[99] Yongxin Song, Liberto Beltrán, Ilya Besedin, Michael Kerschbaum, Marek Pechal, François Swiadek, Christoph Hellings, Dante Colao Zanuz, Alexander Flasby, Jean-Claude Besse, and Andreas Wallraff. Realization of constant-depth fan-out with real-time feedforward on a superconducting quantum processor. *arXiv preprint arXiv:2409.06989*, 2024.

[100] PC De Groot, J Lisenfeld, RN Schouten, S Ashhab, A Lupaşcu, CJPM Harmans, and JE Mooij. Selective darkening of degenerate transitions demonstrated with two superconducting quantum bits. *Nature Physics*, 6(10):763–766, 2010.

[101] Jerry M. Chow, A. D. Córcoles, Jay M. Gambetta, Chad Rigetti, B. R. Johnson, John A. Smolin, J. R. Rozen, George A. Keefe, Mary B. Rothwell, Mark B. Ketchen, and M. Steffen. Simple all-microwave entangling gate for fixed-frequency superconducting qubits. *Phys. Rev. Lett.*, 107:080502, Aug 2011.

[102] Moein Malekakhlagh and Easwar Magesan. Mitigating off-resonant error in the cross-resonance gate. *Phys. Rev. A*, 105:012602, Jan 2022.

[103] Petar Jurcevic, Ali Javadi-Abhari, Lev S Bishop, Isaac Lauer, Daniela F Bogorin, Markus Brink, Lauren Capelluto, Oktay Günlük, Toshinari Itoko, Naoki Kanazawa, Abhinav Kandala, George A Keefe, Kevin Krsulich, William Landers, Eric P Lewandowski, Douglas T McClure, Giacomo Nannicini, Adinath Narasgond, Hasan M Nayfeh, Emily Pritchett, Mary Beth Rothwell, Srikanth Srinivasan, Neereja Sundaresan, Cindy Wang, Ken X Wei, Christopher J Wood, Jeng-Bang Yau, Eric J Zhang, Oliver E Dial, Jerry M Chow, and Jay M Gambetta. Demonstration of quantum volume 64 on a superconducting quantum computing system. *Quantum Science and Technology*, 6(2):025020, mar 2021.

[104] G. S. Paraoanu. Microwave-induced coupling of superconducting qubits. *Phys. Rev. B*, 74:140504, Oct 2006.

[105] David C. McKay, Christopher J. Wood, Sarah Sheldon, Jerry M. Chow, and Jay M. Gambetta. Efficient z gates for quantum computing. *Phys. Rev. A*, 96:022330, Aug 2017.

[106] L. H. Pedersen, N. M. Møller, and K. Mølmer. Fidelity of quantum operations. *Phys. Lett. A*, 367(1-2):47–51, 2007.

[107] Cora N. Barrett, Amir H. Karamlou, Sarah E. Muschinske, Ilan T. Rosen, Jochen Braumüller, Rabindra Das, David K. Kim, Bethany M. Niedzielski, Meghan Schuldt, Kyle Serniak, Mollie E. Schwartz, Jonilyn L. Yoder, Terry P. Orlando, Simon Gustavsson, Jeffrey A. Grover, and William D. Oliver. Learning-based calibration of flux crosstalk in transmon qubit arrays. *Phys. Rev. Appl.*, 20:024070, Aug 2023.

[108] David C. McKay, Ian Hincks, Emily J. Pritchett, Malcolm Carroll, Luke C. G. Govia, and Seth T. MerkelLin. Benchmarking quantum processor performance at scale. *arXiv preprint arXiv:2311.05933*, 2023.

[109] G S Paraoanu. Microwave-induced coupling of superconducting qubits. *Phys. Rev. B*, 74(14):140504, 10 2006.

[110] Chad Rigetti and Michel Devoret. Fully microwave-tunable universal gates in superconducting qubits with linear couplings and fixed transition frequencies. *Phys. Rev. B*, 81(13):134507, 4 2010.

[111] Pavel D. Kurilovich, Thomas Connolly, Charlotte G. L. Bøttcher, Daniel K. Weiss, Sumeru Hazra, Vidul R. Joshi, Andy Z. Ding, Heekun Nho, Spencer Diamond, Vladislav D. Kurilovich, Wei Dai, Valla Fatemi, Luigi Frunzio, Leonid I. Glazman, and Michel H. Devoret. High-frequency readout free from transmon multi-excitation resonances, 2025.

[112] W. Dai, S. Hazra, D. K. Weiss, P. D. Kurilovich, T. Connolly, H. K. Babla, S. Singh, V. R. Joshi, A. Z. Ding, P. D. Parakh, J. Venkatraman, X. Xiao, L. Frunzio, and M. H. Devoret. Spectroscopy of drive-induced unwanted state transitions in superconducting circuits, 2025.

[113] Marie Frédérique Dumas, Benjamin Groleau-Paré, Alexander McDonald, Manuel H. Muñoz Arias, Cristóbal Lledó, Benjamin D'Anjou, and Alexandre Blais. Measurement-induced transmon ionization. *Phys. Rev. X*, 14:041023, Oct 2024.

[114] Alexander McDonald, Alex Chapple, Boris Varbanov, and Alexandre Blais. Readout and fluxonioum ionization: lessons, pitfalls, and advice. *APS March Meeting Abstracts*, page Q17, 2025.

[115] Konstantin Nesterov, Ivan Pechenezhskiy, Ants Remm, Leon Ding, Youngkyu Sung, and Bharath Kannan. Predicting measurement-induced state transitions in fluxonium readout. *APS March Meeting Abstracts*, page Q17, 2025.

[116] Nicolas Didier, Jérôme Bourassa, and Alexandre Blais. Fast quantum nondemolition readout by parametric modulation of longitudinal qubit-oscillator interaction. *Phys. Rev. Lett.*, 115:203601, Nov 2015.

[117] Alex A. Chapple, Alexander McDonald, Manuel H. Muñoz-Arias, and Alexandre Blais. Robustness of longitudinal transmon readout to ionization, 2024.

[118] Alex A. Chapple, Othmane Benhayoune-Khadraoui, Simon Richer, and Alexandre Blais. Balanced cross-kerr coupling for superconducting qubit readout, 2025.

[119] Can Wang, Feng-Ming Liu, He Chen, Yi-Fei Du, Chong Ying, Jian-Wen Wang, Yong-Heng Huo, Cheng-Zhi Peng, Xiaobo Zhu, Ming-Cheng Chen, Chao-Yang Lu, and Jian-Wei Pan. 99.9%-fidelity in measuring a superconducting qubit, 2024.

[120] Aayam Bista, Matthew Thibodeau, Ke Nie, Kaicheung Chow, Bryan K. Clark, and Angela Kou. Readout-induced leakage of the fluxonium qubit, 2025.

[121] Michael A. Gingras, Bethany M. Niedzielski, Kevin A. Grossklaus, Duncan Miller, Felipe Contipelli, Kate Azar, Luke D. Burkhart, Gregory Calusine, Daniel Davis, Renée DePencier Piñero, Jeffrey M. Gertler, Thomas M. Hazard, Cyrus F. Hirjibehedin, David K. Kim, Jeffrey M. Knecht, Alexander J. Melville, Christopher O'Connell, Robert A. Rood, Ali Sabbah, Hannah Stickler, Jonilyn L. Yoder, William D. Oliver, Mollie E. Schwartz, and Kyle Serniak. Improving transmon qubit performance with fluorine-based surface treatments, 2025.

[122] Paul Manset, José Palomo, Aurélien Schmitt, Kyrylo Gerashchenko, Rémi Rousseau, Himanshu Patange, Patrick Abgrall, Emmanuel Flurin, Samuel Deléglise, Thibaut Jacqmin, and Léo Balembois. Hyperinductance based on stacked josephson junctions, 2025.

[123] F. Hassani, M. Peruzzo, L. N. Kapoor, et al. Inductively shunted transmons exhibit noise insensitive plasmon states and a fluxon decay exceeding 3 hours. *Nature Communications*, 14:3968, 2023.

[124] Sameia Zaman. Kinetic inductance characterization of thin 2h-nbse2 superconductor using circuit quantum electrodynamics. *Master thesis*, 2024.

[125] Trevyn F. Q. Larson, Sarah Garcia Jones, Tamás Kalmár, Pablo Aramburu Sanchez, Sai Pavan Chitta, Varun Verma, Kristen Genter, Katarina Cicak, Sae Woo Nam, Gergő Fülöp, Jens Koch, Ray W. Simmonds, and András Gyenis. Localized quasiparticles in a fluxonium with quasi-two-dimensional amorphous kinetic inductors, 2025.

[126] Lukas Grünhaupt, Nataliya Maleeva, Sebastian T. Skacel, Martino Calvo, Florence Levy-Bertrand, Alexey V. Ustinov, Hannes Rotzinger, Alessandro Monfardini, Gianluigi Catelani, and Ioan M. Pop. Loss mechanisms and quasiparticle dynamics in superconducting microwave resonators made of thin-film granular aluminum. *Phys. Rev. Lett.*, 121:117001, Sep 2018.

[127] M Müller, T Luschmann, A Faltermeier, S Weichselbaumer, L Koch, G B P Huber, H W Schumacher, N Ubbelohde, D Reifert, T Scheller, F Deppe, A Marx, S Filipp, M Althammer, R Gross, and H Huebl. Magnetic field robust high quality factor nbtin superconducting microwave resonators. *Materials for Quantum Technology*, 2(1):015002, feb 2022.

[128] C. Macklin, K. O'Brien, D. Hover, M. E. Schwartz, V. Bolkhovsky, X. Zhang, W. D. Oliver, and I. Siddiqi. A near–quantum-limited josephson traveling-wave parametric amplifier. *Science*, 350(6258):307–310, 2015.

[129] Joseph Emerson, Marcus Silva, Osama Moussa, Colm Ryan, Martin Laforest, Jonathan Baugh, David G. Cory, and Raymond Laflamme. Symmetrized characterization of noisy quantum processes. *Science*, 317(5846):1893–1896, 2007.

[130] E. Knill, D. Leibfried, R. Reichle, J. Britton, R. B. Blakestad, J. D. Jost, C. Langer, R. Ozeri, S. Seidelin, and D. J. Wineland. Randomized benchmarking of quantum gates. *Phys. Rev. A*, 77:012307, Jan 2008.

[131] Easwar Magesan, J. M. Gambetta, and Joseph Emerson. Scalable and robust randomized benchmarking of quantum processes. *Phys. Rev. Lett.*, 106:180504, May 2011.

[132] Daniel Gottesman. Theory of fault-tolerant quantum computation. *Phys. Rev. A*, 57:127–137, Jan 1998.

[133] Easwar Magesan, Jay M. Gambetta, B. R. Johnson, Colm A. Ryan, Jerry M. Chow, Seth T. Merkel, Marcus P. da Silva, George A. Keefe, Mary B. Rothwell, Thomas A. Ohki, Mark B. Ketchen, and M. Steffen. Efficient measurement of quantum gate error by interleaved randomized benchmarking. *Phys. Rev. Lett.*, 109:080505, Aug 2012.